FABRICATION, CHARACTERIZATION AND SENSOR APPLICATIONS OF OPTICAL WHISPERING GALLERY MODE COUPLING SYSTEM

by

QIULIN MA

A Dissertation submitted to the

Graduate School-New Brunswick

Rutgers, The State University of New Jersey

in partial fulfillment of the requirements

for the degree of

Doctor of Philosophy

Graduate Program in Mechanical and Aerospace Engineering

Written under the direction of

Prof. Tobias Rossmann and Prof. Zhixiong Guo

and approved by

_____

_____

_____

_____

New Brunswick, New Jersey

[October, 2010]

ABSTRACT OF THE DISSERTATION

Fabrication, Characterization and Sensor Applications of Optical Whispering Gallery Mode Coupling System

By QIULIN MA

Dissertation Director:
Tobias Rossmann and Zhixiong Guo

Micro/nano optical whispering gallery mode (WGM) resonators have attracted tremendous attention in the past two decades due to their distinct feature of high quality factor in small mode volumes. However, few studies have been done on temperature sensitivity and measurement of WGM, instability characterization of WGM resonance and gas phase molecules detection using WGM, all of which are explored in the present study. A complete analytical description of optical WGM resonance in micro spherical resonators as well as an analysis of optical coupling between fiber taper and micro spherical resonator is reviewed and discussed. Experimental systems and methods are developed for fabrications of high quality silica microsphere (50μm ~500μm in diameter, quality factor ~10^7-10^8) and submicron fiber taper, which are examined utilizing both optical microscope and scanning electron microscope. Various WGM spectra are recorded for size matching between microsphere and fiber taper. Free spectrum range of the resonance is experimentally verified. Switching between TE mode and TM mode coupling is demonstrated. Three different coupling regimes by are achieved experimentally.

Temperature measurement based on WGM resonance wavelength shift is studied in a range of cryogenic temperatures (~110K) to near room temperatures (310K). The experimental results match with theory well. The ultra high temperature measurement resolution (potentially ~10^{-6}K) is discovered and discussed. Other unprecedented advantages of the sensor are also addressed. A vacuum chamber is fabricated to enclose the WGM system. WGM instability is characterized in vacuum, using reconstructed WGM spectra. A resonance wavelength shift noise level within 0.4pm is measured and analyzed. Gas phase molecule detection utilizing spectral shift of WGM is explored. A Mie theory analysis is carried out to interpret the experiment. Water vapor sensing is realized by SiO_2 nanoparticle coating on the microsphere. High measurement resolution (1ppm H_2O) in low humidity level (0%~10%) is found possible. Finally, gas phase molecule detection utilizing cavity enhanced absorption spectroscopy of WGM is also addressed by illustrating CRD, *Q*-spoiling and dip depth variation. An experiment system is designed and initial test result provides insights of future endeavors.

Acknowledgements

First, I would like to thank my academic advisor and thesis co-advisor, Prof. Tobias Rossmann, for his support, guidance and encouragement he has provided throughout my research in past five years. He trained me patiently and rigorously for valuable experimental skills through the project of dynamic data driven applicatoin system (DDDAS) in the first year, which really elevated my experimental research ability. In the WGM projects, he continued to play a key role in advising me for experimental details. He also created a space in which ideas could be freely explored. I have been always very impressed by his sharp intuition in experiments and his wide range and in-depth engineering knowledge.

Secondly, but not less importantly, I want to express my gratefulness to my thesis co-advisor Prof. Zhixiong Guo, who has offered me abundant guidance and support in the WGM projects. Besides the fact that he provided me unlimited freedom in using the instruments in his lab, he also treated me and advised me with nothing less than he did to the students in his own group. He has always tried to encourage me while I was going through difficulties in research and always tried to teach me how to identify new valuable research directions. His advices have always been insightful and penetrated to the details. Especially, his original and inspiring ideas on temperature sensing and hysteresis effect interpretation in humidity sensing have made our studies possible for high quality journal publications.

I have to say that I feel so lucky to have these two young and active research advisors during my PhD study. They have been a perfect combination for advising me in exploring exciting scientific subjects and for teaching me various aspects in life. I would miss very

much the fruitful years that we worked closely together. And I wish the best to their future collaborations.

I would also like to acknowledge my dissertation committee members Professors Tobias Rossmann, Zhixiong Guo, Jerry Shan and Wei Jiang for their patience in reading the dissertation draft and making valuable suggestions and advices.

Many thanks go out to our department technician John Petrowski, who has patiently offered me valuable helps in experimental designs and fabrications.

I would like to acknowledge the contributions from my labmate, Lei Huang, for the idea of humidity coating and for the cooperation on experimental coating work. I would also like to share the research credits with Lei on the recognized cooperation as stated in Chapter 7. And many thanks go to Ji Li in Prof. Huang's group for helping us on atomic force microscopy imaging.

Many thanks also go out to Prof. Denhardt in Department of Biology, Prof. Huang in Department of Food Science and Prof. James Harrington in Department of Materials Science at Rutgers University for their lab supports on the work of humidity coating, atomic force microscopy and CO_2 laser, respectively.

I would also like to take this chance to thank my friends: Lei Huang, Jian Jiao and Huan Huang, who were always willing to offer a hand if I need in running an experiment.

The research grants that have supported my research at Rutgers University are: Mechanical and Aerospace Engineering Fellowship, CBET-0651737, CTS-0522556 and CNS-0539152 from National Science Foundation, CSREES Award 2008-01336 from US Department of Agriculture and Rutgers Academic Excellence Fund.

Finally, I want to thank my parents and wife who have given me tremendous support and encouragement during my entire PhD study.

Dedication

To my parents and wife

Table of Contents

Lists of tables

List of Figures

CHAPTER 1

INTRODUCTION

1.1 Background and Motivation

Optical resonators consisting of two or more mirrors are utilized in all branches of modern linear and nonlinear optics. High performance of the devices, i.e. a high quality (Q) factor and high mode stability is important and desired, which makes the practical usage of such mirrors-based resonators technically restricted. A typical resonator of such kind is the traditional Fabry-Perot (FP) cavity, which is the earliest type used for the resonant cavity of laser. To increase the quality factor, the mirror reflectivity is usually increased through improving the coating. Decreasing the mirror size can achieve smaller mode volume. However, rather difficult and expensive tasks include high quality mirror fabrication, mirrors alignments and binding. The up-to-date microelectronic and semiconductor technology has made micro/nano scale optical resonators based on photonic crystal possible. Photonic crystals are composed of periodic dielectric nanostructures that affect the propagation of electromagnetic (EM) waves in the same way as the periodic potential in a semiconductor crystal affects the electron motion. A photonic crystal cavity can be formed by introducing crystal defects in the periodic nanostructures, which is finding applications in many areas of physics and engineering. However, the fabrication of these structures is very challenging and expensive. The quality factor is relatively small and currently well below 10^6 [1].

Dielectric resonators based on total internal reflection become a good alternative choice for confining light for they demonstrate ultra-high quality factors. The optical

resonance in such resonators is called whispering gallery mode (WGM). Savchenkov *et al.* [2] in Jet Propulsion Lab (JPL) at NASA have demonstrated a millimeter sized CaF_2 WGM resonator with quality factor (Q) higher than 10^{11}. However, the related fabrication is relatively simple and inexpensive. The WGM originally were introduced for sound wave propagating close to the cylindrical wall in St. Paul's Cathedral, London [3], where the acoustical modes were partially confined due to the suppression of the wave diffraction by the sound reflection from the curved dome walls. Since WGM is a morphology-dependent phenomenon, the radius of the resonator determines the effective volumes and distribution of the modes. Early WGM studies started with the work of Lord Rayleigh who studied the acoustical WGM of sound wave over a curved gallery surface almost a century ago [3-5]. In 1909, equations for resonant eigen-frequencies of dielectric and metallic spheres are derived by Debye [6], which also can be deduced from the theoretical studies by Mie on the scattering of plane electromagnetic waves by spheres in 1908 [7]. Widely discussed afterwards are generalized properties of electromagnetic resonances in dielectric spheres with emphasis on microwave modes in the early years [8, 9]. During the past two decades, optical whispering gallery mode have been realized in modern high quality dielectric resonators of many different shapes such as cylindrical [10], spherical [11], toroidal [12], ring [13] etc. They have drawn increasing attention due to their great potential in application of cavity quantum electrodynamics [14], microlasers [15, 16], optical filters [17], miniature sensors [18, 19], etc.

The first observations of WGM in optics can be attributed to solid-state WGM lasers. Laser action was studied by Garrett *et al.* [20] in Sm:CaF_2 crystalline resonators. The size of the resonators was in the millimeter range. Pulsed laser operation due to total internal

reflection in a ruby ring at room temperature has been observed [21]. Lasers then become one of the most obvious applications of optical WGM. Significant reduction of the lasing threshold can be realized due to the high quality factor of the resonators. Knight *et al.* [22] demonstrated laser emission from WGM in a highly refractive dye-doped solvent flowing in a normally illuminated silica capillary. Another way to create a WGM laser is by the use of solids doped with rare earth ions. Sandoghdar *et al.* [23] realized a WGM laser based on neodymium-doped silica microspheres with a 200-nW threshold. Cai *et al.* [16] utilized a microsphere made of highly doped erbium:ytterbium phosphate glass for generating laser at 1.5μm with an output power as high as 3μW and achieved a laser threshold pump power of 60μW.

The unique properties of WGM including narrow linewidth, tunability and high stability to environment conditions make it well suited for optical filtering. The narrow linewidth allows increased channel capacity in a communications band, while tunability provides spectral diversity and increased efficiency. Ilchenko *et al.* [24] demonstrated a high-Q microwave filter with linewidth of about 10MHz and a tuning range exceeding 10GHz utilizing a WGM resonator fabricated with lithium niobate. Savchenkov *et al.* [25] have produced optical filters with bandwidth of about 10 kHz using CaF_2 WGM resonators which can be tuned by temperature change. The insertion loss of the filter was at 5-dB level. Multi-resonator filters are also available with WGMs which have significantly more sparse spectra comparing with filters comprised of a single WGM. Multi-pole, high-Q filters based on cascaded WGMs fabricated with silica have been demonstrated, delivering a robust performance at 10 to 100 GHz bandwidths [26, 27].

In recent years, WGM resonators have attracted more attention on detecting biomolecules due to their very small volume and high quality factor. An evanescent wave is produced by the total internal reflection of light within the resonator which interacts with analytes on its surface. The evanescent wave protrudes above the resonator's surface by ~100nm and samples only the analytes on the surface. Surface treatments such as antibodies can provide specificity for the analyte so that the sensor only detects the molecules that bound to the surfaces. Blair and Chen [28] showed that the resonant coupling of power into the WGM allows for efficient use of long photon lifetimes of the high-Q WGMs to increase the interaction of the light and the particles under study. A great portion of the input power is absorbed by the fluorophore and thereby enhancing the fluorescence emission. It showed the improvement in sensitivity by over an order of magnitude and sample volume reduction by many orders of magnitude comparing with traditional fluorescence biosensing. On the other hand, for detection of unlabeled biomolecules, Arnold *et al.* [29] have extensively studied a silica microsphere coupled with a fiber taper as a sensor head. A shift of the WGM resonance frequency can be detected when a layer of molecules are attached on the surface of the microsphere and results in changes of effective resonator diameter and refractive index. Based on a perturbation analysis, they predicted that the shift should be inversely proportional to the microsphere radius and proportional to protein surface density and excess polarizability [30]. In 2005 Guo was the first to propose the idea of detection of a single molecule using WGM technique in his proposal to National Science Foundation and some simulation results were published in his PhD student Haiyong Quan's PhD dissertation in 2006 [91]; and later formally published in a journal article in 2007 [19].

High-*Q* WGM is also very valuable in increasing sensitivity of mechanical measurements. An acceleration sensor was developed by Laine *et al.* [31] based on microsphere WGM resonator and pedestal antiresonant reflecting waveguide coupler. Induced flexure-arm displacements were monitored through changes in the resonance characteristics of a spherical optical cavity coupled to the flexure. Better than 1 mg at 250Hz bandwidth and a noise floor of 100μg were achieved. Loppolo *et al.* [32] investigated a micro-optical force sensor based on the WGM. A compressive force applied to a hollow Polymethyl-methacrylate (PMMA) microsphere induces a change in both the shape and the index of refraction of the sphere leading to a shift in WGM. A measurement sensitivity as high as 7.664nm/N was demonstrated. Huston and Eversole [33] have also demonstrated a miniature optical strain-sensor technique capable of microstrain sensitivity. A fiber rod with 125μm in diameter is tensioned with piezoelectric transducer and WGM wavelength shift is induced during tensioning which yields a sensitivity of 0.14nm/μstrain. A miniature integrated gyroscope system based on optical WGM was proposed by JPL for potential applications in spacecrafts and satellites [34]. Sensitivity of this sensor is expected to be large due to large dispersion of the system. And it was predicted that the sensor may possess high enough sensitivity even on a millimeter-size scale.

Although WGM in dielectric micro resonators have been massively studied, few work can be found in the aspects of temperature sensitivity and temperature sensor applications of WGM, WGM coupling system stability measurement and gas phase chemical sensing, all of which are addressed in this dissertation. Fabrication instrumentations and methods are independently developed in this work for making high quality silica microsphere-fiber taper based WGM coupling system. Both microsphere and fiber taper are examined for

quality and structure using scanning electron microscopy (SEM). The WGM phenomenon is realized and the coupling is characterized for different sizes of microspheres and fiber tapers. Devices, alignments and measurement methods are developed to test temperature sensitivity of WGM in silica microspheres from cryogenic temperatures (~110K) to near room temperatures (~310K). Experimental results match the theoretical prediction well. Ultra-high resolution (potentially 10^{-6}K using current available technologies), fast response, and great integration potentials of temperature measurement using WGM are found and discussed. A specialized vacuum chamber is built for enclosing WGM coupling system which is versatile in both vacuum tests and gas sensing tests. The resonance shift noise level as well as variations of other resonance characteristics due to the instability of the fiber taper-microsphere coupling system are measured and characterized in vacuum, with the help of a fiber-ring resonator. As a result, a general approach for measuring the instability of any type of WGM coupling system is established. A potential WGM gas sensing method that uses a coated silica microsphere is explored. The coating is designed to specifically adsorb only the probed gas molecules (water molecules) and be transparent to the laser wavelength used. A theoretical analysis based on Mie theory is found to match the experiment result well, which also provide predictions for refractive index sensitivity of various design of such kind of WGM sensors. One ppm level change of water molecules is predicted to be resolvable. On the other hand, cavity-enhanced gas absorption spectroscopy based on WGM are theoretically examined and reviewed for three types of techniques i.e. cavity ring down, Q-spoiling, dip-depth variation based on an envisioned gas, methane (CH_4). An experimental setup is designed and built for characterizing the

WGM system in absorption based gas detection. The initial experimental attempt provides insights for clear directions of future endeavors for absorption based WGM gas sensing.

1.2 Dissertation outline

In each of the subsequent chapters, more relevant background information of the related studies is introduced at the beginning. In chapter 2, detailed theoretical description of WGM resonance in a spherical micro resonator is introduced. Chapter 3 presented the theory of optical coupling between fiber taper and microsphere as well as a theoretical estimate of size matching of the coupling system. Fabrications of microsphere and fiber taper as well as characterization of the fabricated coupling system are presented in Chapter 4. Chapter 5 introduces the temperature measurement of WGM in silica microspheres. Chapter 6 provides the specific design and fabrication procedure of the specialized vacuum chamber for the fiber taper-microsphere based coupling system. Resonance shift noise level are measured and characterized. In chapter 7, spectral shift response of WGM in a coated microsphere due to water vapor adsorption and desorption is studied both theoretically and experimentally. Chapter 8 present the study of gas molecular absorption spectroscopy based on WGM. Finally, a summary of the results and discussion of the future research are presented in Chapter 9.

CHAPTER 2

OPTICAL WHISPERING GALLERY MODE RESONANCE

2.1 Introduction

Whispering gallery phenomena (WGM) were first introduced by Lord Rayleigh in 1910 [5] by describing the phenomenon of acoustical waves he had observed propagating around the interior gallery of the Saint Paul's Cathedral. One can whisper along the wall and hear all long the inside perimeter of the dome. This kind of resonance phenomenon is also true with light waves. However, the related optical gallery, i.e., the optical cavity shrinks down to micro/nano scales. An optical cavity with circular geometry is called whispering gallery mode resonator. The optical modes of a spherical dielectric micro particle were first investigated by Mie at the beginning of 20th century [7]. The sharp features of the scattering spectrum were attributed to resonant circulation of optical energy within sphere. Light injected tangentially into the WGM type cavities is trapped in circular orbits within the surface by repeated total internal reflections. The low dissipation mechanism of confinement results in an unusual high quality factor. A wide range of resonators built for different applications have been fabricated and investigated in the last two decades. Among them the surface-tension-induced microcavities, such as silica microspheres, attract great interests due to the unprecedented quality factors (Q) and low fabrication cost. In this chapter, the WGM resonant characteristics of the dielectric spherical resonator, such as field distribution, cavity quality factor, loss mechanisms and measurement methods of quality factor are discussed.

2.2 Geometric Optics Analysis of WGM

In a spherical micro resonator which has radius R_0, the light beams are confined inside by total internal reflection (TIR), i.e., the angels between beams and normal directions of the boundary satisfy Snell's law. The propagation path of the light inside the resonator can be approximated as a polygon as shown in Figure 2.1. The smaller the resonance

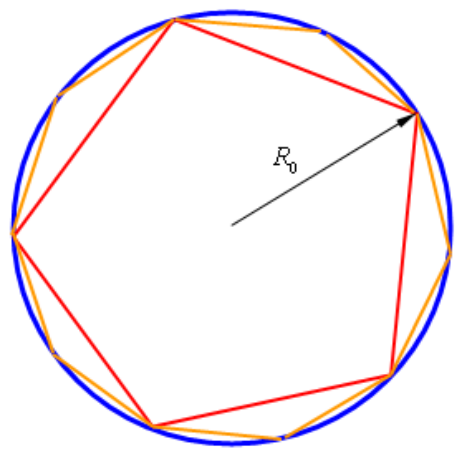

Figure 2.1 Geometric Schematic of the WGM resonance.

wavelength, the higher order the polygon. In order to simplify this geometric optics analysis, we assume that $R_0 >> \lambda_0$ so that the distance of travelling path of photons inside the optical micro resonator is equal to its equatorial circumference. By applying the phase-matching principle of the resonance, we have

$$\frac{\lambda_0}{n_s} \cdot m = 2\pi R_0 \tag{2.1}$$

where n_s is the refractive index of the micro resonator, λ_0 is the resonance wavelength and m is the azimuthal mode number. So for the mth and (m+1)th mode, we have

$$\frac{1}{\lambda_0} = \frac{m}{2\pi R_0 n_s} \tag{2.2}$$

and
$$\frac{1}{\lambda_1} = \frac{m+1}{2\pi R_0 n_s} \tag{2.3}$$

Subtracting (2.2) from (2.3), we have

$$\frac{\lambda_0 - \lambda_1}{\lambda_0 \lambda_1} = \frac{1}{2\pi R_0 n_s}$$

Thus, the free spectral range (FSR) which we define as the spacing between any two successive modes is

$$FSR = \lambda_0 - \lambda_1 = \frac{\lambda_0 \lambda_1}{2\pi R_0 n_s} \approx \frac{\lambda_0^{\ 2}}{2\pi R_0 n_s} \tag{2.4}$$

where we have used the fact that $\lambda_0 \approx \lambda_1$. This result is fairly accurate as long as the circumference of the resonator is much greater than the resonance wavelength. We will use it to compare with the FSR derived from electromagnetic theory.

2.3 Electromagnetic theory analysis of WGM in spherical micro resonators

The electromagnetic (EM) wave modes exists inside a spherical micro resonator are excited by the evanescent field from the fiber optic waveguide. To investigate the general time varying fields in the resonator, Maxwell's equation is applied and written as

$$\nabla \times \vec{E} = -\frac{\partial \vec{B}}{\partial t} \tag{2.5}$$

$$\nabla \times \vec{H} = \vec{J} + \frac{\partial \vec{D}}{\partial t} \tag{2.6}$$

$$\nabla \cdot \vec{B} = 0 \tag{2.7}$$

$$\nabla \cdot \vec{D} = \rho \tag{2.8}$$

where $\vec{E}$ and $\vec{H}$ are electric and magnetic field intensity, respectively, $\vec{D}$ is the electric displacement, $\vec{B}$ is the magnetic flux density, $\vec{J}$ is the current density and ρ is the electric charge density.

If we assume the medium is dielectric ($\rho = 0$ and $J = 0$) and isotropic with constant scalar permittivity and permeability, we have

$$\vec{D} = \varepsilon \vec{E} \text{ and } \vec{B} = \mu \vec{H} \tag{2.9}$$

where $\varepsilon = \varepsilon_r \varepsilon_0$ and $\mu = \mu_r \mu_0$, ε_0 and μ_0 are the permittivity and permeability of vacuum, ε_r and μ_r are the relative permittivity and relative permeability, respectively, for the dielectric materials.

Taking the curl operation of (2.5), we have

$$\nabla \times (\nabla \times \vec{E}) + \frac{\partial}{\partial t}(\nabla \times \vec{B}) = 0 \tag{2.10}$$

Using the vector identity $\nabla \times \nabla \times A = \nabla(\nabla \cdot A) - \nabla^2 A$, we obtain

$$\nabla(\nabla \cdot \vec{E}) - \nabla^2 \vec{E} = -\mu \nabla \times \left(\frac{\partial \vec{H}}{\partial t} \right) \tag{2.11}$$

By substituting (2.6) and (2.8) in (2.11), we find

$$\nabla^2 \vec{E} - \mu\varepsilon \frac{\partial^2 \vec{E}}{\partial t^2} = 0 \tag{2.12}$$

If we choose a harmonic solution of the electric field as $E\left(\vec{r}, t\right) = E\left(\vec{r}\right) e^{i\omega t}$, we obtain

$$\nabla^2 \vec{E} + \omega^2 \mu\varepsilon \vec{E} = 0 \tag{2.13}$$

where we define the propagation constant $k = \omega\sqrt{\mu\varepsilon} = \frac{\omega}{c} = \frac{2\pi}{\lambda}$ and c is the speed of light in the resonator, so we obtain the Helmholtz's equation

$$\nabla^2 \overline{E} + k^2 \overline{E} = 0 \tag{2.14}$$

The spherical coordinates is adopted as shown in Figure 2.2 for describing the whispering gallery mode resonance in a sphere. And in spherical coordinates, we have

$$\nabla^2 f = \frac{1}{r^2}\frac{\partial}{\partial r}(r^2 \frac{\partial f}{\partial r}) + \frac{1}{r^2 \sin\theta}\frac{\partial}{\partial \theta}(\sin\theta \frac{\partial f}{\partial \theta}) + \frac{1}{r^2 \sin^2\theta}\frac{\partial^2 f}{\partial \varphi^2} \tag{2.15}$$

So, in the spherical coordinates, equation (2.14) becomes

$$\frac{1}{r^2}\frac{\partial}{\partial r}(r^2 \frac{\partial E}{\partial r}) + \frac{1}{r^2 \sin\theta}\frac{\partial}{\partial \theta}(\sin\theta \frac{\partial E}{\partial \theta}) + \frac{1}{r^2 \sin^2\theta}\frac{\partial^2 E}{\partial \varphi^2} + k^2 E = 0 \tag{2.16}$$

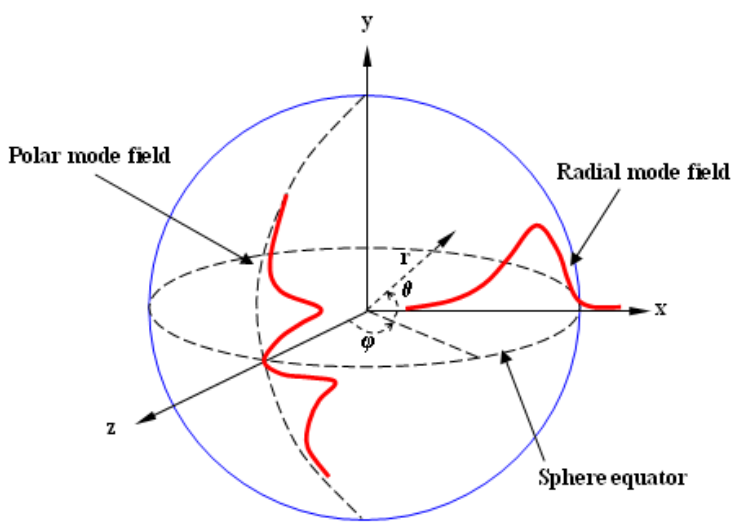

Figure 2.2 Schematic of WGM resonance in a spherical coordinates.

To solve equation (2.16), the transverse electric (TE) mode is considered so that the electric field has only the θ-component. The polarization direction of the EM field of a spherical resonator can be approximated constant along the same spherical coordinate axes at all points in space. Therefore either E or H of the EM field is separable [41], i.e.

$$E = E_\theta = \Psi_r(r) \cdot \Psi_\theta(r) \cdot \Psi_\varphi(\varphi) \tag{2.17}$$

By plugging equation (2.17) into equation (2.16), we have:

$$\frac{1}{\Psi_r}\frac{d}{dr}(r^2\frac{d\Psi_r}{\partial r})+\frac{1}{\Psi_\theta \sin\theta}\frac{d}{d\theta}(\sin\theta\frac{d\Psi_\theta}{d\theta})+\frac{1}{\Psi_\varphi \sin^2\theta}\frac{d^2\Psi_\varphi}{d\varphi^2}+k^2r^2=0 \qquad (2.18)$$

Thus (2.18) can be separated into three ordinary differential equations for components r, θ and φ, respectively. Next, we solve the field distribution for each component of the electric field.

(I).The radial field satisfied the equation

$$\frac{d^2\Psi_r}{dr^2}+\frac{2}{r}\frac{d\Psi_r}{dr}+(k^2-\frac{l(l+1)}{r^2})\Psi_r=0 \qquad (2.19)$$

which is the spherical Bessel differential equation. The general solutions of (2.11) is

$$\Psi_r=c_1 j_l(kr)+c_2 y_l(kr) \qquad (2.20)$$

where j_l and y_l are the first and second kind of spherical Bessel functions, respectively, of order l and are related to the ordinary Bessel functions J_l and Y_l by:

$$j_l(x)=\sqrt{\frac{\pi}{2x}}J_{l+1/2}(x) \qquad (2.21)$$

$$y_l(x)=\sqrt{\frac{\pi}{2x}}Y_{l+1/2}(x)=(-1)^{l+1}\sqrt{\frac{\pi}{2x}}J_{-l-1/2}(x) \qquad (2.22)$$

To validate solution in (2.20), we examine it when radius approaches 0. We know from the property of spherical Bessel functions that as $x<<1$, $j_l(x)\to\frac{x^l}{(2l+1)!!}$ and $y_l(x)\to-\frac{(2l-1)!!}{x^{l+1}}$, which means $y_l(r)$ is divergent as $r\to 0$. Since the field must be finite everywhere, the radial field distribution inside the sphere is reduced to

$$\Psi_r = cj_l(kr) \text{ for } r < R_0 \tag{2.23}$$

As the propagation of the light is confined in the sphere by TIR, to obey the continuity of Maxwell equations at the boundary, there is an evanescent field that decays exponentially outside the sphere for the radial field distribution. To obtain the field outside the sphere, we assume $\Psi_r = \frac{\phi_r}{r}$ and equation (2.19) becomes

$$\frac{d^2\phi_r}{dr^2} + (k^2 - \frac{l(l+1)}{r^2})\phi_r = 0 \tag{2.24}$$

where we set $r = R_0 + \Delta r$ and get:

$$\frac{d^2\phi_r}{d\Delta r^2} + (k^2 - \frac{l(l+1)}{(R_0 + \Delta r)^2})\phi_r = 0 \tag{2.25}$$

Since the evanescent field usually extends out the boundary by several wavelengths of the total internal reflected beam inside the sphere, we can assume that $\frac{\Delta r}{R_0} \to 0$. Therefore equation (2.25) is reduced to:

$$\frac{d^2\phi_r}{d\Delta r^2} + (k^2 - \frac{l(l+1)}{{R_0}^2})\phi_r = 0 \tag{2.26}$$

The solution of equation (2.26) is:

$$\phi_r = C\exp(-\alpha \cdot \Delta r) \text{ where } \alpha = \sqrt{\frac{l(l+1)}{R_0^2} - k^2} \tag{2.27}$$

Therefore

$$\Psi_r = \frac{\phi_r}{r} = \frac{C}{r}\exp(-\alpha \cdot \Delta r) \tag{2.28}$$

Since $r = R_0 + \Delta r \approx R_0$, we have

$$\Psi_r = \frac{C}{R_0}\exp(-\alpha \cdot \Delta r) = B\exp(-\alpha \cdot \Delta r) \tag{2.29}$$

So, the radial field distribution is summarized as

$$\Psi_r = \begin{cases} Aj_l(kr) & (r < R_0) \\ B\exp(-\alpha \cdot (r - R_0)) & (r > R_0) \end{cases} \tag{2.30}$$

where A and B are constants which are determined by matching the boundary conditions at the surface. The radial field distribution is related to the mode numbers *l* and *n*. And *n* denotes the number of maxima of the field in radial distribution.

Once the radius, refractive index, polar index *l* and the polarization state of the WGM resonance are specified, along with the refractive index of the environment, a series of resonant wavelengths can be obtained by solving the characteristic equations [35]:

$$(\eta_s \alpha_s + \frac{1}{R_0}) j_l(k_0 n_s R_0) = k_0 n_s j_{l+1}(k_0 n_s R_0) \tag{2.31}$$

where $\eta_s = \begin{cases} 1 & TE \\ \left(\dfrac{n_s}{n_0}\right)^2 & TM \end{cases}$

The longest one corresponds to *n*=1, the secondary to *n*=2, and so forth. The fundamental WGMs correspond to *n*=1 and *l*=*m*, which are usually favored in most of the applications. They are featured by possessing a single intensity maximum in both radial and polar directions and the field maximum is the most close to the equator. Therefore, they are the strongest modes to have energy exchange with the external coupler. Fundamental WGMs consist a quasi-periodic resonant spectrum for a given microsphere resonator. With decrease of the resonant wavelength, the polar indices *l* increases successively, corresponding to an increase number of field maximum in the azimuthal direction. The spacing between any two modes with successive *l* numbers is defined as the free spectral

range (FSR). As an example, Figure 2.3 shows the normalized radial field intensity for a sphere with radius of 40μm at different *l* and *n* numbers.

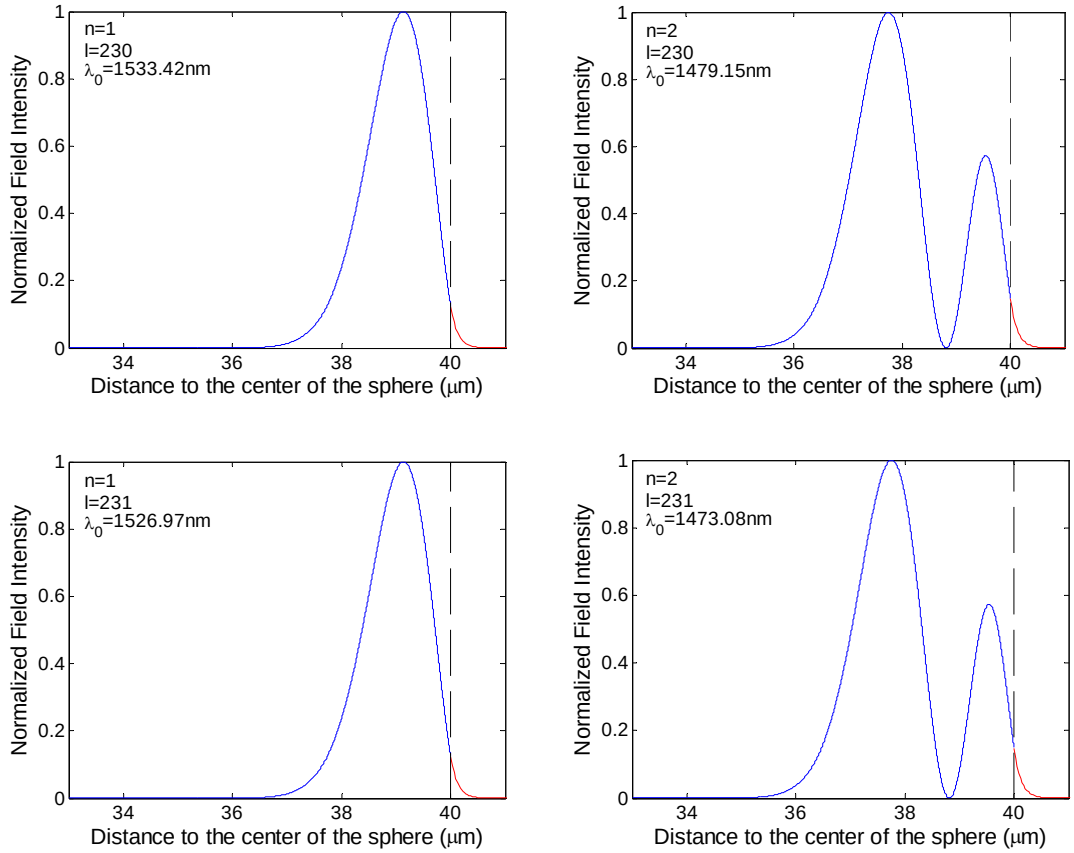

Figure 2.3 Normalized radial field intensity distributions in a sphere with radius of 40μm. The resonance parameters are (*n*=1, *l*=230, λ_0 =1533.42nm), (*n*=1, *l*=231, λ_0 =1526.97nm), (*n*=2, *l*=230, λ_0 =1479.15nm) and (*n*=2, *l*=231, λ_0 =1473.08nm).

It is seen that the resonance wavelength spacing between two adjacent *n* numbers is much larger than that of the two successive *l* numbers. By comparing the FSR derived from the geometric optics analysis and the on from EM theory analysis, we can validate the solutions from Maxwell equations. The resonance wavelength for equation (2.4) is taken as the average of the wavelengths of two adjacent *l* number modes. By plugging in n_s =1.4682

(refractive index of Corning SMF-28 fiber) and R_0 =40μm, we get the results of FSR in Table 2.1 for the cases in Figure 2.3. The error between the geometric optic analysis and EM theory analysis is negligible for *n*=1(<2%). And the FSR got from *n*=2 deviates more between the two analysis which illustrates that the geometric optics analysis is for the fundamental WGMs.

Table 2.1 Comparison between geometric optics analysis and EM theory analysis for FSR.

	Geometric (FSR)	EM theory (spacing)	Error
Between (n=1, l=230) and (n=1, l=231)	6.35nm	6.45nm	1.6%
Between (n=2, l=230) and (n=2, l=231)	5.91nm	6.07nm	2.6%

(II).The azimuthal field distribution obeys the equation

$$\frac{d^2\Psi_\varphi}{d\varphi^2} + m^2\Psi_\varphi = 0 \tag{2.32}$$

With a periodicity of 2π for azimuthal direction, so the solution is:

$$\Psi_\varphi = N_\varphi \exp(im\varphi) \text{ with } N_\varphi = 1/\sqrt{2\pi} \tag{2.33}$$

which is a simple sinusoidal distribution. The integer *m* is the azimuthal mode number and N_φ is the normalization constant obtained from solving $\int_0^{2\pi} \left|\Psi_\varphi\right| d\varphi = 1$.

(III). The polar field distribution follows

$$\frac{1}{\sin\theta}\frac{1}{d\theta}(\sin\theta\frac{d\Psi_\theta}{d\theta}) + \left[l(l+1-\frac{m^2}{\sin^2\theta}) \right]\Psi_\theta = 0 \tag{2.34}$$

which is a spherical harmonic differential equation and the solution is associated Legendre polynomials:

$$\Psi_\theta = N_\theta P_l^m(\cos\theta) \tag{2.35}$$

where m degenerates with l in wavelength, that is for a given polar index, l, there are $2m+1$ modes that possess the same resonant wavelength. m=-l, -(l-1), -(l-2)…,l-2, l-1, l and $l-|m|+1$ gives the number of intensity maximum in the polar direction. N_θ is a normalization constant obtained from $\int_0^{2\pi}|\Psi_\theta|d\theta=1$. Figure 2.4 shows a normalized field intensity distribution of a TE mode in the polar direction for a sphere with radius of 40μm.

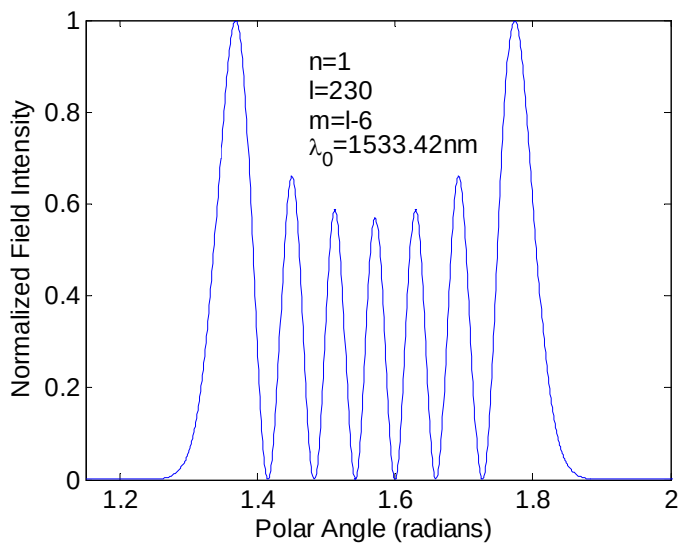

Figure 2.4 The normalized field intensity distribution of a TE mode in the polar direction for a sphere with radius of 40μm. The resonance wavelength is 1533.42nm and numbers are *n*=1, *l*=230, *m*=*l*-6.

2.4 Resonator quality factor

The extent of energy dissipation of a WGM mode in a resonator is commonly expressed by the quality factor (Q-factor) of resonator, which is defined as the energy stored in the mode times the angular frequency and divided by the energy dissipation rate:

$$Q \equiv \frac{\omega_0 U}{-\left(\frac{dU}{dt}\right)} \tag{2.36}$$

where ω_0 is the angular frequency of the resonant wave, U is the stored energy in the mode. The solution to equation (2.36) is:

$$U(t) = U(0)e^{-\omega_0 t/Q} \tag{2.37}$$

The time dependence of the stored energy suggests that the optical field damps as

$$E(t) = E(0)e^{-\omega_0 t/2Q}e^{-i\omega_0 t} \tag{2.38}$$

Standard Fourier analysis yields

$$E(t) = \frac{1}{\sqrt{2\pi}}\int_{-\infty}^{\infty} E(\omega)e^{-i\omega t}d\omega \tag{2.39}$$

where

$$E(\omega) = \frac{1}{\sqrt{2\pi}}\int_{-\infty}^{\infty} E(0)e^{-\omega_0 t/2Q}e^{i(\omega-\omega_0)t}dt \tag{2.40}$$

It follows that

$$\left|E(\omega)\right|^2 \propto \frac{1}{(\omega-\omega_0)^2 + (\omega_0/2Q)^2} \tag{2.41}$$

Therefore, in frequency domain the resonance has a Lorentzian shape with a Full Width at Half Maximum (*FWHM* or $\Delta\omega$) equal to ω_0/Q. Thus, the practical formula for calculating Q-factor from measurement is:

$$Q = \frac{\omega_0}{\Delta\omega} = \frac{f_0}{\Delta f} \tag{2.42}$$

where $f_0 = \omega_0/2\pi$ and Δf are the frequency and *FWHM* of the resonance, respectively. Figure 2.5 shows an example of the spectrum of a WGM resonance with $Q \approx 2\times10^7$ at a center wavelength around 1531nm.

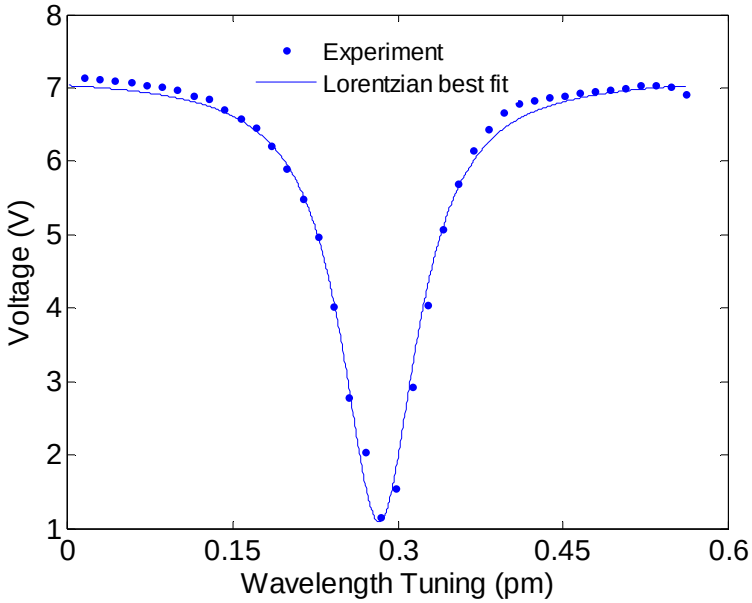

Figure 2.5 Spectrum of a WGM resonance with $Q \approx 2\times10^7$ at a center wavelength around 1531nm.

Part of the incident light power is coupled into the WGM mode through an optical coupler. The rest travels down the coupler in the form of guided modes to the output as if it does not see the resonator. There are several types of loss mechanisms which keep the light from being eternally trapped in the resonator. These include: (1) scattering loss due to surface roughness; (2) loss due to surface contamination; (3) absorption loss due to molecular resonance; (4) radiation loss due to boundary curvature of propagation; (5) coupling loss due to energy coupling back to the coupler's guided modes. To differentiate these losses by Q-factors, we rewrite equation (2.36) as

$$\frac{1}{Q}=\frac{-\left(\frac{dU}{dt}\right)}{\omega_0 U}=\frac{-\left(\frac{dU_{scat}}{dt}\right)}{\omega_0 U}+\frac{-\left(\frac{dU_{cont}}{dt}\right)}{\omega_0 U}+\frac{-\left(\frac{dU_{absorb}}{dt}\right)}{\omega_0 U}+\frac{-\left(\frac{dU_{rad}}{dt}\right)}{\omega_0 U}+\frac{-\left(\frac{dU_{coup}}{dt}\right)}{\omega_0 U} \quad (2.43)$$

Thus,

$$\frac{1}{Q}=\frac{1}{Q_{scat}}+\frac{1}{Q_{cont}}+\frac{1}{Q_{absorb}}+\frac{1}{Q_{rad}}+\frac{1}{Q_{coup}} \tag{2.44}$$

where Q_{scat}, Q_{cont}, Q_{absorb}, Q_{rad} and Q_{coup} result from scattering loss, contamination loss, absorption loss, radiation loss and coupling loss, respectively. And we define intrinsic Q-factor as:

$$\frac{1}{Q_{in}}=\frac{1}{Q_{scat}}+\frac{1}{Q_{cont}}+\frac{1}{Q_{absorb}}+\frac{1}{Q_{rad}} \tag{2.45}$$

So that the total loaded Q-factor can be simply decomposed as:

$$\frac{1}{Q}=\frac{1}{Q_{in}}+\frac{1}{Q_{coup}} \tag{2.46}$$

Calculations based on the model of Rayleigh scattering by molecular-sized surface clusters under grazing incidence and TIR yield the estimate for Q_{scat} as [36]:

$$Q_{scat}=\frac{\lambda^2 D}{2\pi^2\sigma^2 B} \tag{2.47}$$

where σ and B are the rms size and the correlation length of surface roughness, respectively. D is the diameter of the resonator and λ is the resonance wavelength. The Q-factor resulted from molecular absorption can be estimated as [36]:

$$Q_{absorb}=\frac{2\pi n_s}{\alpha\lambda} \tag{2.48}$$

where n_s is the refractive index of the resonator, α is absorption coefficient of the resonator's material. The volume current method can be used to approximate the radiation loss. Thus, the associated Q-factor Q_{rad} can be estimated as: [35]

$$Q_{rad}=\frac{l^2 n_s}{k^3 c_0 \varepsilon_0 N_s^2 n_0^2 R_0^5 Z_0}\left[n_0\left(\frac{\pi}{\gamma_1}\right)^{1/4} j_l(kn_sR_0)j_{l+1}(kn_0R_0)-n_s\left(\frac{\pi}{\gamma_2}\right)^{1/4} j_{l-1}(kn_sR_0)j_l(kn_0R_0)\right]^{-2} \tag{2.49}$$

where $\gamma_1 = l - \frac{1}{2} - kn_0R_0 \frac{j_l(kn_0R_0)}{j_{l-1}(kn_0R_0)} + \frac{(kn_0R_0)^2}{l}$, $\gamma_2 = l + \frac{1}{2} - kn_0R_0 \frac{j_{l+1}(kn_0R_0)}{j_l(kn_0R_0)} + \frac{(kn_0R_0)^2}{l}$,

c_0 is the vacuum speed of light, $Z_0 \approx 377$ is the impedance of free space, and the normalization constant

$$N_s = \left\{ \sqrt{\frac{\pi}{m}} 2^{N-1} N! R_0^2 \left[\left(1 + \frac{1}{\alpha R_0} \right) j_l^2(kn_sR_0) - j_{l-1}(kn_sR_0) j_{l+1}(kn_sR_0) \right] \right\}^{-1/2}$$

l and *m* are the polar and azimuthal mode numbers, respectively. Modes with the same *l* value but differing in *m* values, have similar loss, and therefore *m* does not appear explicitly in these equations.

(I).Linewidth measurement of *Q*-factor

Equation (2.42) can be used to compute the *Q*-factor of a WGM. The key is to measure the *FWHM* or linewidth, Δf (or $\Delta\lambda$) of a WGM. As shown by Figure 2.5, the resonance lineshape is actually obtained by scanning the frequency of a tunable laser through the resonance. Therefore, such a lineshape detected is actually the convolution of the laser lineshape with the WGM resonance lineshape. The laser's lineshape is also Lorentzian. Let us assume that the WGM lineshape follows:

$$O(x) = \frac{1}{\pi} \left[\frac{\gamma_2}{(x - x_2)^2 + \gamma_2^2} \right] \tag{2.50}$$

which has a $FWHM_{WGM}$ of $2\gamma_2$. And the laser has a lineshape of

$$h(x) = \frac{1}{\pi} \left[\frac{\gamma_1}{(x - x_1)^2 + \gamma_1^2} \right] \tag{2.51}$$

which has a $FWHM_{laser}$ of $2\gamma_1$. Thus, the lineshape we measured is

$$I(X) = O(x) * h(x) = \int_{-\infty}^{+\infty} O(x)h(X-x)dx \tag{2.52}$$

Using the property of Fourier transform of convolution

$$F\{O(x) * h(x)\} = F\{O(x)\}F\{h(x)\} \tag{2.53}$$

Therefore, the convolution is obtained as

$$I\{X\} = F^{-1}\{F\{O(x)\}F\{h(x)\}\} = \frac{1}{\pi}\left[\frac{\gamma_1 + \gamma_2}{(X - x_1 - x_2)^2 + (\gamma_1 + \gamma_2)^2}\right] \tag{2.54}$$

which has a $FWHM_{convolution}$ of $2(\gamma_1 + \gamma_2) = 2\gamma_1 + 2\gamma_2$. Therefore, we have the formula of the original *FWHM* of WGM is

$$FWHM_{WGM} = FWHM_{convolution} - FWHM_{laser} \tag{2.55}$$

So, when the laser's linewidth is more than one order of magnitude narrower than that of the WGM, the linewidth of the WGM obtained by scanning the laser can be approximated as the original linewidth. Otherwise, equation (2.55) should be applied to consider the convolution effect in the linewidth measurement of *Q*-factor.

(II).Cavity ring down measurement of *Q*-factor

When the *Q*-factor of a WGM is high enough so that the WGM linewidth is comparable to the linewidth of the laser, the linewidth measurement of *Q*-factor becomes inaccurate. As indicated by equation (2.37), the stored energy in a mode decays exponentially with time in the micro resonator. Therefore, the time constant of the decay, or the photon life time of the resonance is:

$$\tau = \frac{Q}{\omega_0} = \frac{Q}{2\pi f_0} \tag{2.56}$$

which is linearly related to Q-factor. Therefore if the incident light coupled into the micro resonator is suddenly turned off, the decaying signal can be detected and used to find Q-factor of the mode. Such a method is called cavity ring down (CRD) measurement. As a more advanced method, it can be applied for high-Q measurement with better accuracy. Photon lifetime in time domain can be directly recorded by CRD measurement. The laser linewidth is not a limitation of this method any more.

Catching the decaying signal in CRD measurement is actually quite challenging, which requires three key factors: fast blocking of the incident laser, trigger of the blocking at the fully charged point of WGM, fast photo detector. As shown in Figure 2.6, the laser is tuned and coupled into an optical fiber which goes to a high speed $LiNbO_3$ Mach-Zehnder (MZ) electro-optic modulator (10Gb/s X5 JDSU). The schematic of the modulator is shown in Figure 2.7. Light from the input waveguide is split at a Y-junction and half the

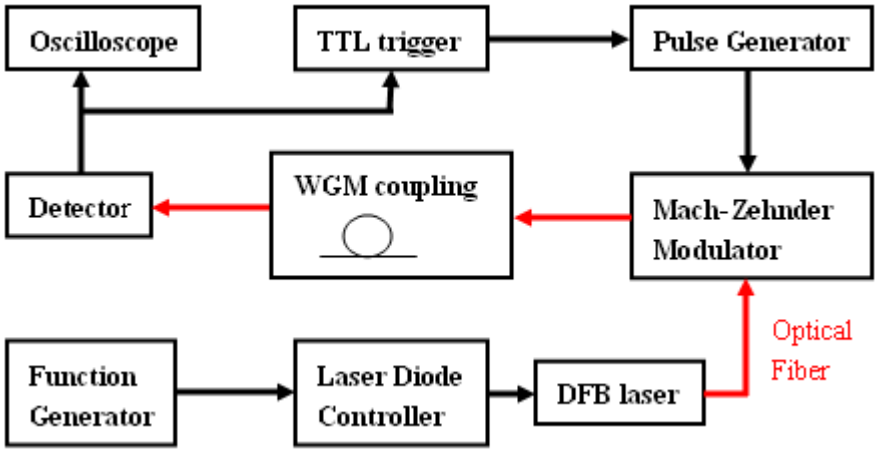

Figure 2.6 Design of the CRD measurement.

optical power passes through each of the two parallel waveguides. As a DC voltage and a high frequency voltage pulse apply on the Bias electrode and the RF electrode, respectively,

one path of the light can be phase shifted so that the output intensity becomes zero after the recombination of the two paths of light. The high frequency pulse is generated by a function generator (Agilent 33220A) which is triggered by a TTL trigger circuit as shown in Figure 2.8. The 5V trigger signal is generated when the peak of the WGM resonance is reached and identified by the reference voltage. Therefore, the oscilloscope (Tektronix TDS3034B 2.5GS/s) acquires the decaying signal after the incident laser is blocked.

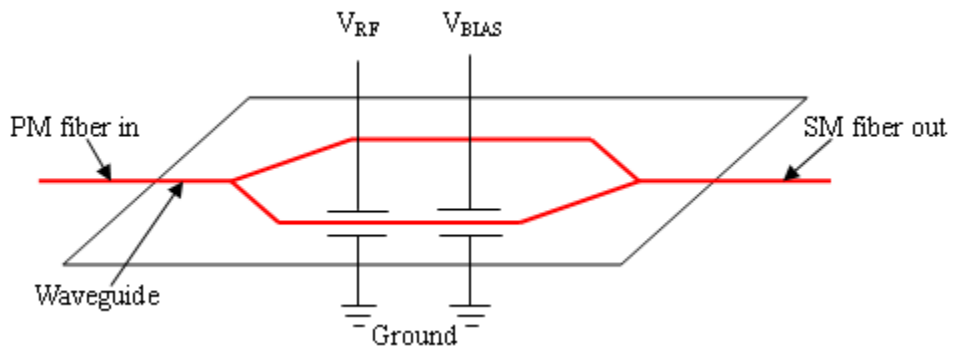

Figure 2.7 Schematic of Mach-Zehnder electro-optic modulator.

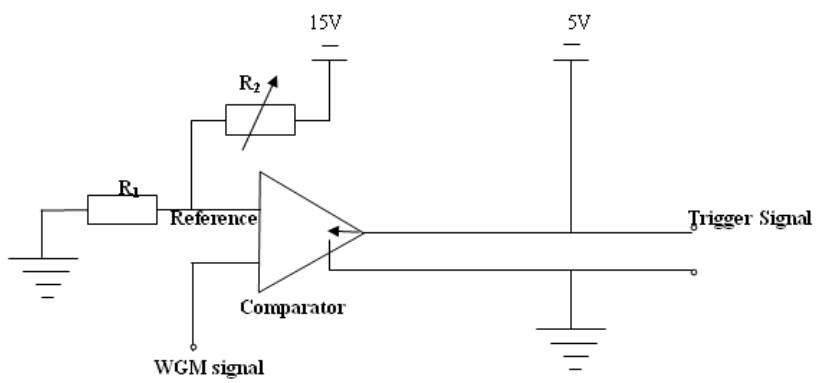

Figure 2.8 Design of the TTL trigger circuit.

Figure 2.9 shows an acquired spectrum from the system described in Figure 2.6. The laser is successfully blocked at the peak of the WGM. However, the CRD decaying signal was not captured due to that the blocking and photo detection is not fast enough for *Q*-factor we

measure. The WGM shown in Figure 2.9 has a Q of ~10^7 (estimated by linewidth method) which corresponds to photon life time at an order of ~10ns. The rise time of MZ modulator is only 40ps. The 100ns blocking time estimated from Figure 2.9(b) caused by the response delay combination of pulse generator and detector. Therefore, much faster versions of these two instruments need to be used to capture the CRD decaying signal.

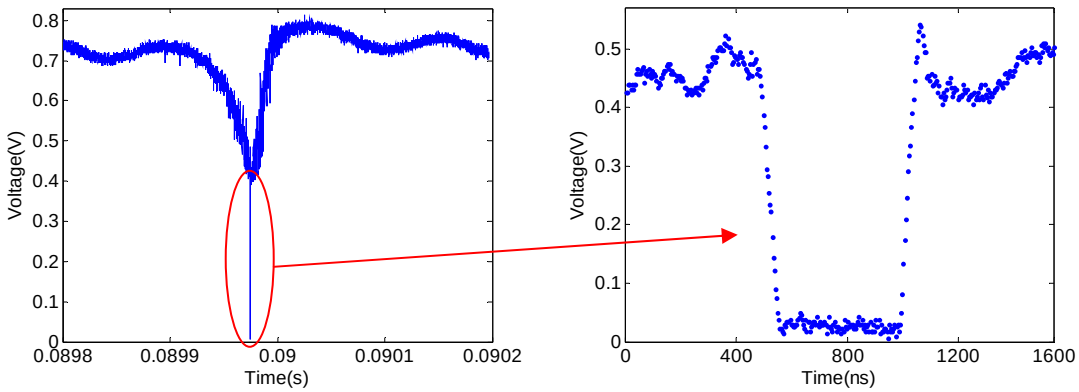

(a) (b)

Figure 2.9 (a) Laser blocking on at the fully charged point of WGM (b) Zoom-in of the blocking.

CHAPTER 3

OPTICAL COUPLING OF WHISPERING GALLERY MODE

3.1 Introduction

In this chapter, various strategies of coupling light into the spherical micro-resonator through evanescent wave are reviewed. Both advantage and disadvantage of them are introduced. Fiber taper coupling is selected as the coupler for this study. An approach to describe the near-field coupling of a WGM with a propagating mode in fiber taper is presented. The relation between the Q-factors from coupling loss and intrinsic loss is discussed to identify three different coupling regimes. Phase-matching between the guided modes in the fiber taper and WGM is presented as a principle of determining appropriate size-matching of the resonator and fiber taper.

3.2 Near-field coupling strategies for WGM

In order to utilize high Q-factor spherical optical resonators, a major challenge is to excite the whispering gallery modes efficiently without compromising Q-factor. The modes in the optical resonator are highly confined and thus are not accessible by a free-space beam. Employments of near-field couplers are required. An evanescent field generated at a surface which totally reflects light in the other side was shown to be the most promising approach to transfer power from the coupler into the whispering gallery modes. Therefore, the performance of the coupler with which light is passed into and out of the sphere is crucial. A good coupler should have the following merits: (1) Excite WGM

efficiently with little potential of Q-spoiling; (2) simple coupler-to-sphere alignment; (3) clearly defined ports; (4) inexpensive fabrication process.

Four popular WGM coupling strategies are shown in Figure 3.1. Prism coupling is most earliest used and required only relatively inexpensive hardware [37]. A free space laser beam is directed into a prism to achieve total internal reflection at the prism surface. The evanescent field on the other side of the prism surface allows the light to tunnel into the resonator through the glass-air interface. However, it requires bulky components and awkward alignments. Achieving optimal alignment is challenging. The fiber half-block consists of a fiber that is polished to expose the core for near-field coupling [38]. The major drawback is that the coupling coefficient is low due to the leakage of light from WGM back into the radiation modes in the cladding of the half-block and into the surrounding block. The fiber-prism coupling is robust and has the advantage of waveguide light delivery as well as prism coupling [39]. A fiber end is polished into an angled plane which serves as a

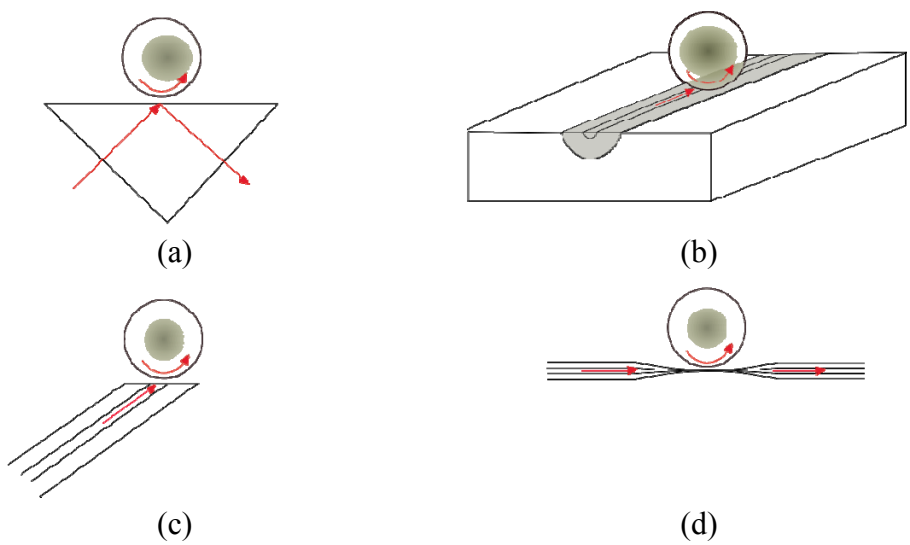

Figure 3.1 Different WGM coupling strategies: (a) prism coupling (b) fiber half-block coupling (c) fiber-prism coupling (d) fiber-taper coupling.

TIR surface for guided modes of the fiber. However, it requires delicate cutting and polishing the end of the fiber tip. Fiber taper can be fabricated so that the surrounding air is essentially the cladding and the evanescent tail of the fiber mode is well exposed for coupling [40]. It requires minimum effort to make alignment for coupling the light into and out of the resonator. It also allows sensitive tuning of the fiber-mode propagation constant by scanning the resonator along the taper waist at locations with different waist diameters. Fiber tapers can be conveniently fabricated by heating and pulling or chemical etching with low cost. The fiber taper coupler satisfies the four merits mentioned before and therefore is the one we selected for the study of this work.

3.3 Optical coupling between fiber taper and micro resonator

Let us examine the excitation of a single high *Q*-factor WGM by a single travelling mode in a fiber taper. As shown in Figure 3.2, let $E_0(t)$ be the electric field amplitude of the circulating mode of TIR in the resonator to model the whispering gallery mode. The pump amplitude is $E_{in}(t)$ and the transmitted amplitude is $E_{out}(t)$. Assuming that the coupling zone is much smaller than the diameter of the resonator, we can introduce local real amplitude coefficients r' to describe the coupling of the WGM to the guided mode in

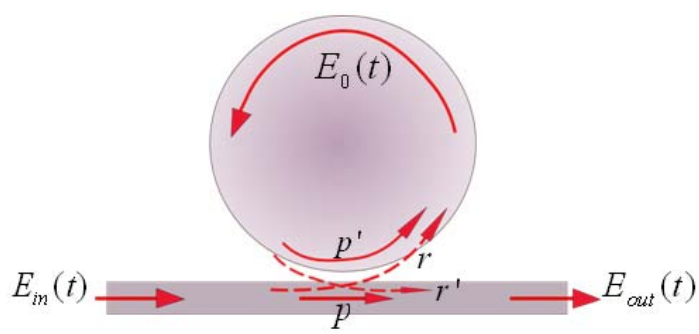

Figure 3.2 Schematic of the excitation of a WGM in micro resonator.

the fiber taper, and coefficient r to describe the guided mode in fiber taper coupling to the WGM. p and p' are the transmitted amplitude coefficients for the mode in fiber taper and WGM in the resonator, respectively, to describe the mode after passing through the coupling zone. Thus we can write the amplitude of the mode in the resonator and output of the fiber taper as [41]:

$$E_0(t) = p' E_0(t-\tau_0) e^{(i\varphi - \alpha L/2)} + irE_{in}(t) \tag{3.1}$$

$$E_{out(t)} = pE_{in}(t) + ir' E_0(t) \tag{3.2}$$

where $\tau_0 = n_s L / c_0$ is the circulation time for the mode travelling inside the resonator, $L \approx 2\pi R_0$ is approximately equal to circulation distance traveled by the mode inside the resonator, $\varphi = 2\pi n_s L / \lambda$ is the phase lag after the mode travel one circle in the resonator. n_s is the refractive index of the resonator, c_0 is the speed of light in vacuum, and α is the intrinsic loss coefficient in the resonator caused by scattering, contamination, absorption and radiation. Due to the time reversal symmetry and energy conservation, we have $p = p'$, $r = r'$ and $|p|^2 + |r|^2 = 1$. If the Q-factor of the resonator mode is high, intrinsic loss and coupling loss of WGM are both very small which means that $\alpha << 1$, $|r| << 1$. The angular resonant frequency can be approximated as $\omega_0 \approx 2\pi c_0 / \lambda_0$. Thus we have frequency detuning from resonance as:

$$\Delta\omega = \omega - \omega_0 = 2\pi c_0 \left(\frac{1}{\lambda} - \frac{1}{\lambda_0} \right) \approx 2\pi c_0 \frac{-\Delta\lambda}{\lambda_0^2} \quad . \tag{3.3}$$

And we also have

$$\varphi = 2\pi n_s L / \lambda = 2\pi n_s L \left(\frac{1}{\lambda} - \frac{1}{\lambda_0} + \frac{1}{\lambda_0} \right) = 2\pi n_s L \frac{-\Delta\lambda}{\lambda_0^2} + \frac{2\pi n_s L}{\lambda_0} = 2\pi n_s L \frac{-\Delta\lambda}{\lambda_0^2} + 2N\pi \quad . \tag{3.4}$$

where N is an integer. Combining (3.3) and (3.4), we have

$$\varphi = \frac{n_s}{c}\Delta\omega + 2N\pi \,. \tag{3.5}$$

So, $\exp(i\varphi - \alpha L/2) = \exp(i\frac{n_s L}{c}\Delta\omega - \alpha L/2)$, and using Taylor expansions, we have

$$\exp(i\varphi - \alpha L/2) = (1 + i\frac{n_s L}{c}\Delta\omega)(1 - \alpha L/2) \,. \tag{3.6}$$

Plugging (3.6) into (3.1), and neglecting second order small terms, we have

$$\frac{dE_0(t)}{dt} + \left(\frac{1-p}{p\tau_0} + \frac{c\alpha}{2n_s} + i\Delta\omega\right)E_0(t) = \frac{ir}{t\tau_0}E_{in}(t) \,. \tag{3.7}$$

According to the definition of the intrinsic and coupling Q-factors, we have

$\frac{c\alpha}{2n_s} = \frac{\omega_0}{2Q_{in}}$ and $\frac{1-p}{p\tau_0} = \frac{\omega_0}{2Q_{coup}}$, thus (3.7) becomes

$$\frac{dE_0(t)}{dt} + \left(\frac{\omega_0}{2Q_{coup}} + \frac{\omega_0}{2Q_{in}} + i\Delta\omega\right)E_0(t) = \frac{ir}{t\tau_0}E_{in}(t) \quad . \tag{3.8}$$

Suppose we fix the pump laser wavelength, the resonance field amplitude will be fixed, i.e. in steady state. Then we can drop the time derivative term on LHS of (3.8) and obtain

$$E_0(t) = \frac{ir/t\tau_0}{\left(\omega_0/2Q_{coup} + \omega_0/2Q_{in} + i\Delta\omega\right)}E_{in}(t) \quad . \tag{3.9}$$

Plugging (3.9) into (3.2) and using $p \approx 1$, we have

$$E_{out}(t) = E_{in}(t)\left[1 - \frac{\omega_0/2Q_{coup}}{\left(\omega_0/2Q_{coup} + \omega_0/2Q_{in} + i\Delta\omega\right)}\right]. \tag{3.10}$$

Therefore, we can deduce the field intensity transmission coefficient of the fiber taper as

$$T = \frac{|E_{out}(t)|^2}{|E_{in}(t)|^2} = 1 - \frac{4Q_{in}Q_{coup}}{(Q_{in} + Q_{coup})^2 + (Q_{in}Q_{coup}\Delta\omega/\omega_0)^2} \quad . \tag{3.11}$$

After the micro resonator is fabricated, Q_{in} is determined and fixed by the intrinsic loss mechanisms. However, Q_{coup} can be altered by different coupling conditions which are achieved by varying the gap between the fiber taper and micro resonator. The larger the gap the less likely the light leaks back into the fiber taper and thus the higher Q_{coup} would be. Figure 3.3 shows the on-resonance (i.e. $\Delta\omega = 0$) transmission coefficient of field intensity

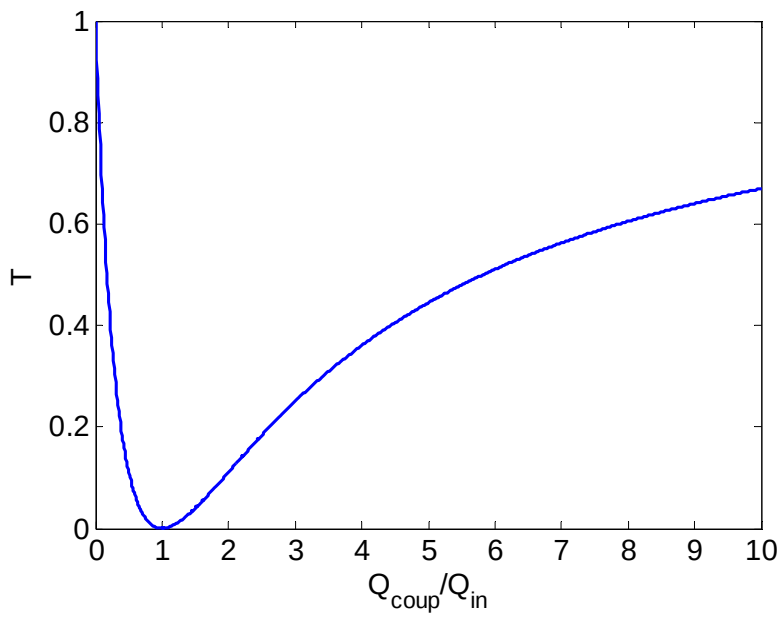

Figure 3.3 Dependence of on-resonance transmission coefficient of field intensity in fiber taper on ratio between Q-factors resulted from coupling loss and intrinsic loss, respectively.

in fiber taper changing with the ratio of Q_{coup} / Q_{in}. The WGM coupling is commonly characterized by over-coupled, critically coupled and under-coupled according to Q_{coup} / Q_{in}. The characteristics of the three regimes of couplings are

(I) Over-coupling:

Over-coupling starts from that the fiber taper directly touches the resonator to fairly small gap between them. The effect of light coupling back from resonator into fiber taper is

strong. The total Q-factors are the lowest among the three regimes of coupling. As shown in Figure 3.3, as the resonator moves away from the fiber taper, Q_{coup} increases but smaller than Q_{in}, and the transmission coefficient T of fiber taper decreases and approaches zero.

(II) Critical-coupling:

Critical coupling is the point where a certain gap is achieved between fiber taper and micro resonator so that $Q_{coup} = Q_{in}$. The total Q-factor is $Q_{in}/2$. The light in the fiber taper is fully attenuated (i.e. T=0) after the coupling when it is on resonance (i.e. $\Delta\omega = 0$). Thus, this coupling is also regarded as the most efficient or optimized.

(III) Under-coupling:

The effect of light coupling back from resonator into the fiber taper becomes weak. The total Q-factors are larger than $Q_{in}/2$ and are the highest among the three regimes of coupling. As the resonator moves further away from the fiber taper starting from the critical-coupling point, Q_{coup} keeps increasing and $Q_{coup} > Q_{in}$, transmission coefficient T of fiber taper increases. As $Q_{coup} \to \infty$, the total Q-factor approaches Q_{in}, however, T approaches 1 which means that almost no light can be coupled into the resonator for WGM.

Guo *et al.* [48] have obtained the three coupling regimes through a finite element (FEM) based numerical simulation for coupling light from a micro planar waveguide to a microdisk. As shown in Figure 3.4, as the gap increases from 0 to about 1000nm, the normalized energy stored in the microdisk first increases from zero to the unity (i.e., all the energy in the waveguide is lost into the microdisk) and subsequently it decreases to zero again. The loaded Q-factor monotonically increases with the gap which is actually due to

that Q_{coup} keeps increasing with increasing gap. This description of the near-field gap effect is consistent with the description of the coupling regimes and with the variation of the on-resonance transmission coefficient shown in Figure 3.3. An experimental demonstration of gap-effect/coupling regimes will be shown in Chapter 4.

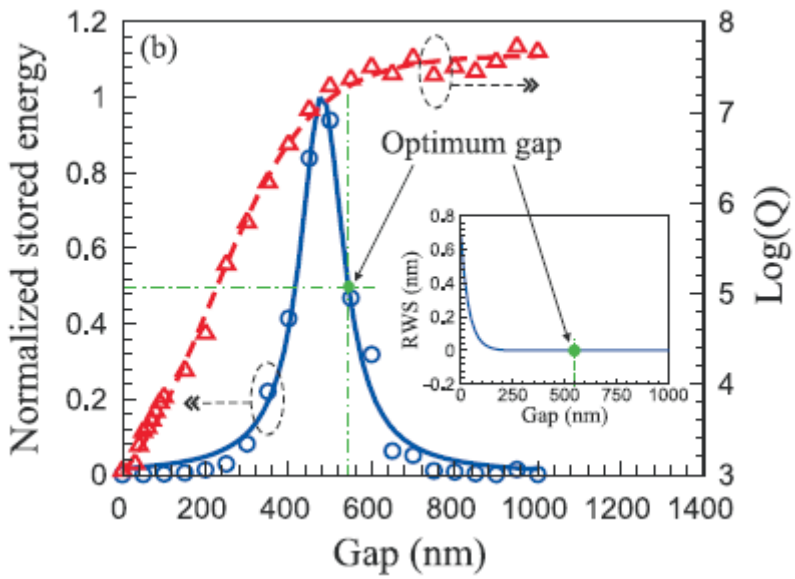

Figure 3.4 Gap effect on energy storage and resonance quality for a 10μm diameter microdisk coupled with a 2μm wide waveguide working on the 801nm resonance mode [46].

3.4 Size-matching for efficient coupling between fiber taper and spherical micro resonator

The discussion in section 3.3 does not deal with the diameter of the fiber taper. Only the relation between the intrinsic and coupling Q-factors is used to characterize the transmission coefficient. The coupling is regarded efficient when most of the power in the fiber can be loaded into the micro resonator on resonance. This happens most likely when fundamental WGM (i.e. $|m| = l$, $n = 1$) is excited, which is confined most closely to the surface of the resonator and to the resonator equator. We need to match the propagation

constant of the WGM at the surface of the resonator with the propagation constant of the appropriate mode in the fiber taper, which is essentially matching the waist size of fiber taper required for efficient excitation of WGM with a specific size of micro resonator. The propagation constant of a WGM with mode number *n*, *l* and *m* can be approximated as [40]

$$\beta_{WGM} = kl / x_{nlm} \tag{3.12}$$

where *k* is the free-pace propagation constant, x_{nlm} is the size parameter of a resonator. In the case of fundamental WGM, we have $x_{nlm} = 2\pi R_0 / \lambda$. The value of *l* can be calculated according to the various value of *n* for a resonator of given radius R_0 and refractive index n_s by solving the asymptotic expansion of morphological resonance frequencies in Mie scattering [42]:

$$x_{nlm} = \frac{l+1/2}{q} - \frac{\zeta_1}{q}\left(\frac{l+1/2}{2}\right)^{1/3} + \sum_{i=0}^{7} \frac{d_i(q,\zeta_1)}{(l+1/2)^{i/3}(q^2-1)^{(i+1)/2}} \tag{3.13}$$

where $q = n_s / n_a$, n_a is the refractive index of the surrounding air. ζ_1 denoates the first zero of the Airy function. The coefficients d_i depend on polarization (TE or TM) of the mode. To excite TE modes which have the strongest WGM coupling, we have

$$d_0 = -1$$

$$d_1 = 2^{1/3} 3(q^2-1)\zeta_1^{\,2} /(20q)$$

$$d_2 = 2^{2/3} q^2 \zeta_1 / 6$$

$$d_3 = \frac{-2^{1/3} q^2 \zeta_1^{\,2}(4-q^2)}{20}$$

$$d_4 = \frac{\zeta_1[40(-1+3q^2-3q^4+351q^6)-479(q^2-1)^3\zeta_1^{\,3}]}{2^{4/3}63000q}$$

$$d_5 = \frac{5q^2(-13-16q^2+4q^4)+2q^2(128-4q^2+q^4)\zeta_1^{\,3}}{1400}$$

$$d_6 = \frac{\zeta_1^{\,2}[100(-551+2204q^2-3306q^4-73256q^6+10229q^8)-20231(q^2-1)^4\zeta_1^{\,3}]}{2^{2/3}16170000q}$$

$$d_7 = \frac{q^2\zeta_1[10(11082+44271q^2-288q^4+7060q^6)-3(52544+48432q^2-11496q^4+2395q^6)\zeta_1^{\,3}]}{2^{10/3}141750}$$

The propagation constant of the fundamental mode in the fiber taper is a function of the radius of the fiber taper waist and can be expressed as [40]

$$\beta_{taper}^2 = k^2 n_s^2 - (2.405)^2 / \rho^2 \tag{3.14}$$

where ρ is the radius of the fiber taper waist. Then we can set $\beta_{WGM} = \beta_{taper}$ to solve for ρ. By using $n_s = 1.4682$ (refractive index of Corning SMF-28 fiber) and $n_a = 1$, we obtain Figure 3.5 for the size-matching for efficient fundamental mode coupling. It can be seen that the smaller the resonator the smaller the taper waist should be for efficient coupling. Humphery *et al* recently claimed that the highest coupling from a fundamental fiber mode to a fundamental resonator WGM mode is achieved with a fiber taper that has a radius about 30% smaller that the result predicted from phase-matching as shown by Figure 3.5.

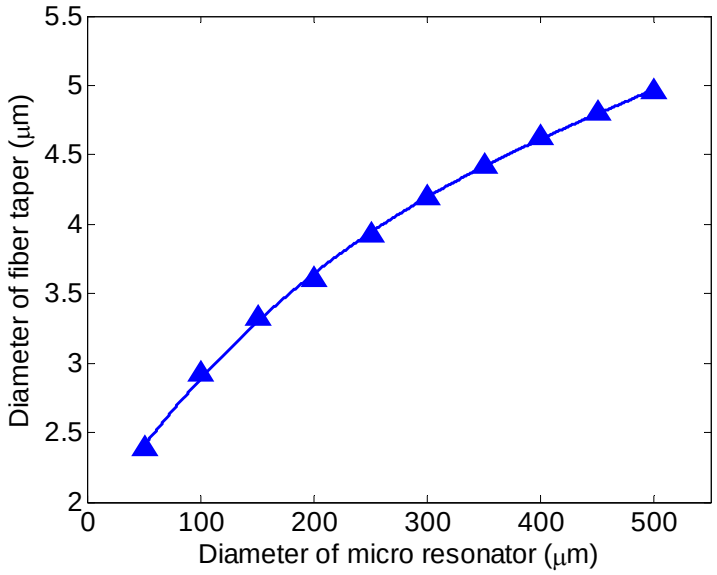

Figure 3.5 Fiber taper and micro resonator size-matching for efficient fundamental mode coupling.

CHAPTER 4

FABRICATION AND CHARACTERIZATION OF WHISPERING GALLERY MODE SYSTEM

4.1 Introduction

In this chapter, the fabrications of fiber taper and microsphere are presented. An oxy-hydrogen flame system is constructed and a CO_2 laser system is tested for the fabrication of the spherical micro resonator i.e. a microsphere. For the fabrication of fiber taper, a computer-based programmable heat-and-pull system as well as a hydrofluoric acid etching system is built. The fabrication procedures and key criteria are introduced for both the microsphere and fiber taper which are examined by both digital optical microscope and scanning electro microscopy (SEM). High quality fiber tapers with sub-micron waist size and negligible tapering loss are produced by heat-and-pull. Different sizes of microspheres with nanoscale roughness are fabricated. Transmission spectrums are recorded for characterizing the coupling between different sizes of fiber taper and microsphere. FSR of WGM is observed. A fiber polarization controller is used to optimize the coupling and to switch between TE and TM mode coupling. The three coupling regimes as mentioned in chapter 3 are achieved by fine tuning the coupling gap in nano scale.

4.2 Fabrication of microsphere

A high quality micro resonator for high Q-factor optical whispering gallery mode is made by melting the tip of a stripped and cleaned optical fiber with very clean heating

source. The surface tension shapes the melted material into a spherical form which we call a microsphere.

4.2.1 Preparation of the fiber

In the ultraviolet regime metallic impurities degrade the transmittance while in the infrared water is the principal contamination. Years of development of fiber optic communication has led to industrial production of very high quality (<5ppm –OH), very low absorption silica. The material we used for microsphere fabrication is an optical single mode fiber, which is usually composed of core, cladding, buffer/coating and jacket as shown in Figure 4.1. The specific one we use is Corning SMF-28e ultra-low loss (<0.19dB/km for telecommunication band 1525nm~1575nm) bare fiber, which actually contains only core, cladding and buffer. The core and cladding are 8.2μm and 125μm in diameter, respectively. Both of them are made of slightly doped synthetic fused silica and the cladding has slightly lower (0.36% less) refractive index. The refractive index of the core and cladding are 1.47 and 1.4647, respectively. The buffer is made of Corning CPC protective polymeric coatings with a diameter of 245μm.

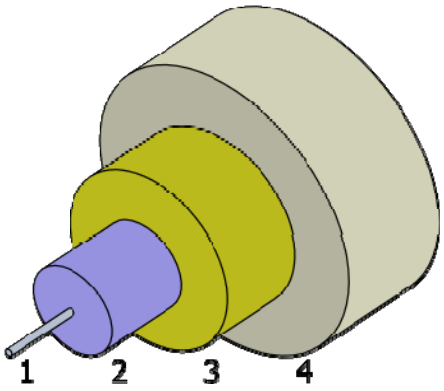

Figure 4.1 Schematic of the structure of a typical single mode optical fiber: 1.core 2.cladding 3.buffer/coating 4.jacket.

The procedures for preparing clean fiber rod used for melting are as following:

(I). Stripping of the fiber coating and cleaving of the fiber. The polymeric coating can be totally stripped off using a single mode fiber stripper (Clauss CFC-2). In addition, the fiber is then cleaved using an ultrasonic fiber cleaver (Photon Kinetics FK11) to make a flat tip cross-section.

(II). Initial cleaning using ethanol and glassware detergent. Residuals of polymer coating, dirt, grease and dust collect on the stripped fiber surface must be removed. The easiest way is by repeatedly and slowly scrubbing the surface using a delicate task wiper (Kimwipes) with glassware detergent Liqui-Nox (Alconox) and 100% ethanol. The fiber can be very well cleaned without any scratch on the surface.

(III). Ultrasonic cleaning. After the initial cleaning, the fiber is dipped into 100% ethanol in a small glass beaker. The beaker is then suspended in the bath of an ultrasonic cleaner (Fisher Scientific FS20) for 5 minutes, which further removes any residual attachments on the fiber after the scrubbing.

(IV). Drying by duster spray. After the ultrasonic cleaning, the fiber is dried quickly using a pure duster spray.

A good method to examine the cleanliness of the fiber is by heating the end of the fiber until it glows white hot. This launches white light down the fiber, illuminating any defects on the fiber surface. Figure 4.2 (a) and (b) show a clean and an unclean fiber, respectively, using this method. The clean fiber is dark above the heating point until the location where the stripping starts, while the unclean one has many bright surface scattering centers which illuminate the fiber.

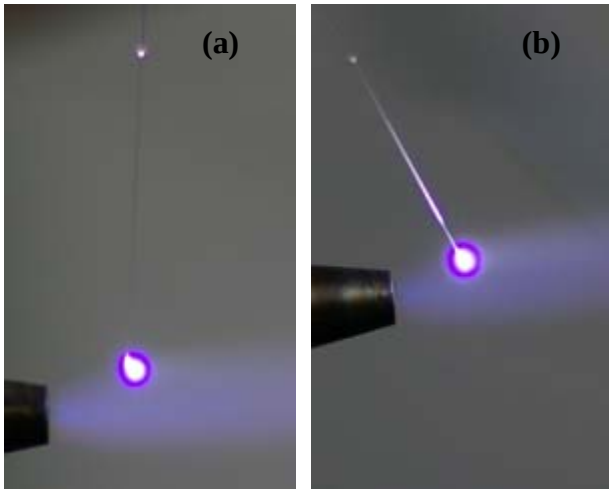

Figure 4.2 Stripped fiber under heating illumination (a) clean, (b) unclean.

After the cleaning procedure, we have examined the fiber under a digital optical microscope as shown in Figure 4.3(a). By adjusting the illumination exposure, we can clearly differentiate the core and cladding. The flat cross-section of the fiber is also examined using scanning electron microscopy (SEM) as shown in Figure 4.3 (b). We have applied zero-point-of-charge technique for silica (dielectric material) so that no conductive coating is needed for SEM and the core can be clearly distinguished. Notice that the core takes a small portion (0.43%) of the fiber which is good for fabricating microsphere with relatively uniform materials. Since silica absorbs atmospheric water vapor and gets contaminated in air, a stripped and cleaned fiber should be exposed in air for least amount of time before used for fabrication.

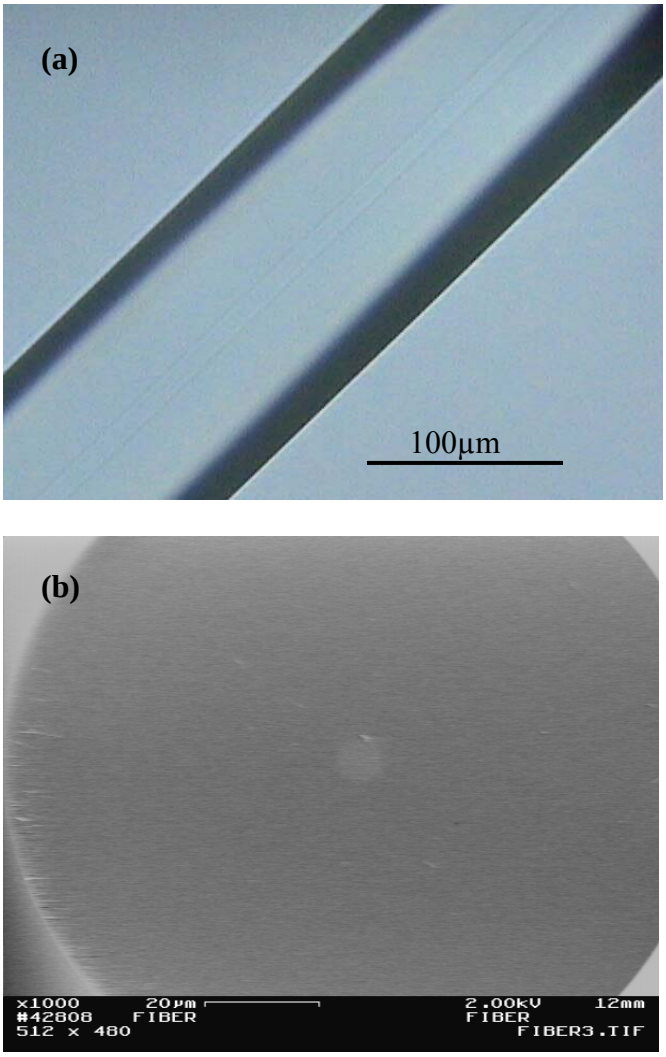

Figure 4.3 (a) SMF-28e fiber under digital optical microscope, (b) the cross-section of the SMF-28e fiber under SEM.

4.2.2 Formation of the silica microsphere

The silica microspheres are fabricated by melting the tip of the prepared fiber and the liquid surface tension forms a microsphere from the tip. Extremely clean heating source free of soot must be used. We have tried both CO_2 laser and oxy-hydrogen flame.

(I) Fabrication using CO_2 laser

The laser we used is 10.6μm, 20W, CW CO_2 laser (MPB Technologies). The beam is focused by a ZnSe focusing lens. The fiber is positioned perpendicular to the laser beam and held by a 3-dimensional translation stage. As shown in Figure 4.4, from (a) to (h), the fiber is moved into and out of the focal point. During the movement, the fiber below the focal point is melted and attracted upward to form the sphere. However, some smoke comes out during this process which indicates that some amount of silica is burned instead

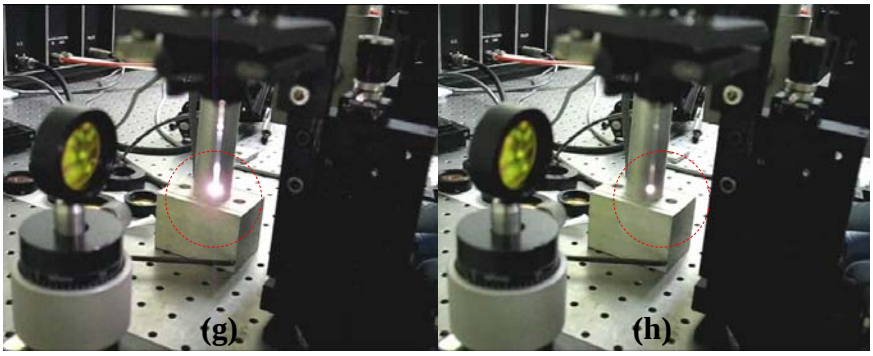

Figure 4.4 Microsphere forming process with CO_2 laser heating, from (a) to (h) the fiber is moved into and out of the focal point of the laser.

of being melted. This may spoil the quality of the sphere. A sample of the microsphere with diameter of 600μm (measured by the digital microscope) made by this method is shown in Figure 4.5. It can be seen that the sphere is not so spherical and black contamination resulted from burning can be clearly seen on the fiber stem. Due to the lack of appropriate attenuator and fine control of the laser power, we switched to oxy-hydrogen flame fabrication.

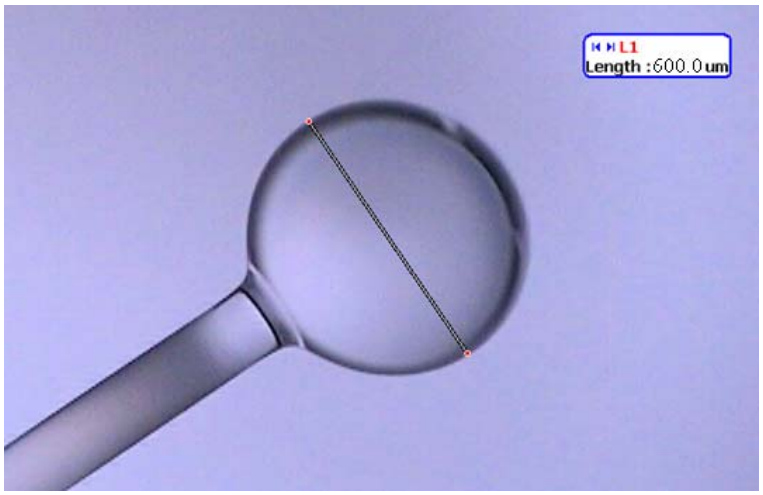

Figure 4.5 Microsphere (Diameter=600μm) formed on tip of the fiber by CO_2 laser heating.

(II) Fabrication using oxy-hydrogen flame

A safe and well controllable oxy-hydrogen torch system is constructed as shown in Figure 4.6. Ultra pure oxygen and hydrogen (Airgas) in cylinders are used. The oxy-hydrogen torch is a premixed type with flow control valves for the fuel and oxidizer. The nozzle is exchangeable and the one for microsphere fabrication has an opening of 2mm in diameter. A small pilot torch which burns pure hydrogen is fixed on the table for ignition of the main torch. Once an appropriate flame for fabrication appears by adjusting the flow controls, the flame can be quenched by putting the torch on the hanger and be reignited by taking off from hanger and igniting on the pilot flame. Output pressures from the cylinders are regulated at around 5psi for both hydrogen and oxygen. In addition, flashback arrestors are connected after the regulators for safety.

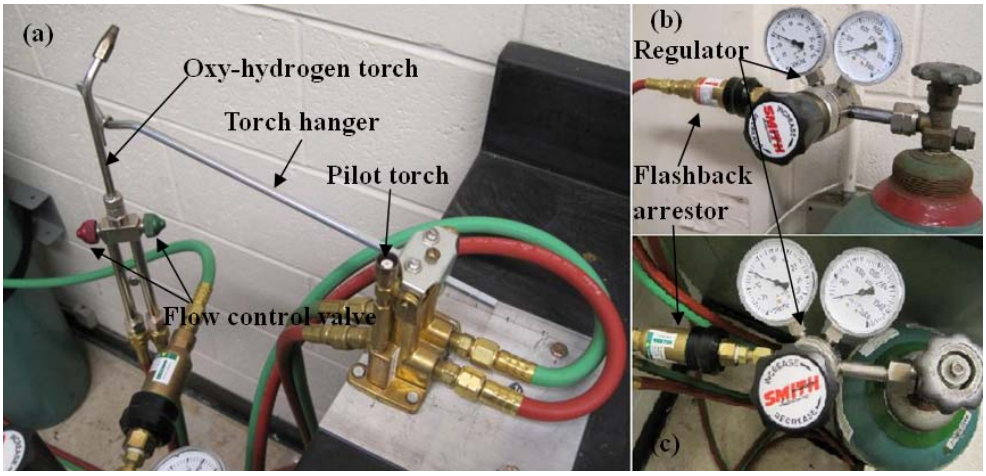

Figure 4.6 Adjustable oxy-hydrogen torch system (a) oxy-hydrogen, torch hanger and pilot torch (b) hydrogen regulator and flashback arrestor (c) oxygen regulator and flashback arrestor.

The flame temperature can be easily controlled by adjusting the combustion ratio of oxygen and hydrogen, varying from about 2400K (hydrogen in air) to about 3080K (stoichiometric mixture of oxygen and hydrogen). And the power can be controlled by varying the gas flow rates. The ideal flame should appear blue and approximately 3 inches long as shown in Figure 4.7, which also illustrates the melting of the fiber.

Figure 4.7 Fabrication of the microsphere by oxy-hydrogen flame.

During the fabrication, once the silica passes the melting point, surface tension shapes the material into a spherical form. At this point, the sphere glows hot white and it is then moved slowly out to a lower temperature part of the flame to do seconds of annealing. Annealing reduces the density variation and allows time for small surface variations being smoothed out by surface tension. And it solidifies immediately after fully getting out of the flame. The fused spheres can have a size about 50~500μm, depending on the size of the fiber being melted. By carefully melting a very thin fiber taper of about several microns in diameter, smaller spheres can be obtained. Figure 4.8 (a) shows a microsphere with diameter about 80μm fabricated from fiber taper under

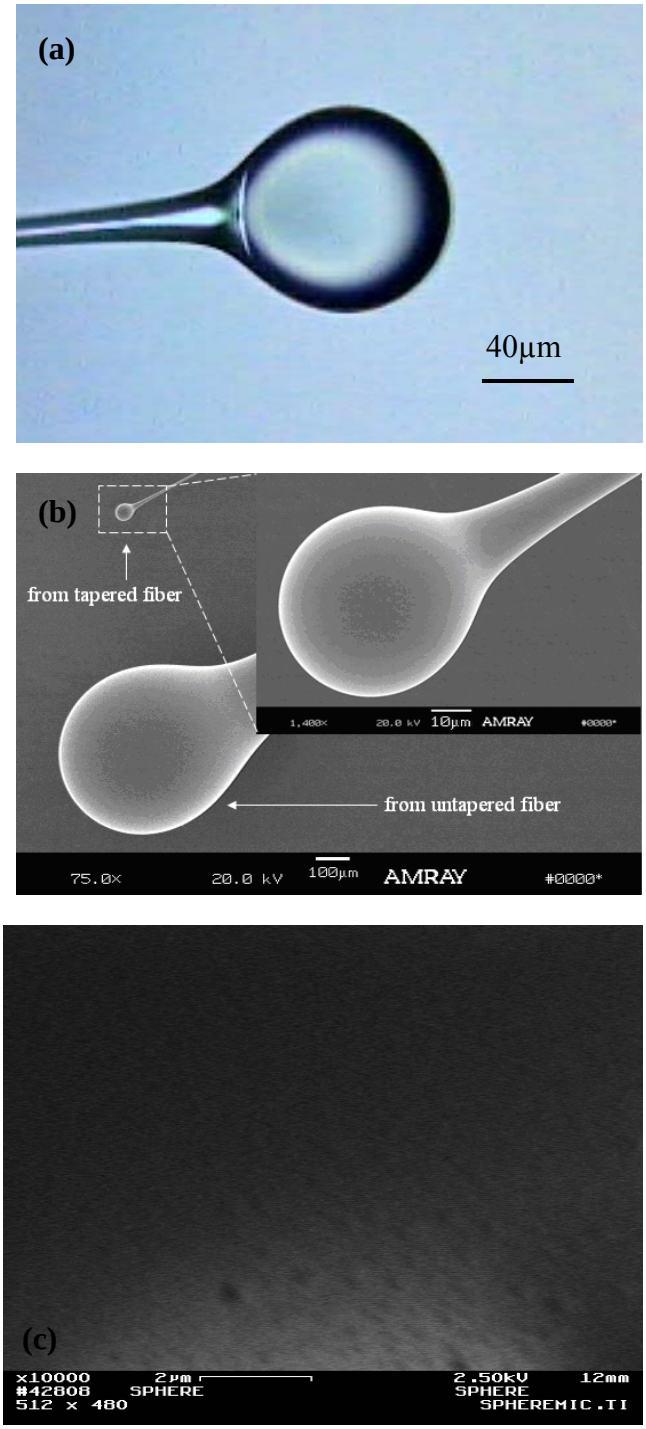

Figure 4.8 (a) A microsphere with diameter about 80μm fabricated from a fiber taper, (b) SEM image of two micro spheres (D≈50μm and 500μm , respectively) fabricated from an untapered fiber and a fiber taper, respectively, and (c) SEM image of the surface of a microsphere.

the digital optical microscope. In addition, Figure 4.8 (b) shows an SEM image of two microspheres (D≈50μm and 500μm, respectively) together which are fabricated from untapered and tapered fiber, respectively. Figure 4.8(c) shows the uncoated surface microstructure of the microspheres. Only nano-scale dips and bumps appears which proves the smoothness of the spheres.

4.3 Fabrication of fiber taper

An air-cladded fiber taper can expose the evanescent field of the propagating light inside it. There are two ways to achieve this: 1.removing the cladding 2.combining the core and cladding into one rod. Hydrofluoric (HF) acid etching and heat-and-pull methods are studied based on these two principles, respectively.

4.3.1 Method of HF acid etching

Hydrofluoric acid is an extremely corrosive liquid and is a contact poison. It should be handled with extreme care. Figure 4.9 shows the setup of fabricating fiber taper by HF acid etching. A Teflon container with inside diameter of 1cm is filled with 25% HF acid and a meniscus can be formed on top of the container due to surface tension. A stripped and cleaned fiber is aligned through the meniscus by the help of a 3D translation stage. A green light alignment laser is coupled into the fiber. The transmission signal is detected by a photodiode and monitored on an oscilloscope. The length of the etched region and taper slope can be controlled by changing the fiber position in the HF meniscus. It takes around 2 hours to drop the transmission power by 1/2~1/3 when the taper is finished. Then the taper is lifted up. To get smooth and undegraded taper, the taper needs to be rinsed in DI water to remove the acid residual right after etching. However, it is very difficult to get a very thin

taper (reaches down to 1μm in diameter) since the diameter of the taper decreases very fast when it etches to the size smaller than the initial core. The transmission loss due to tapering is also not negligible. Better control of the etched surface roughness and fiber taper slope needs modifying the HF concentration during the fabrication procedure which is not trivial to achieve. Due to all these drawbacks, we switched to the other technique, i.e. heat-and-pull.

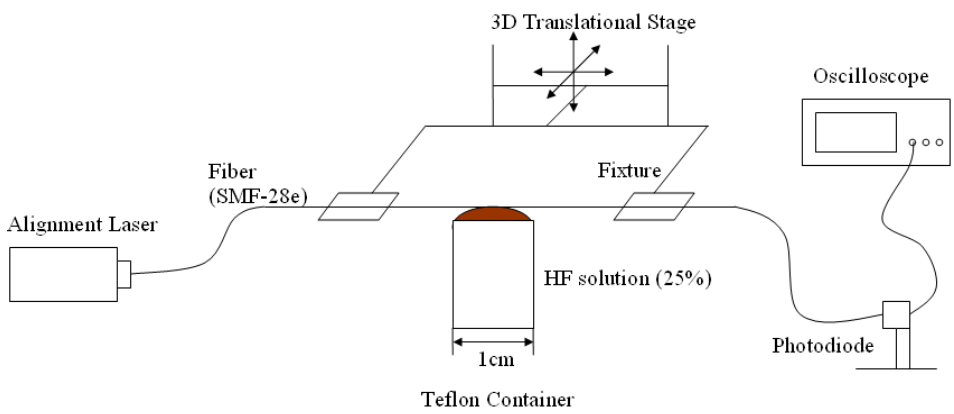

Figure 4.9 Setup of fiber taper fabrication by method of Hydrofluoric etching.

4.3.2 Method of heat-and-pull

Fabrication of fiber taper by heat-and-pull a SMF-28e optical fiber is much more successfully carried out. It combines the core and cladding into one rod in the tapered region, so that the evanescent wave can be effectively exposed. The heating source is pure hydrogen flame combusted in air. The torch nozzle with an opening of 0.8mm in diameter is used, so that the flame can be adjusted to very small and concentrated on the fiber less than 5mm. A fiber pulling system is constructed as shown in Figure 4.10. The step resolution of the stepper motor (AM17-44-3MT, AMS) is 1/8000 inch. Figure 4.11 shows whole setup of the fiber taper fabrication by the method of heat-and-pull. It should be

recognized that Dr. Lei Xu, a previous postdoctoral researcher in Dr. Guo's lab, has built the heat-and-pull instrument. The middle of the fiber is first stripped and cleaned. The fiber

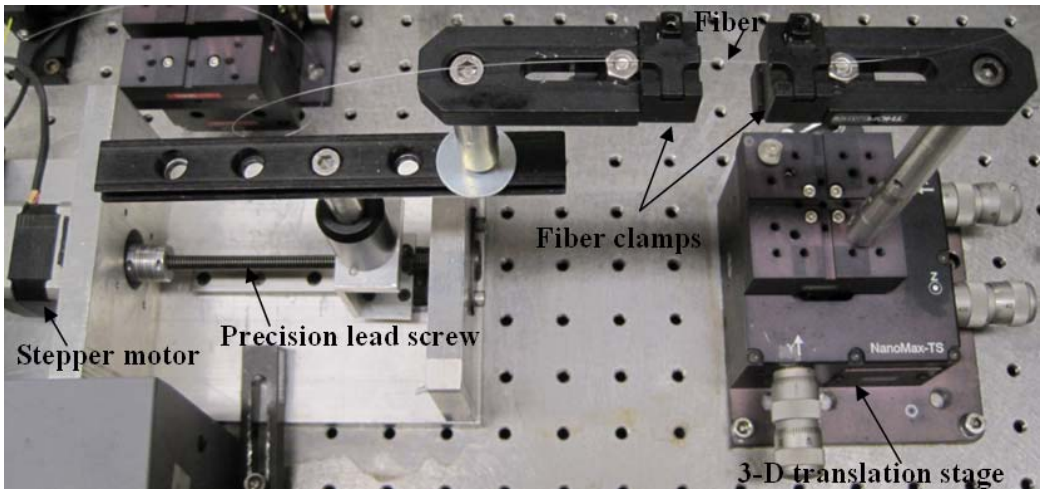

Figure 4.10 Photo of the optical fiber pulling system for fiber taper fabrication.

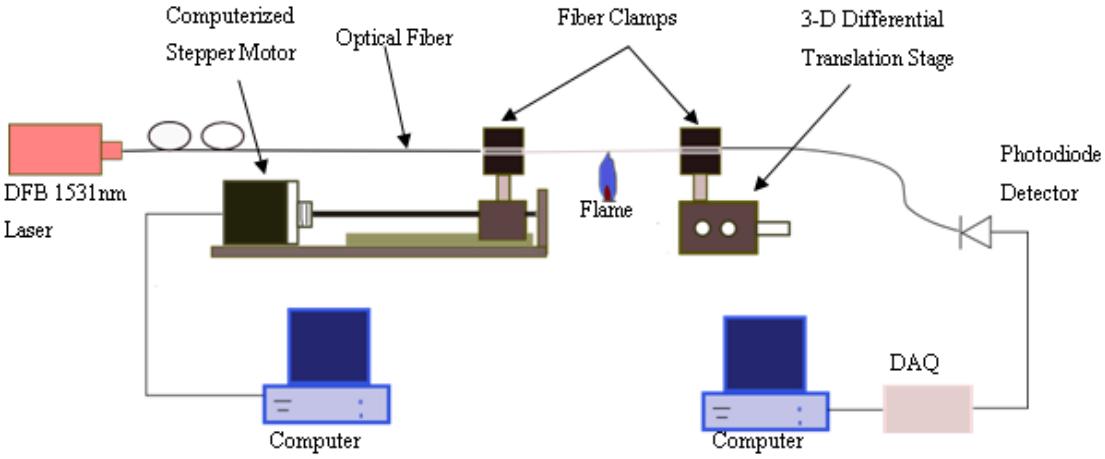

Figure 4.11 Setup of fiber taper fabrication by method of heat-and-pull.

is then fixed by two V-groove fiber clamps (HFF003, Thorlabs) on the pulling stage. One clamp is connected to the computerized programmable stepper motor, while the other one is fixed and supported on a 3-D differential translation stage (MAX313, Thorlabs) which

allows fine adjusting of the pulling alignment and post tensioning of the fiber taper. One end of the fiber is coupled to a DFB 1531nm laser (NEL NLK1556STG) and the output signal is detected by a photodiode detector (PDA400, Thorlabs). During the fabrication, the transmission signal is recorded and the hydrogen flame is brushed back and forth on the middle of the fiber between the fiber clamps. The stepper motor is usually programmed to pull the fiber by a length of 8000 steps (1 inch) in about 17s. The pulling starts with an initial speed of 150 steps per second (0.48mm/s) and accelerates to a finishing speed of 500 steps per second (1.59mm/s). A faster speed at the end can avoid the flame deflecting the thin taper too much. The flame should be moved away from the taper at the moment the motor stops. This procedure allows a uniform tapering of the fiber. A fiber taper of 1.5 to 2 inch long is usually obtained with a waist that can disperses red, orange, yellow, green, blue and violet color light under white light. The dispersion indicates that the fiber taper diameter has reached to sub-micrometer scale. We did SEM measurement to confirm the size. Figure 4.12 shows different fabricated fiber tapers and demonstrates that the waists can be as small as about 300nm. Figure 4.13 shows the uncoated cross-section of a fiber taper under SEM which proves that the core and cladding are already combined into one rod when the taper diameter reach to about 2.5μm. As shown in Figure 4.14, a typical transmission signal is recorded during the fabrication which indicates that the power loss due to tapering is negligible.

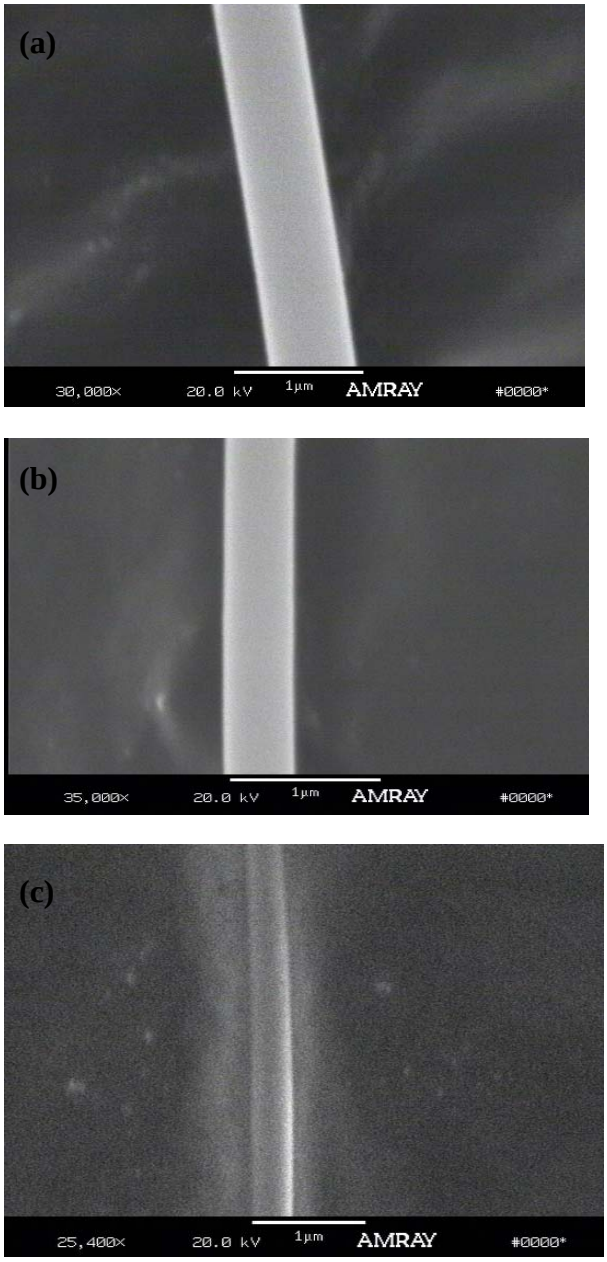

Figure 4.12 SEM images of the sub-micrometer fiber taper waists.

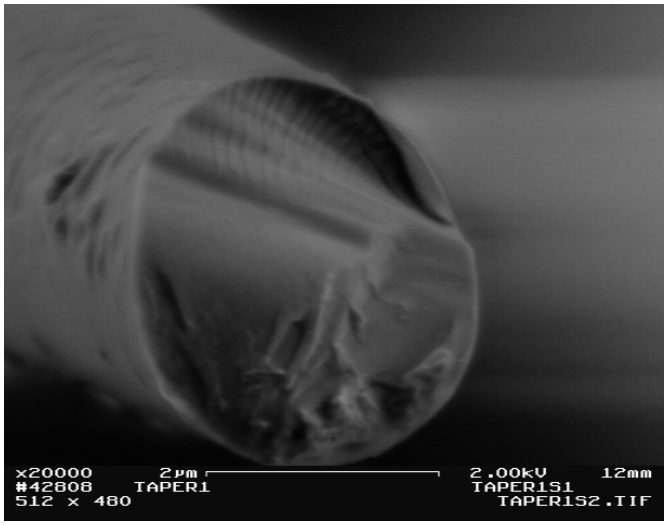

Figure 4.13 SEM image of the cross-section of a fiber taper.

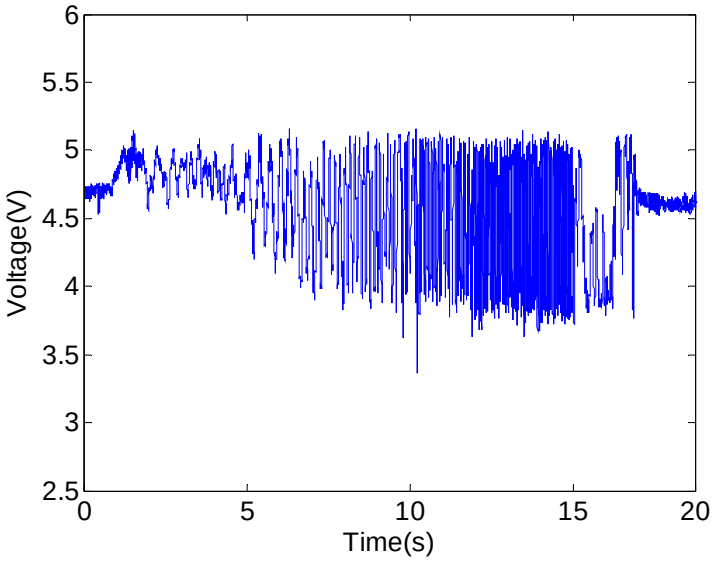

Figure 4.14 Transmission signal during the fiber taper fabrication.

To preserve a fundamental mode light propagation in the tapered region, the adiabatic condition must be met. It assumes that all changes in fiber profile occur over enough long distance so that there is a negligible change in the power of local mode. We have the beat length

$$z_b = 2\pi / \left|\beta_1 - \beta_2\right| \tag{4.1}$$

where β_1 and β_2 are the two closet propagation constants. Hence, the fiber nonuniformity must change over a distance large compared with z_b to ensure the fundamental mode propagation. For the single mode SMF-28 fiber, β_1 is the single mode propagation constant, while β_2 refers to a packet of radiation modes. And we can assume weakly guiding ($n_{co} \cong n_{cl}$) so that the upper bond of z_b can be expressed as

$$z_b \cong \frac{4\pi a V}{(2\Delta)^{1/2}\tilde{W}^2} \tag{4.2}$$

where a is the radius of the core, $V = \frac{2\pi a}{\lambda}\left(n_{co}^2 - n_{cl}^2\right)^{1/2}$ is the waveguide parameter, $\Delta = \frac{1}{2}\left(1 - \frac{n_{cl}^2}{n_{co}^2}\right)$ is the profile height parameter and modal parameter, n_{cl} and n_{co} are the refractive indices of the cladding and core, respectively, $\tilde{W} \cong 1.123\exp(-2/V^2)$ for step refractive index profile fiber. Plugging in parameters of SMF-28e fiber, a=4.1μm, λ=1.531μm, n_{cl}=1.4647 and n_{co}=1.47, we have z_b≅2.51mm. For all the tapers we fabricated we have the transitional tapered region much longer than 2.51mm and thus have preserved the fundamental propagation.

4.4 Characterization of the fabricated whispering gallery mode system

The fabricated microsphere and fiber taper are coupled for WGM. The FSR of WGM, fiber taper-microsphere size matching, switching between TM and TE WGMs and coupling regimes are experimentally studied to examine the performance of the coupling system.

4.4.1 Typical setup for WGM coupling

Figure 4.15 shows a typical setup of WGM coupling in this study. The DFB 1531nm tunable laser is tuned and coupled into the fiber taper. The microsphere is positioned by a 3D differential translation stage (MAX302, Thorlabs) which has a step resolution of 20nm. The coupling is manipulated under a long working distance stereo-microscope (SV8, Zeiss). The Transmission signal is detected by a photodiode detector (PDA400, Thorlabs)

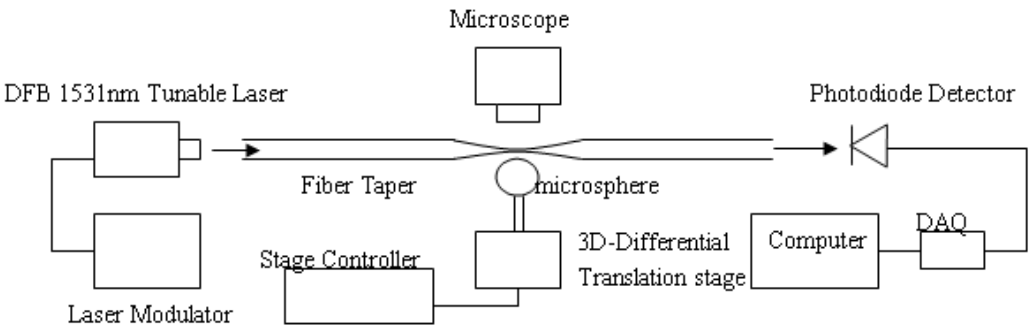

Figure 4.15 Schematic of a typical WGM coupling system.

and recorded by a computer equipped with data acquisition (DAQ). The output end of the fiber needs to be slightly angled cleaved to eliminate the etalon effect which results in significant oscillations on the sawtooth laser tuning curve. This setup modified a previous setup in Dr. Guo's lab in which the data acquisition was performed using an optical spectral analyzer (OSA) and the translation stage was updated. Figure 4.16 (a) shows etalon effect by a comparison between the transmission signals of the fiber without and with angle cleaved output end. The free spectral range of the etalon effect can be estimated as

$$\Delta\lambda = \frac{\lambda_0^2}{2n_{co}l} \tag{4.3}$$

where λ_0 is the central wavelength of the tuning, l is the length of the fiber. The wavelength spacing of etalon oscillation peaks in experiment observation which is consistent with the value $\Delta\lambda$ obtained from equation (4.3). This confirms that the oscillations result from the Fabry-Perot interference of the two fiber ends.

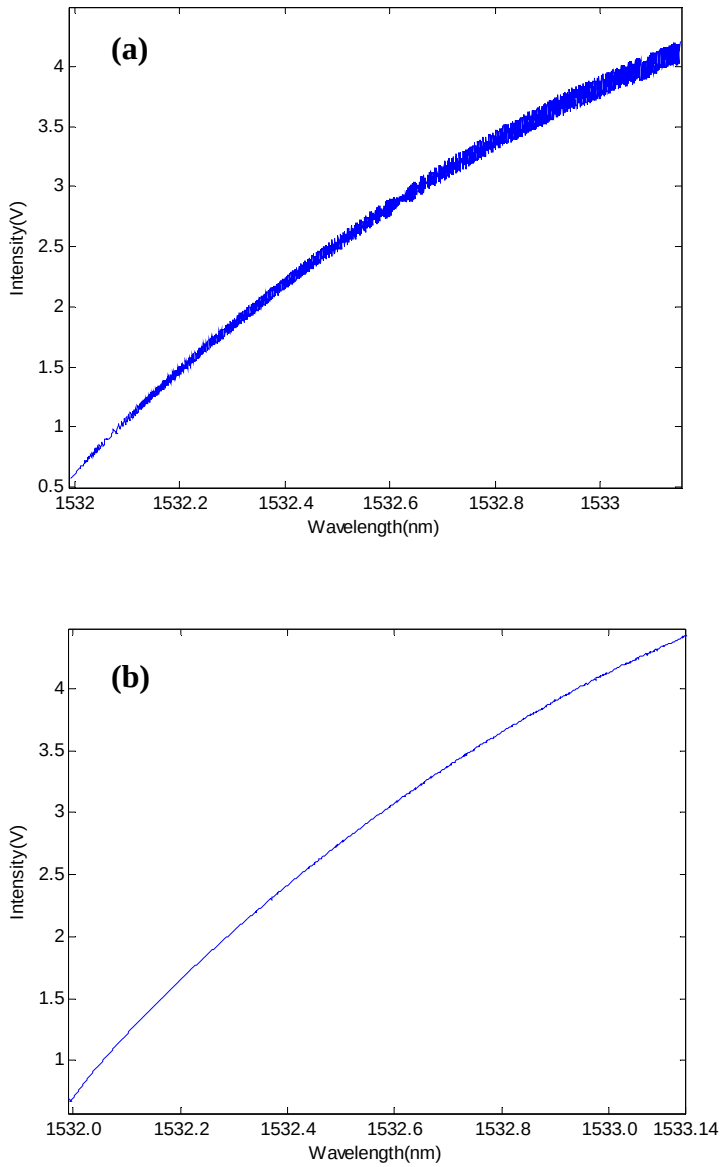

Figure 4.16 Transmission of the sawtooth laser tuning signal (a) with flat cleaved output end and (b) with angle cleaved output end.

4.4.2 Microsphere-fiber taper size matching of WGM coupling

As discussed in chapter 3, we are interested to excite fundamental modes with low n and $l \approx m$, which are the modes with smallest mode volume and most closely confined to the surface of the sphere and to the sphere equator. To get an efficient excitation of these WGMs, diameter of the fiber taper as well as the diameter of the microsphere must be chosen to match the propagation constants. According to the result in chapter 3, sphere with diameter about 50μm and 500μm match to taper waist with 2.4μm and 5μm, respectively. These two sphere sizes are the two limits of our fabrication by melting a single fiber or fiber taper. By directly touching the equator of the sphere to different parts of the taper waist with different diameters, various coupling spectra can be observed from the transmission signal. Figure 4.17 shows the spectrum of a microsphere with diameter about 58μm, 225μm and 490μm coupled to a taper waist that has blue light dispersion, no dispersion and green light dispersion, respectively. The wavelength tuning ranges are 1.11nm, 1.13nm and 1.27nm, respectively for the three cases. The case with D=58μm and 225μm are close to phase-matched coupling, since all the major modes can be clearly differentiated. However, the taper is too small for the case with D=490μm which result in an extremely crowded spectrum. The case with D=58μm clearly demonstrates that the taper waist diameter (<1μm) is much thinner than that predicted from matching the propagation constants. Since we have similar wavelength tuning ranges for the three cases, it is also demonstrated that the smaller the sphere the less WGM can be excited i.e. the smaller the mode volume.

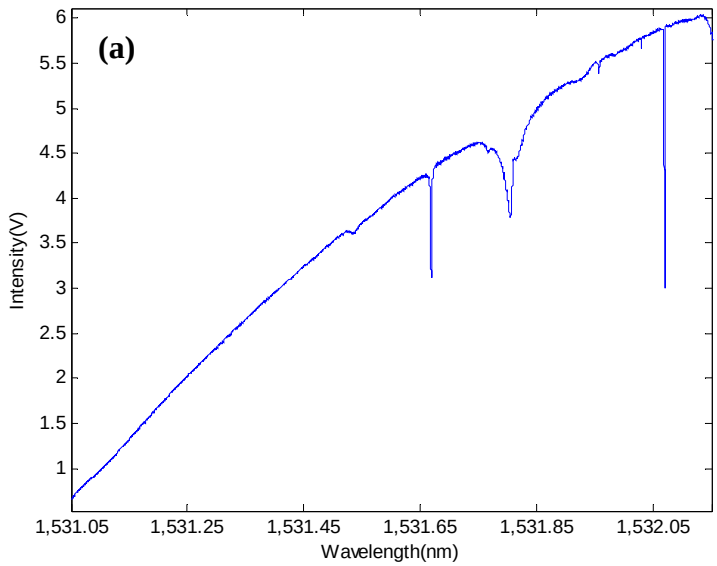
(a)
Intensity(V)
6
5.5
5
4.5
4
3.5
3
2.5
2
1.5
1
1,531.05
1,531.25
1,531.45
1,531.65
1,531.85
1,532.05
Wavelength(nm)

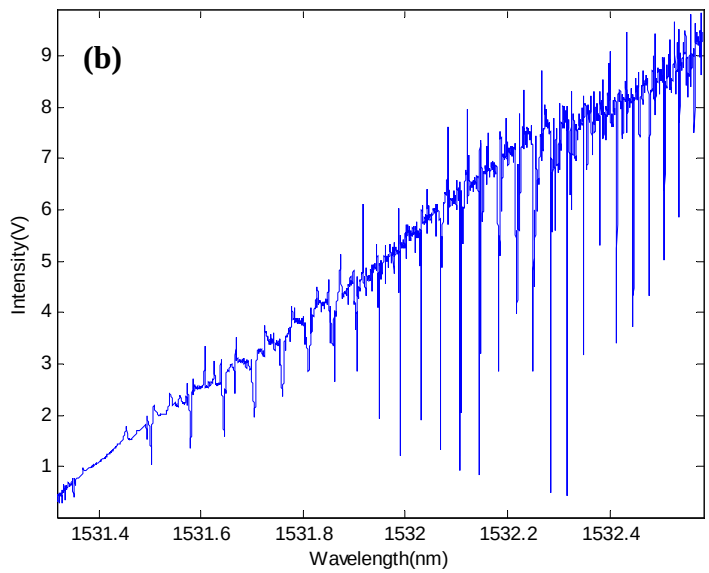
(b)
Intensity(V)
9
8
7
6
5
4
3
2
1
1531.4
1531.6
1531.8
1532
1532.2
1532.4
Wavelength(nm)

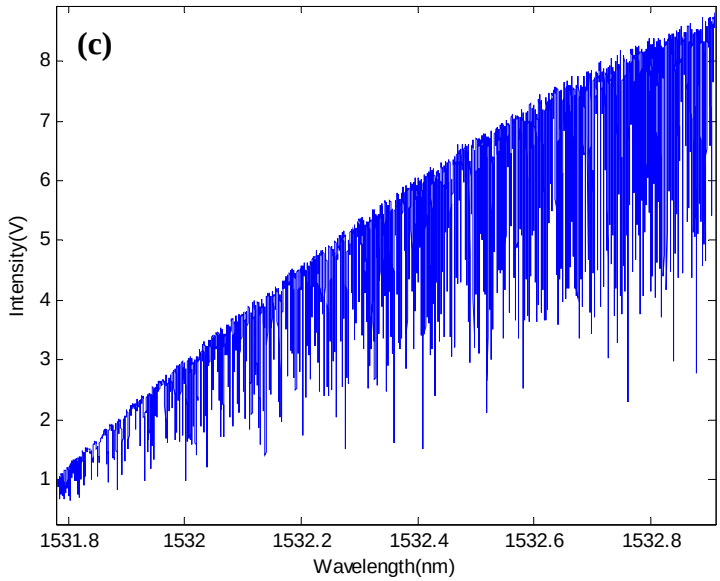

Figure 4.17 WGM spectra of a microsphere with (a) D=58μm, (b) 225μm and (c) 490μm coupled with fiber taper waist that locally has blue light dispersion, no dispersion and green light dispersion, respectively.

4.4.3 Observation of WGM free spectral range.

For our DFB laser, the injection current tuning of the wavelength at a constant control temperature is limited (~1.2nm). Wider tuning range can be realized by varying the control temperature while maintaining a fixed injection current tuning range. As the control temperature is adjusted, the window of injection current tuning scans through the wavelength and similar WGM patterns repeatedly appears. The wavelength spacing between the two similar adjacent patterns is the free spectral range of the WGM of a microsphere. As the example shown in Figure 4.18, for microsphere with diameter of 350μm, the difference between two corresponding dips is about 0.74nm. On the other hand, the FSR calculated by equation (2.4) ($\lambda_0 = 1.53\ \mu m$) is 0.72nm which is within an error of 3% from the experimental observation.

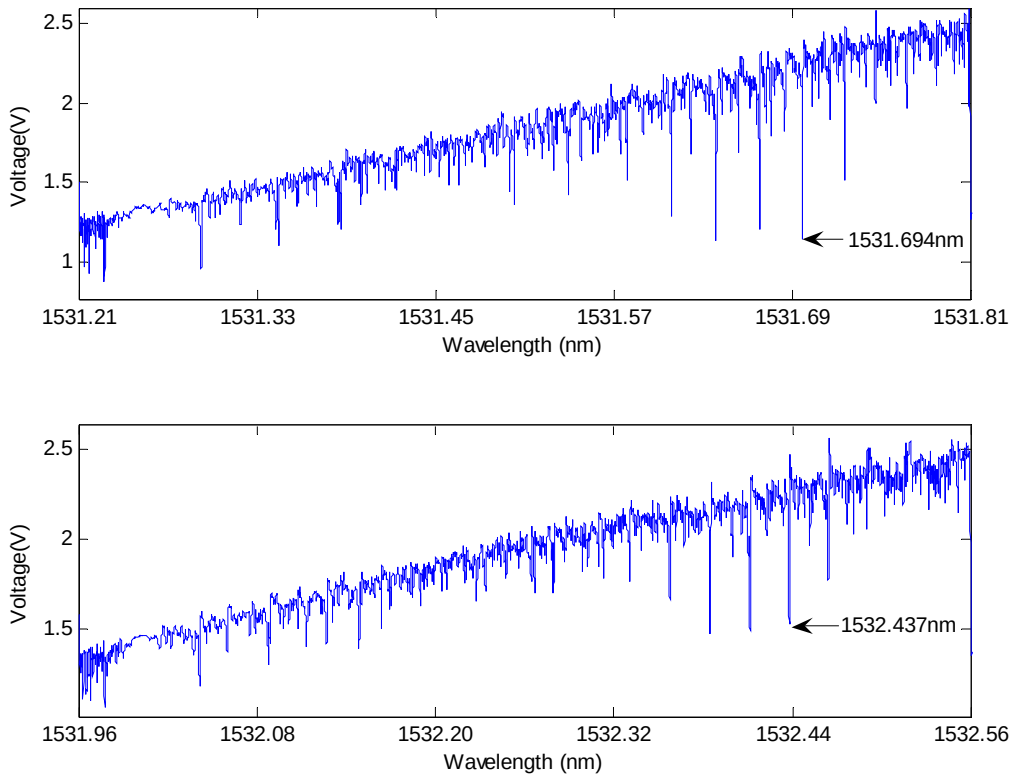

Figure 4.18 Two adjacent similar WGM patterns for a microsphere with D=350μm, the wavelength spacing between the two patterns is about 0.74nm which is the measured WGM FSR.

4.4.4 Switching between TM mode and TE mode coupling

Depending on the polarization of the laser in the fiber taper, TE or TM WGMs can be excited. Thus, to adjust the WGM resonance characteristics such as coupling coefficient, i.e., (1-*T*) (where *T* is defined in Chapter 3) and quality factor, it is very critical to control the polarization of the light being coupled into the microsphere. Although this can be realized by simply adjusting the relative position of the microsphere surrounding the fiber taper axis, micro scale manipulation for the coupling is time consuming and continuous adjustment of the polarization is not achievable. Fortunately, a fiber polarization controller which utilizes stress-induced birefringence to create three independent fractional wave

plates can be used to continuously alter the polarization of the transmitted light in single mode fiber. The fiber is looped into three independent spools as shown in Figure 4.19 (FPC561, Thorlabs). Rotation of the spools rotates the principal axis of birefringence producing controlled change in the polarization. The diameter and number of fiber loops of the spools are specified such that outer spools provide a spatial delay of $\lambda/4$ (quarter wave plate); and central spool provides a spatial delay of $\lambda/2$. The $\lambda/4$ spools control the ellipticity of the polarization and the $\lambda/2$ spool controls the direction of the polarization. This combination allows any state of polarization to be changed into another state of

Figure 4.19 Fiber polarization controller (Thorlabs).

polarization in a continuous way. This device is implemented between the laser and WGM coupling. By manually rotating the spools, we can realize the switching between excitations of TE and TM WGMs as shown in Figure 4.20. The microsphere has a diameter of 336μm and directly touches the fiber taper for coupling. As indicated by the arrows, from (a) to (f), peak 1 originally has its maximum coupling coefficient ($1-T \approx 0.56$) and gradually disappears. In contrast, the coupling coefficient of peak 2 initially is negligible but increases to a maximum ($1-T \approx 0.60$). The TE mode coupling is stronger than the TM mode coupling. Thus, Figure 4.20 shows a TM to TE WGMs switching.

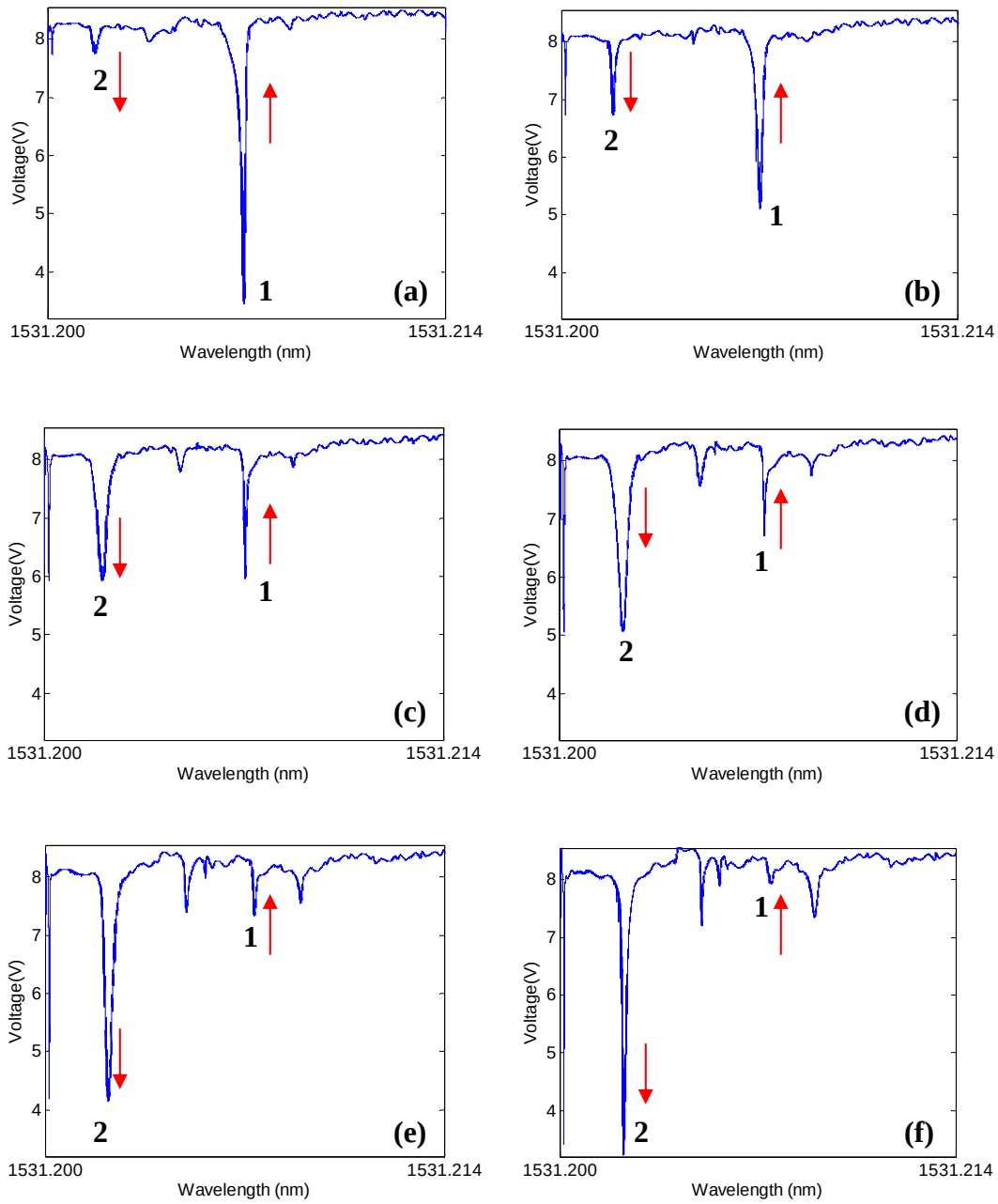

Figure 4.20 Switching from TM mode to TE mode coupling of WGM by a fiber polarization controller.

4.4.5 Observation of coupling regimes

As discussed in Chapter 3, a gap can be made between the microsphere and fiber taper to achieve different coupling regimes. However, in the initial experiment attempts, it is

found that the fiber taper always jump to touch with the microsphere when the microsphere gets close to it. This phenomenon should result from that Van der Waals and electrostatic forces pull the fiber toward to the fiber taper when they are close enough. To minimize this effect, two techniques are applied: 1. Maximum post tensioning of the fiber taper, as shown in Figure 4.10 and 4.11, the 3-D translation stage is used for finely tensioning the fiber taper. 2. Using a radioactive electrostatic charge eliminator (Staticmaster) in proximity of the coupling system to eliminate any charges on the system. The effect of fiber taper jumping onto the microsphere is efficiently reduced. With the differential translation stage of 20nm step resolution holding the microsphere, an efficient gap between the fiber taper and microsphere can be made. Figure 4.21 shows the coupling coefficient (1-*T*) varying with the gap. The diameter of the sphere is about 80µm. Three coupling regimes can be clearly distinguished. Point c is approximately the critical coupling point, where most of

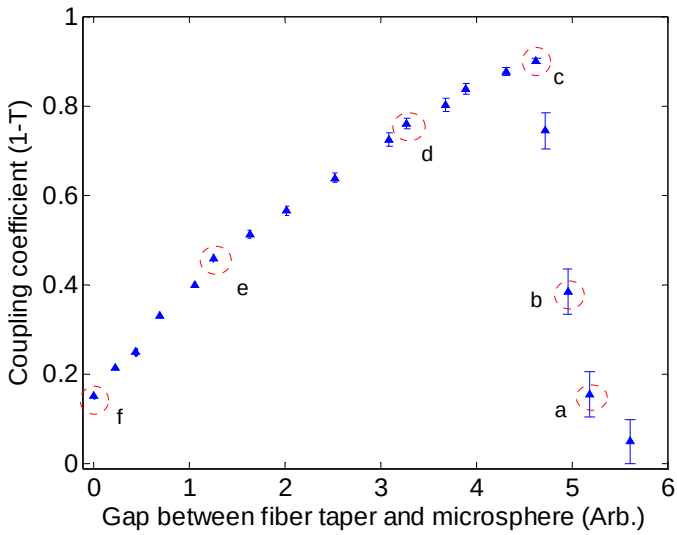

Figure 4.21 Coupling coefficients of a WGM with different gaps between the fiber taper and microsphere (microsphere diameter=80µm).

the power in the fiber is coupled into the microsphere. The measurements on the right and left of point c demonstrate under-coupling and over-coupling regimes, respectively. The

error bars are determined from the coupling coefficient variation in 0.5s of recorded signal at each position, which illustrate that the coupling coefficient becomes more stable as the sphere approaches the fiber taper. However, the real values of the gap can not be specified, since for current study it is not possible to determine the angle between the movement of the translation stage and the equator plane of the WGM resonance. Figure 4.22 shows the WGM profiles corresponding to the measured coupling points a ~ f in Figure 4.21. The linewidth increases from (a) to (f) and the corresponding total *Q*-factor decreases from 1.5×10^{7} down to 1.5×10^{5}. Thus, leaving a gap for varying the coupling coefficient and *Q*-factor is experimentally demonstrated.

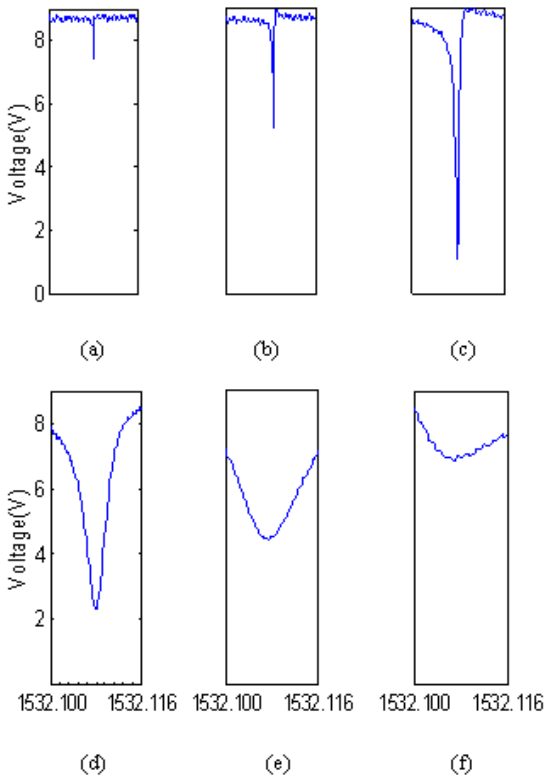

Figure 4.22 WGM dip profile in different coupling regimes with gaps (corresponding to points a ~ f in Figure 4.21). Q=1.5×10^{7}, 7.0×10^{6}, 2.0×10^{6}, 4.3×10^{5}, 2.1×10^{5} and 1.5×10^{5}, respectively, for (a)~(f).

CHAPTER 5

TEMPERATURE DETECTION OF WHISPERING GALLERY MODE

5.1 Introduction

Optical whispering gallery mode phenomena in dielectric micro-resonators have been extensively studied over the past decade for miniature sensors. Sensor applications which employ the interaction of the WGM evanescent component with an ambient analyte medium can be characterized into two categories: measurement of frequency/wavelength shifts of WGM resonance due to change of effective refractive index and/or size of resonator [18, 19, 32, 43-45], and measurement of the amount of resonator's quality factor spoiling [46] or change of coupling efficiency [47, 48]. The state-of-the-art optical technology enables optical frequency measurement down to the level of $\Delta f / f \sim 10^{-10}$, leading to the claim of extremely high sensitivity for nanoscale detection [18, 29 and 43]. However, sensor material properties such as thermal expansion and the thermo-optic effect are susceptible to thermal fluctuations caused by either ambient temperature variation or the absorption of laser energy during laser scanning or pumping. These effects may induce appreciable resonance frequency/wavelength shifts, and thus, need to be considered in the development of resonance shift sensing techniques. Cai *et al.* [49] found red shifts on the frequency of a single mode in a glass microchip laser when the pump power is increased and quantitatively explained the phenomenon based on the thermal expansion effect of the chip material. As stability and continuous operation are critical for use of a micro-resonator, Carmen *et al.* [50] demonstrated a self-stable thermal equilibrium solution for the

micro-cavity-pump system. Recently, Han and Wang [51] proposed qualitatively the use of a surface layer with a negative thermo-optic coefficient to compensate the thermal drift of a resonance frequency in an optical micro-resonator.

On the other hand, resonance frequency/wavelength shift induced by thermal effect can be utilized for temperature sensing. In early summer 2008 we started to work on WGM-based temperature measurements under the encouragement and first insight of Prof. Guo. In this chapter, we investigate the resonance wavelength shifts of fused silica microspheres with well-controlled temperature changes. The tests are done in a near room temperature range (room temperature to about 10K above) and in a wide temperature range from cryogenic temperatures (about 113K) to room temperature. Comparison between theory and experiments for sensitivities are addressed. The unique feature of ultra-high resolution of this kind of sensor and its other potentials are discussed.

5.2 Geometric optics modeling

Consider a WGM as a kth polygon in a micro-resonator as shown in Figure 5.1, which has a radius of R.

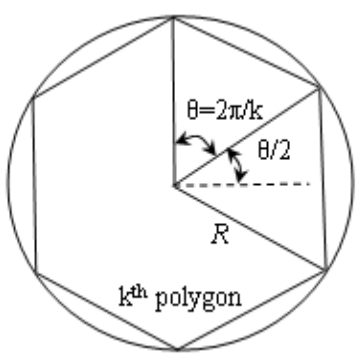

Figure 5.1 A WGM modeled as a kth polygon in a resonator.

Assume the azimuthal mode number is *m*, we have

$$k \cdot 2R \sin\frac{\pi}{k} = m\frac{\lambda}{n} \tag{5.1}$$

where λ is the resonance wavelength in vacuum and *n* is refractive index of the resonator. Then we have

$$\frac{dn}{n} + \frac{dR}{R} = \frac{d\lambda}{\lambda} \tag{5.2}$$

And we also have

$$\frac{dR}{R} = \alpha dT \text{ and } \frac{dn}{n} = \beta dT \tag{5.3}$$

where α and β are the linear coefficient of thermal expansion and thermo-optic coefficients of the resonator's material, respectively.

Plugging (5.3) into (5.2) gives

$$\frac{d\lambda}{dT} = (\alpha + \beta)\lambda \tag{5.4}$$

We define $d\lambda / dT$ as the temperature sensitivity which does not depend on the size of the resonator according to equation (5.4).

5.3 Near room temperature measurements

Figure 5.2 shows the diagram of our experimental setup. The micro-bead is precisely positioned by a 3D differential translation stage (MAX302, Thorlabs) to couple with the fiber taper in the cell. The fiber taper is held by two fiber clamps. The microsphere-taper coupling is observed under a stereo-microscope (SV8, Zeiss) to place the microspheres in contact with the taper for coupling. A DFB 1531 nm laser (NLK1556STG, NEL) is tuned and coupled into the fiber taper. The transmission signal is detected by a photodiode

detector (PDA400, Thorlabs) and recorded by a computer equipped with DAQ cards (National Instrument). A thermocouple (Omega K-type with 0.01" bead and 0.4 s time constant) in the cell is positioned about 0.1mm away from the microsphere to monitor the temperature change around the microsphere. The temperature measured by the thermocouple is recorded simultaneously with the recording of the WGM resonance spectrum with a temperature measurement module (National Instrument). The two DAQ cards are synchronized using a Master-Slave coding in LabView as shown in Figure 5.3. To get a high data resolution for the WGM spectra, the transmission signal is acquired at a fast rate of 1.25MHz, while the temperature measurement is acquired at a slower rate of 1000Hz. 0.1s of data is taken for each tested temperature point.

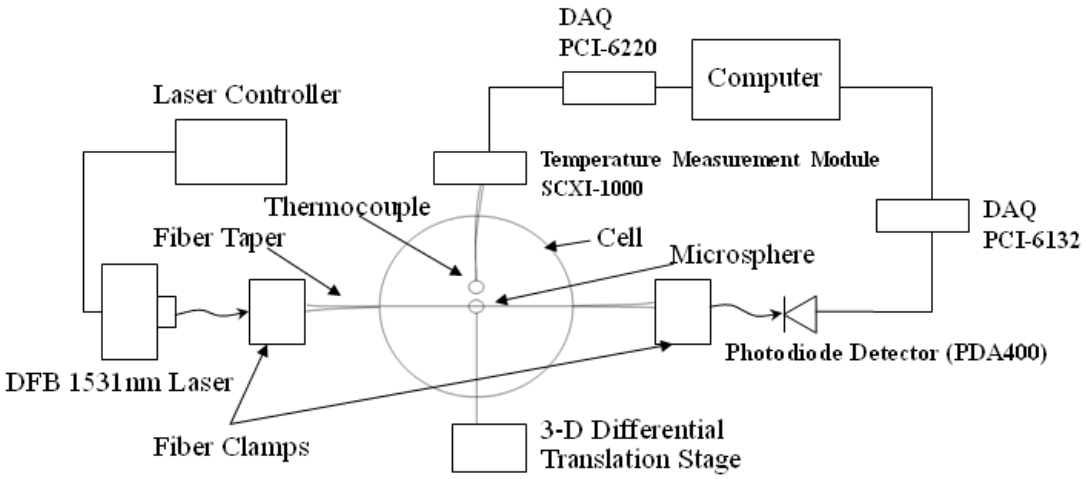

Figure 5.2 Diagram of the experiment setup.

Figure 5.4 shows a photograph of the working cell which is made of a plastic tube 1" in diameter and 2" in length. The accesses on the tube side for placing the fiber taper, thermocouple and micro-bead are sealed. The tube is wrapped with layers of delicate task wipers (Kimwipes) for thermal insulation. The top of the cell is covered by a transparent glass slide, avoiding environmental disturbance from the room to the cell. The bottom of

the cell is a 2mm thick aluminum plate which is glued to a copper plate with silicon paste to ensure excellent heat conduction. The copper plate is slowly heated up from room temperature. It takes about 3 min to steadily raise the air temperature in the cell monitored by the thermocouple by 1K. The air inside the cell is visually stagnant during the heating process with minimized heat convection effect. Uniform temperature increment and distribution in the micro-bead are important.

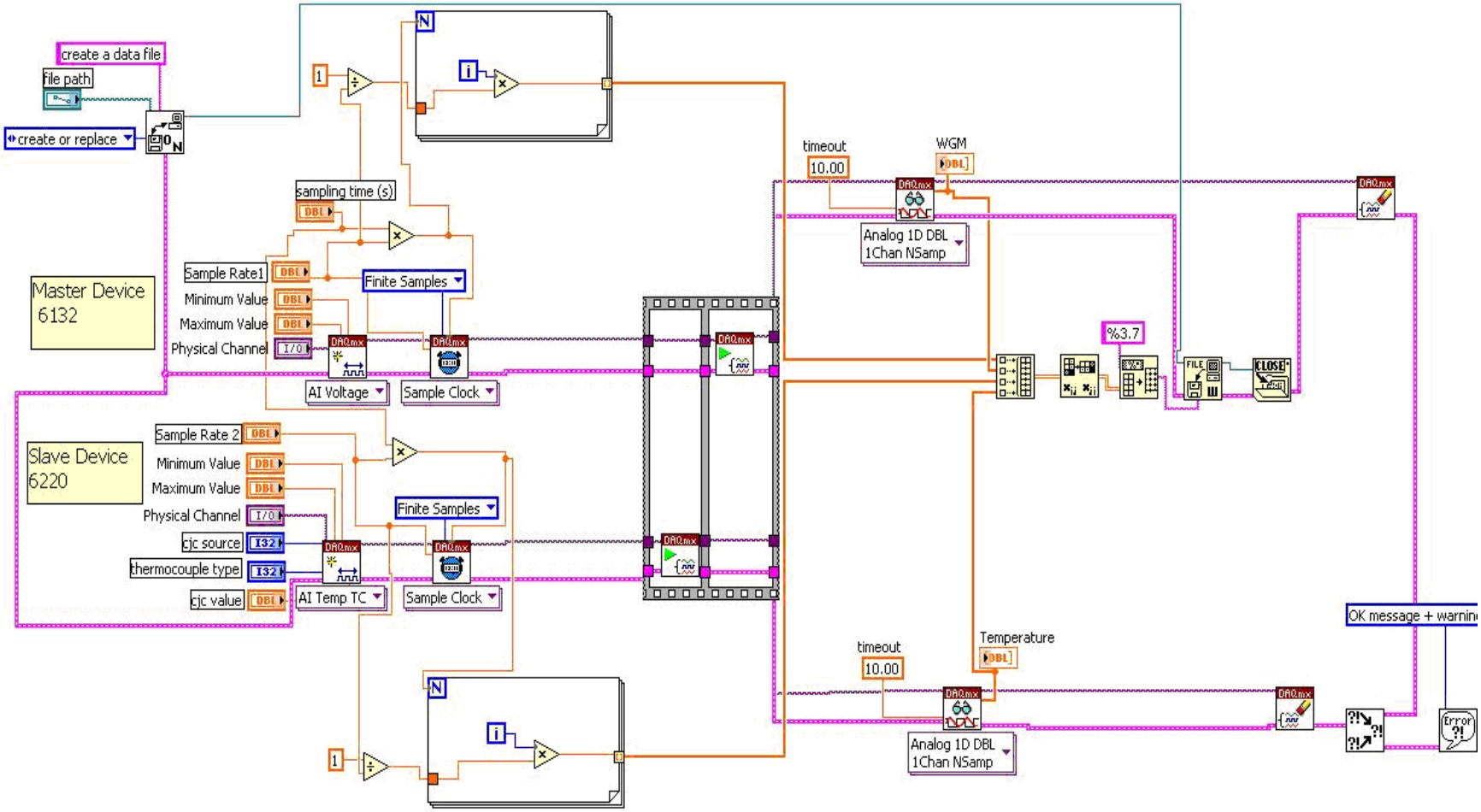

Figure 5.3 LabView Code for synchronizing Temperature and WGM spectrum data acquisitions.

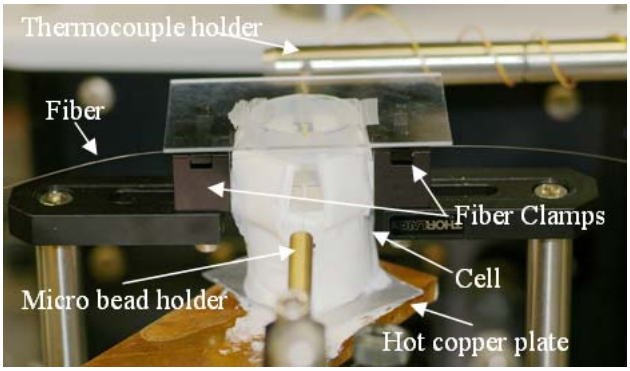

Figure 5.4 Photo of the working cell.

The need for an insulated working cell in the experiments is justified below. To test the influence of open air on the microsphere, we measured the dynamic shifts of a WGM resonance wavelength over 10s for a 105μm diameter microsphere suspended in free air of the lab room and in the working cell (at 298 K), respectively. The results of these two cases are compared in Figure 5.5. It is observed that the wavelength shift fluctuates with an amplitude of 5 pm for the case when the sphere is placed in free air; while the fluctuation amplitude is less than 0.2 pm for the case when the sphere is placed inside the cell. A reduction of 25 times in fluctuation is achieved when the working cell is utilized. From the later result in table 1, a shift of 0.2 pm in the WGM sensor corresponds to a temperature variation of about 0.017 K. A fluctuation of 5 pm in the case of open air results in a temperature error of 0.43 K. Thus, the use of the working cell effectively protects the WGM coupling system from ambient room disturbances (such as air convection and room temperature fluctuation) and improves significantly the temperature stability around the coupling system.

In order to let the microsphere, the thermocouple and the surrounding air be in thermal equilibrium during a measurement, the air in the cell has to be stable and the air

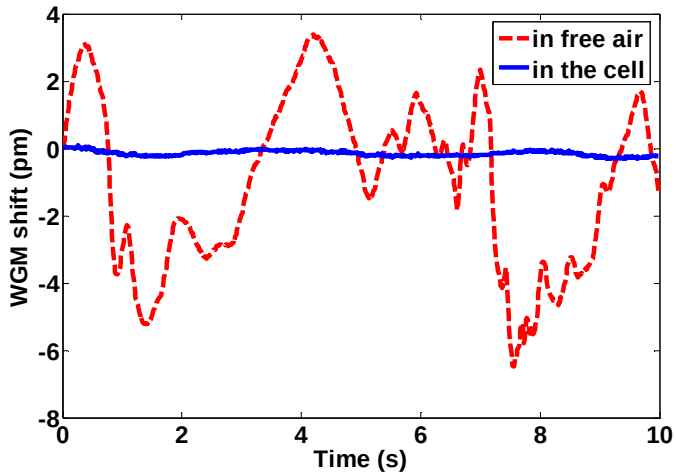

Figure 5.5 The measured dynamic wavelength shifts of a WGM resonance of the microsphere of 105μm in diameter placed in free air and in the working cell at 298K, respectively.

temperature must be increased very slowly and steadily. The thermal response time of the silica microspheres can be estimated using the lumped capacity analysis of heat transfer [52]. We consider the heat transfer of a sphere in natural convection. The Nusselt number can be calculated from the correlation below

$$Nu = 2 + \frac{0.589 Ra_D^{1/4}}{[1 + (0.469/\mathrm{Pr})^{9/16}]^{4/9}} \tag{5.5}$$

For air at 25°C, we have Prandtl number Pr=0.702. Ra_D is linearly proportional to the temperature difference between the sphere and surrounding air. If we assume the temperature difference is ~0.1K, for a sphere with diameter of 400μm, Rayleigh number $Ra_D \approx 6\times10^{-4}$ and thus $Nu\approx$2.07. Even we set the temperature difference ~1K, the $Nu\approx$ 2.12. Thus, due to the facts that the air in the cell is stable, the sphere is small and temperature difference between the sphere and air is small during the slow temperature changing process, we can assume $Nu\approx$2. The convection heat transfer coefficient is

$$h = Nu \cdot k / D \tag{5.6}$$

Using air's thermal conductivity coefficient $k = 0.026W/(m \cdot K)$, we have $h = 130W/K$. The thermal conductivity coefficient of silica is $k_{SiO2} = 1.38W/(m \cdot K)$. Thus, we have Biot number

$$Bi = \frac{hD}{k_{SiO2}} = 0.038 < 0.1 \tag{5.7}$$

Therefore, lumped capacity analysis for sphere is valid. In other words, the sphere's temperature can be assumed to be uniformly changed in the experiment. The time constant of the temperature response of the 400μm sphere is

$$\tau = \frac{\rho c V}{hA} \approx 0.8s \tag{5.8}$$

where silica density $\rho = 2.2 \times 10^3 kg/m^3$ and the specific heat $c = 703J/(kg \cdot K)$. And the smaller the sphere, the shorter the thermal response time. The thermal time constant of a microsphere 80μm in size is only 0.03 s. In actual experiments, the copper plate is heated so that it takes about 3 min to raise the air temperature by 1K. For every 0.5 or 1K temperature increment, 10 WGM spectra are measured in 0.1s and an averaged resonance wavelength shift is calculated. We are confident that the WGM couple and thermocouple are in thermal equilibrium and have a nearly constant and uniform temperature distribution during the samplings.

Now we are ready to investigate the resonance wavelength shift against the temperature rise. The wavelength tuning range for each measurement is measured by an optical spectrum analyzer (AQ6317B, ANDO). A significant WGM resonance that appears in each tuning is selected for measuring the resonance wavelength shift. A WGM spectrum at room temperature is first measured. Then a wavelength shift against a temperature rise is

obtained from the difference between the resonance wavelength at any measured temperature and that at room temperature. Figure 5.6 shows the measured WGM spectra for the microsphere 145μm in diameter at three different temperature stages. The loaded Q value of the microsphere is estimated as 8×10^6 from the dips indicated in the figure.

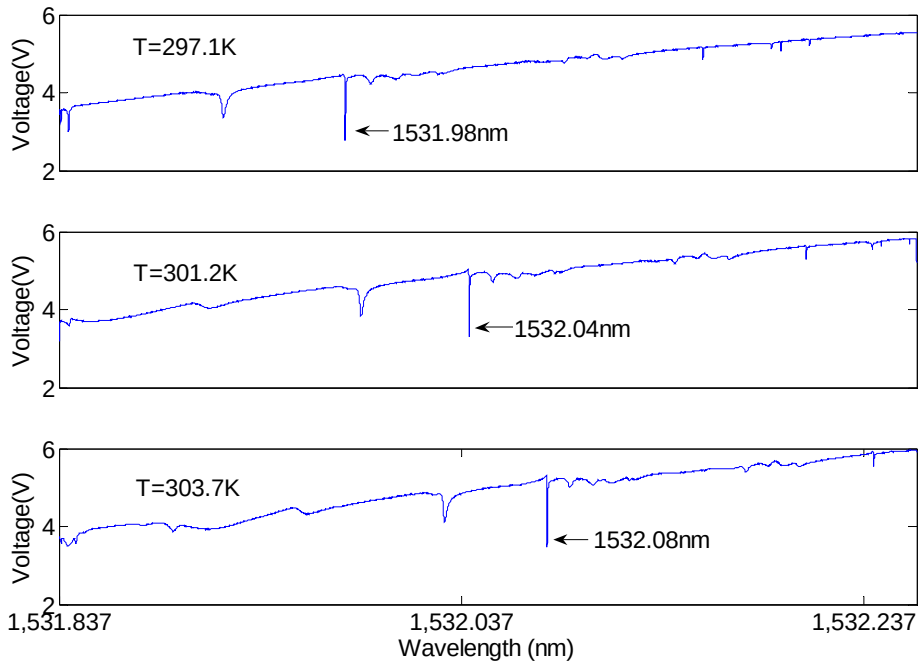

Figure 5.6 The measured transmission spectra of the micro bead of 145μm in diameter (Q=8×10^6) at three different temperature stages.

Microspheres with diameters of 145μm, 225μm, 290μm and 430μm, respectively, are measured for wavelength shifts versus temperature changes in a general temperature range from room temperature to about 7–10K higher and the results are presented in Figure 5.7. The temperature sensitivity (wavelength shift per unit temperature change) for each of the tested microspheres can be best determined by linear fitting of the experimental data. The measured sensitivity results as well as the analytical ones are listed and compared in Table

5.1. Since the magnitude of a shift is much smaller than a resonance wavelength in the testing temperature range, we can use the measured resonance wavelength at a reference temperature (such as room temperature) to calculate the temperature sensitivity for a microsphere operated at a given resonance mode. The analytical temperature sensitivities in Table 5.1 are calculated from equation (5.4) using the resonance wavelengths of the microspheres measured at room temperature and the values of $\alpha = 0.55\times10^{-6}$ K^{-1} [53] and $\beta = 8.52\times10^{-6}$ K^{-1} [54] for bulk silica at a wavelength of around 1531 nm and at a temperature of about 303 K. Although a resonance wavelength depends on the size of a resonator, the variations of the analytical temperature sensitivity (nearly a constant of 13.89 pm K^{-1}) are so small (±0.01 pm K^{-1}) for all the tested microspheres.

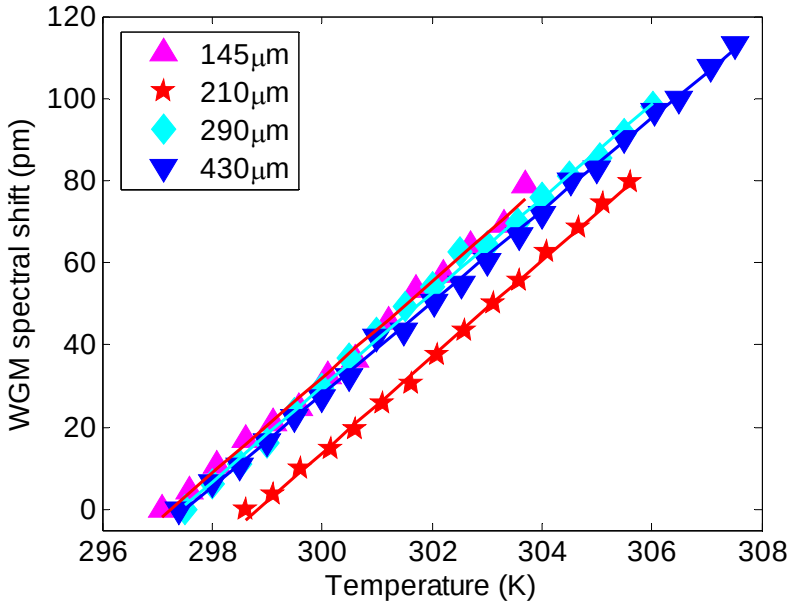

Figure 5.7 The measured data and linear fitting curves of WGM resonance wavelength shifts against temperature variation for the tested microspheres.

Table 5.1 Temperature sensitivities of the tested microspheres.

Micro bead diameter (μm)	Resonance wavelength at room temperature (nm)	Analytical sensitivity (pm/K)	Measured sensitivity (pm/K)	Correlation coefficient (r) in linear fitting
145	1531.978	13.90	11.42±0.51	0.9973
210	1531.954	13.90	11.66±0.30	0.9991
290	1531.113	13.89	11.50±0.33	0.9986
430	1530.335	13.88	11.20±0.18	0.9994

From table 5.1, it is seen that the relevant coefficients in the least-squares linear fittings of the experimentally measured data are all close to 0.999 which indicates an excellent linear dependence of the resonance wavelength shift on the temperature change. The measured sensitivities are all about 81%~84% of the analytical. The 95% confidence intervals are within ±0.51 pm K^{-1}. This is consistent with the fact that theoretically the temperature sensitivity is nearly a constant. These results will be reviewed and compared in a larger temperature test range i.e. the cryogenic to room temperature measurements.

5.4 Cryogenic to room temperature measurements

Still with the first insight and encouragement of Prof.Guo, we started to work on the cryogenic temperature measurements using WGM. Thus, the investigation is extended to a broad temperature range. WGM-based temperature sensors have a potential use for cryogenic studies. There is a need for developing electromagnetic interference-immune high resolution cryogenic temperature sensors. For example, in facilities using massive

superconducting magnets, temperature data need to be recorded to actively control the magnet cool-down and warm-up, and to monitor the cryogenic system during operation. These systems often operate very close to their limits such that a rather small increase in temperature may cause a catastrophic failure. This requires good temperature stability, and therefore, fine resolution in its monitoring [55].

Cryogenic optical fiber sensors (COFS) operating at liquid nitrogen (LN_2) temperature level have been used to measure temperature conditions for superconductors. Lee *et al.* [56] proposed a COFS with resolution ~0.4 K in the vicinity of room temperature and ~0.07 K in the vicinity of cryogenic temperatures using temperature dependent emission characteristics of an erbium-doped fiber (EDF). Bertrand *et al.* [57] realized an optical fiber temperature sensor based on the analysis of the decay time of the fluorescence emitted by special doped crystals bonded at the extremity of a multimode optical fiber, the excited state lifetime of which is greatly dependent on temperature. However, this kind of sensor is not cost-effective, and the resolution is limited by the fluorescence emission intensity and contrast of decay time in cryogenic temperatures. Ciotti *et al*. [56] have studied a photo-imprinted Bragg grating fiber optic cryogenic temperature sensor. On illuminating the fiber with a broadband source of light, a narrow band is reflected by the grating at the Bragg wavelength. The resolution of the sensor of this type depends on two physical properties: the temperature dependence of the glass refractive index and its thermal expansion.

In this study, temperature measurements in a wide range from cryogenic to room temperature using the fiber WGM-based microsensor with an ultra-fine resolution are demonstrated. A thermally insulated optical test cell is designed. Realization of a

cryogenic temperature environment for optical measurements via the use of a LN_2 container is discussed. A means for protection of frost formation on the optical system is introduced. Precise calibration of the laser tuning spectra is achieved by the use of a high resolution optical spectrum analyzer. The WGM resonance spectra are recorded and the wavelength shifts are determined. The relationships of temperature versus wavelength shift are plotted for five microsensors. Finally, the measured temperature sensitivities are compared with the analytical values.

5.4.1 Experimental setup and methods

The experimental setup is sketched in Figure 5.8. The fiber taper is aligned through two narrow slits of the optical test cell. The sensor head microsphere and a temperature-calibration thermocouple (the same one as we used in the near room temperature measurement) are placed into the cell through another two slits of the optical test cell. The microsphere is precisely coupled with the fiber taper. The distributed feedback (DFB) laser (1531 nm) is tuned by a saw shape injection current and coupled into the optical fiber taper. The fiber passes through a polarization controller to optimize a TE mode coupling. The fiber modes couple more strongly to the TE modes than to the TM modes for microspheres [59]. The transmission signal is detected by a photodiode detector (Thorlabs PDA400) and recorded by a computer equipped with a high sampling rate data acquisition (DAQ) card (National Instrument PCI-6132) for acquiring WGM resonance spectra. The thermocouple is positioned about 0.1 mm away from the sensor head microsphere to measure the local air temperature. The signal from the thermocouple is

acquired by a high accuracy DAQ card (National Instrument PCI-6220) in the same computer. Same LabView Programming is used as shown in Figure 5.3.

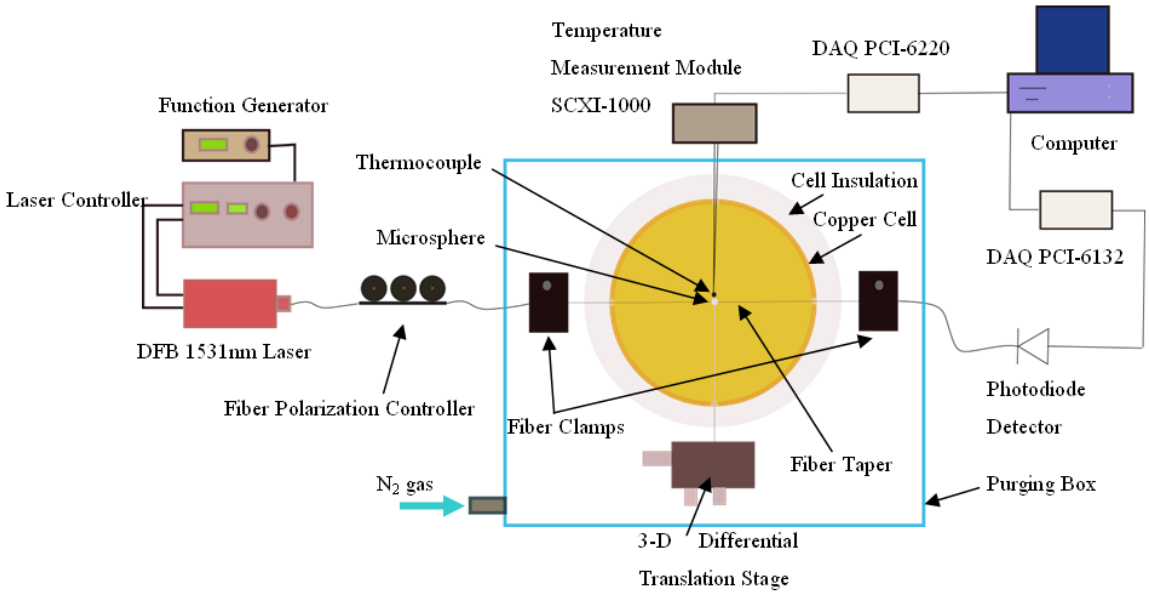

Figure 5.8 Schematic of the WGM sensing setup for cryogenic temperature measurement.

The dimensions and a photo of the optical test cell are shown in Figure 5.9 (a) and (b), respectively. The cell is made of copper for efficient cooling. It is insulated with a layer of fiberglass to maintain cryogenic temperatures. The cell is 31mm in diameter and 21mm high. Four accessible slits with width 1.2mm each are machined on four sides of the cell for placement of the fiber taper, thermocouple and microsphere, respectively. The open top of the cell is covered by a glass slide during experiment. This cover is partially wrapped with fiberglass, leaving a small window in the middle for viewing and optimizing the WGM coupling. The cell is connected on a translation rail for precise placement and alignment with respect to the WGM sensor system. After optimizing the WGM resonances, another glass slide wrapped with fiberglass is tightly attached onto the window with vacuum grease

for further insulation. A solid copper rod is attached to bottom of the cell with silicone paste to ensure good thermal conductivity. An insulated LN_2 container is placed under the

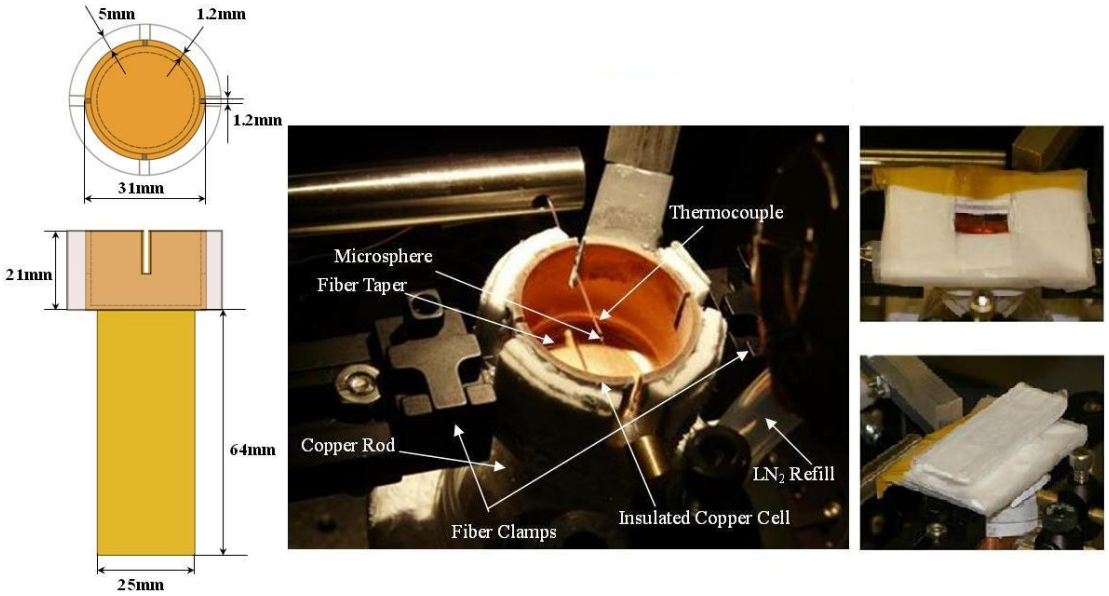

(a) **(b)**

Figure 5.9 Optical test cell: (a) top and side views of the cell with dimensions; (b) a photo of the cell showing structure and alignment.

cell so that the copper rod is fully immersed into the liquid. For initial attempts, the measurement was made in open air as shown in Figure 5.10, which illustrates the alignments of the setup. However, there is always some frost forming on the coupling system that destroys or alters the WGM coupling during the measurement. Thus, a purging box with a volume of $0.03m^3$ is designed and made to cover the whole alignments. As shown in Figure 5.11, after the alignments of WGM coupling is made, the purging box is carefully put on top of the alignments and then all the accesses on it are sealed by sealing tape. A major access is for fine re-adjustment of the coupling after implementing the

purging box. A glass window on top of the box is made for accessing the test cell cover and observing the coupling under microscope if re-adjustment is needed. The LN_2 refill device is insulated with fiberglass and fixed on the box which accurately delivers LN_2 into the container inside the box. Once the coupling is optimized by both the fiber polarization controller from outside and the 3D translation stage inside, the box is purged for 30 min with a nitrogen flow rate 2000cm^3 min^{-1} before injection of LN_2 into the container.

To cool down the air temperature in the cell, LN_2 is filled through the fiberglass-insulated tube into the container. Nitrogen purging continues during the entire experiment period to avoid frost formation on the optical system. The coldest air temperature achievable in the cell depends on the size of the LN_2 container, the LN_2 filling level, and the heat transfer between the cell and the container. The current experimental system can cool down the air temperature in the cell to roughly 100 K. For this study, stable temperatures in the range from 113 K to 293 K were experimentally achieved.

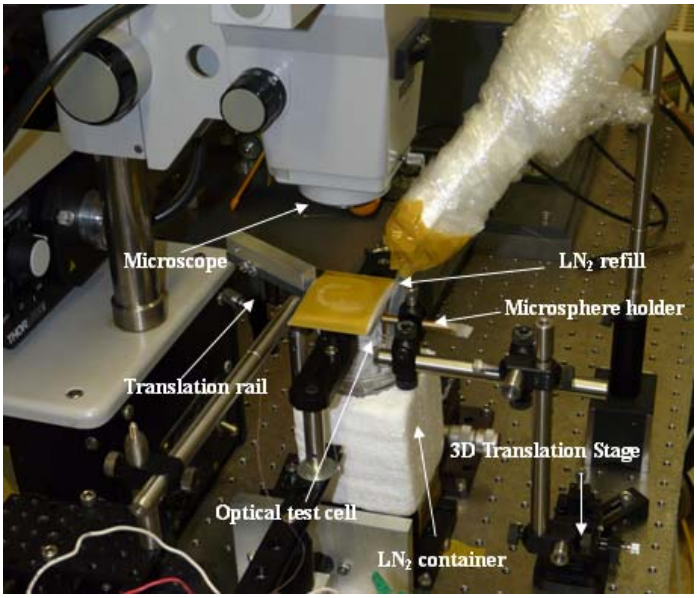

Figure 5.10 Photo of initial attempt of low temperature measurement setup in open air.

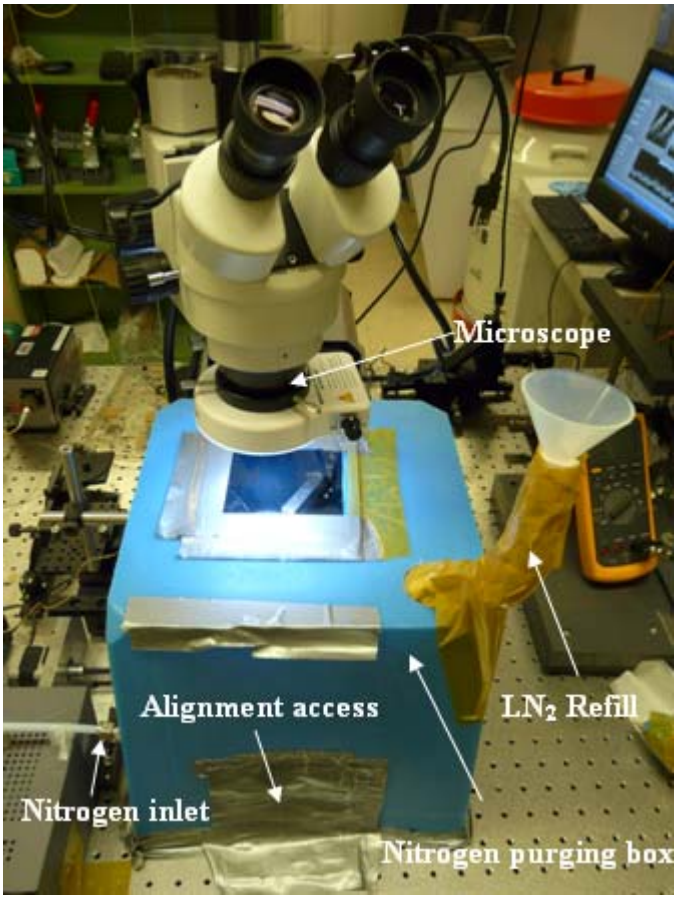

Figure 5.11 Low temperature measurement alignments enclosed in a temperature purging box.

5.4.2 Results and Discussion

Figure 5.12 shows the air temperature changes measured by the thermocouple in several tests with various microspheres placed into the optical test cell. It is seen that in the first few minutes, the air temperature remains at a stable low value and this value varies in different tests because it depends on the filling level of LN_2 in the container. Then the air temperature starts to increase slowly after the LN_2 level drops below the copper rod and steadily due to heat transfer with the external environment. The rate of temperature increase is a function of temperature; thus, it is seen that the spread of response when the temperature starts to increase is different for different tests. When the temperature is over

250 K, the difference of the spreads of temperature response between different tests is negligible. The initial rate of temperature increase is <0.1 K s^{-1}. It takes approximately 4h to heat the cell from cryogenic temperature back to room temperature. The time constants of the microspheres and thermocouple are small enough for them to be able to follow and reflect the air temperature variation in the cell.

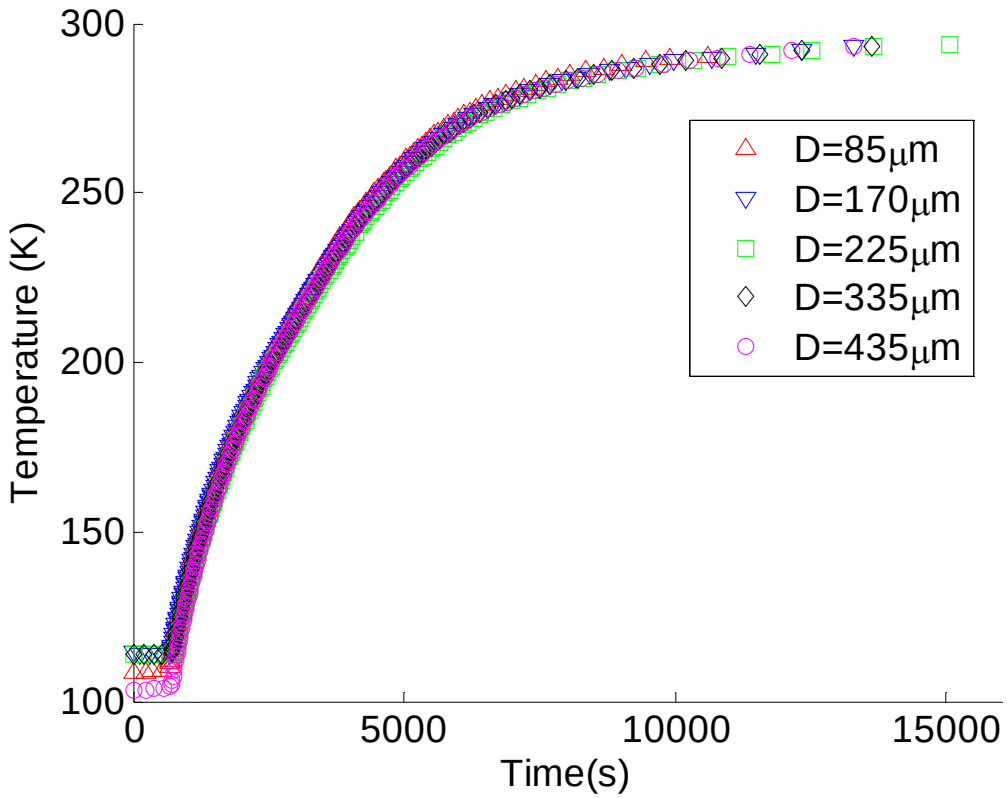

Figure 5.12 The measured air temperature changes in the optical test cell.

For this measurement, the WGM shift is much larger than that of the near room temperature measurement. Thus, the related laser tuning range for accommodating the shift can on longer be assumed to be linear with injection current. Figure 5.13 shows five representative curves of the relationship between the lasing wavelength and the current in the laser diode controller for different controller temperatures. The laser tuning is

calibrated by an optical spectrum analyzer (AQ6317B, ANDO). Repeated testing has shown that the uncertainty is negligible, within ±0.001 nm for each measurement point. The calibrated curves are utilized for accurately finding the resonance peaks in the WGM spectra. In the following temperature tests, the controller temperature T_c is selected such that the base resonance line is located close to the short-wavelength end in the wavelength tuning spectrum.

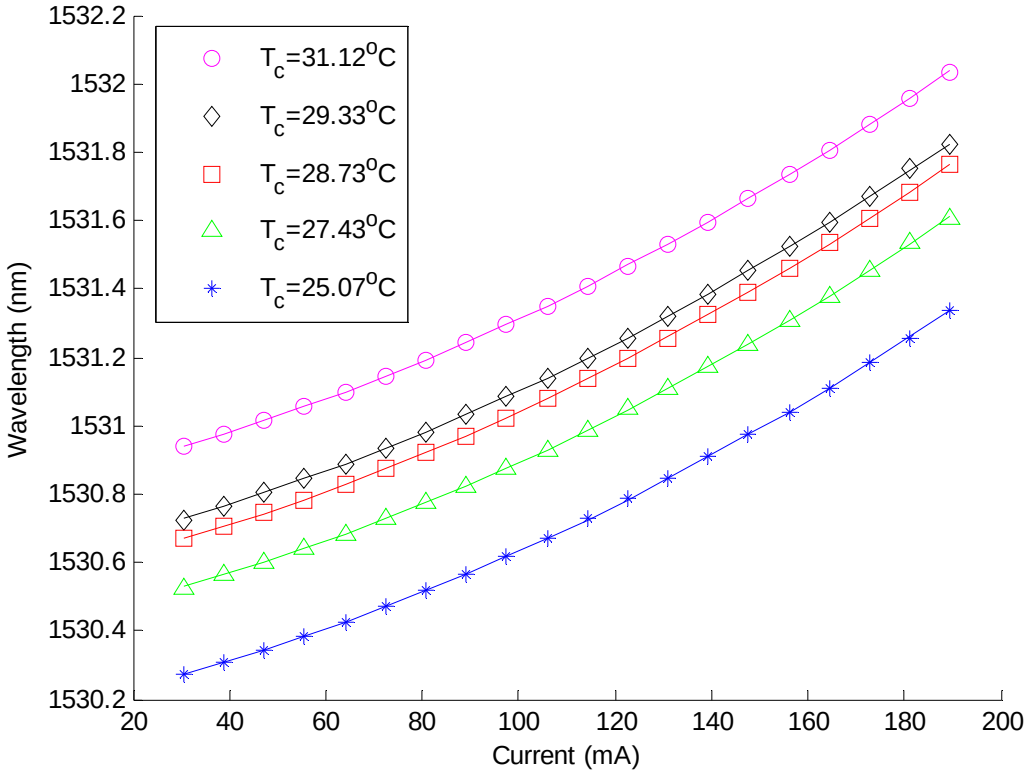

Figure 5.13 Calibration of the DFB 1531nm laser tuning at different controller temperatures.

After optimizing the coupling with the 3D differential translation stage and the polarization controller, a significant TE WGM resonance that appears in each recorded spectrum is selected for measuring the resonance shift with respect to the temperature rise.

Generally, the loaded Q-factor of the selected resonance is about 10^7 in the current study. Figure 5.14 shows the measured WGM spectra from a typical microsphere (225μm) at four different temperatures. It should be noted that the spectra shown have been calibrated with the nonlinear laser tuning. Thus, the modes in Figure 5.14 are linearly distributed in the

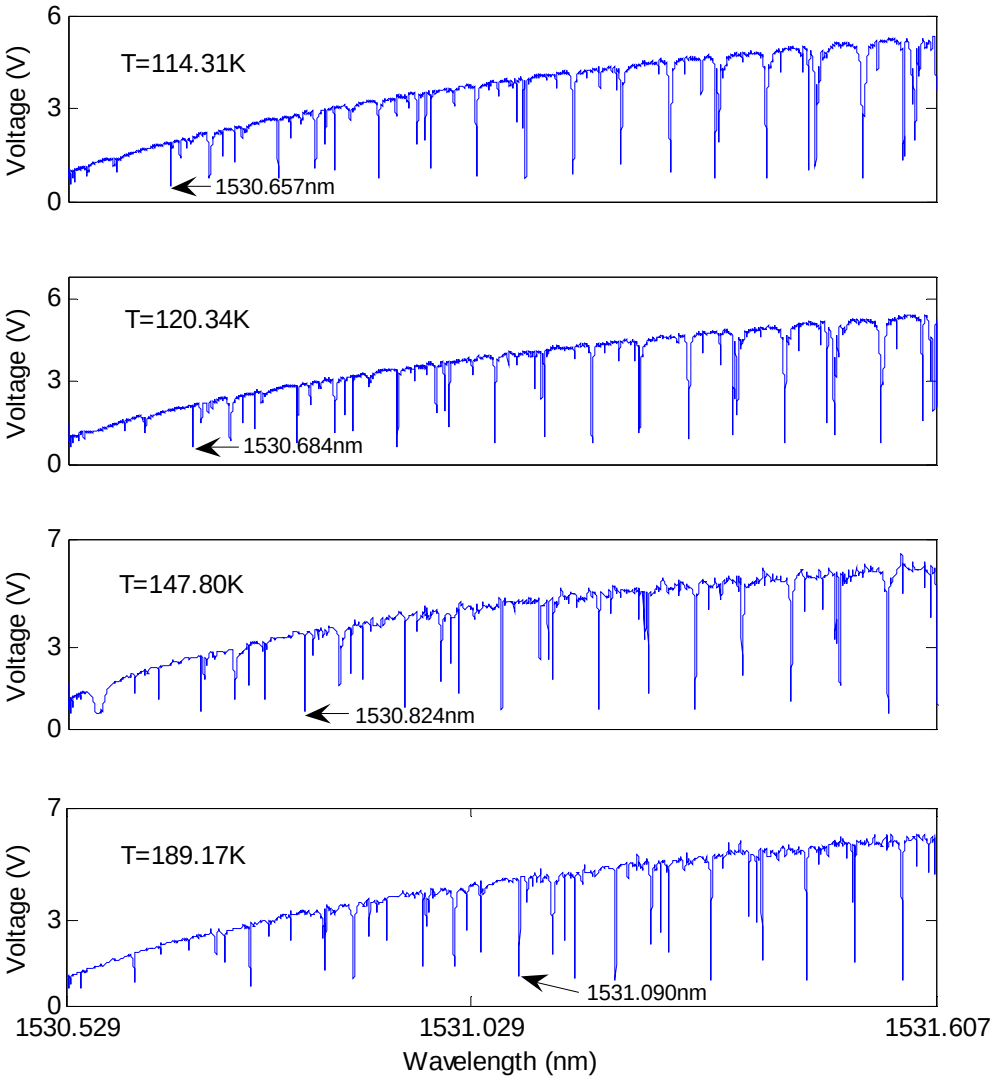

Figure 5.14 Typical transmission spectra of the microsphere 225μm in diameter at four different temperatures.

wavelength abscissa. Microspheres with diameter 85µm, 170µm, 225µm, 335µm and 435µm, respectively, are measured for their wavelength shifts versus temperature change in the range from 113.7±0.6 K to 292 ±1.5 K, and the results are presented in Figure 5.15. The two colors (blue and red in the online version) for each symbol represent shift values measured from two different WGM resonances with continuous temperature variation. This is because the tuning range of the laser is restricted to approximately 1 nm at a fixed controller temperature as shown in Figure 5.13. However, the total optical shift of the

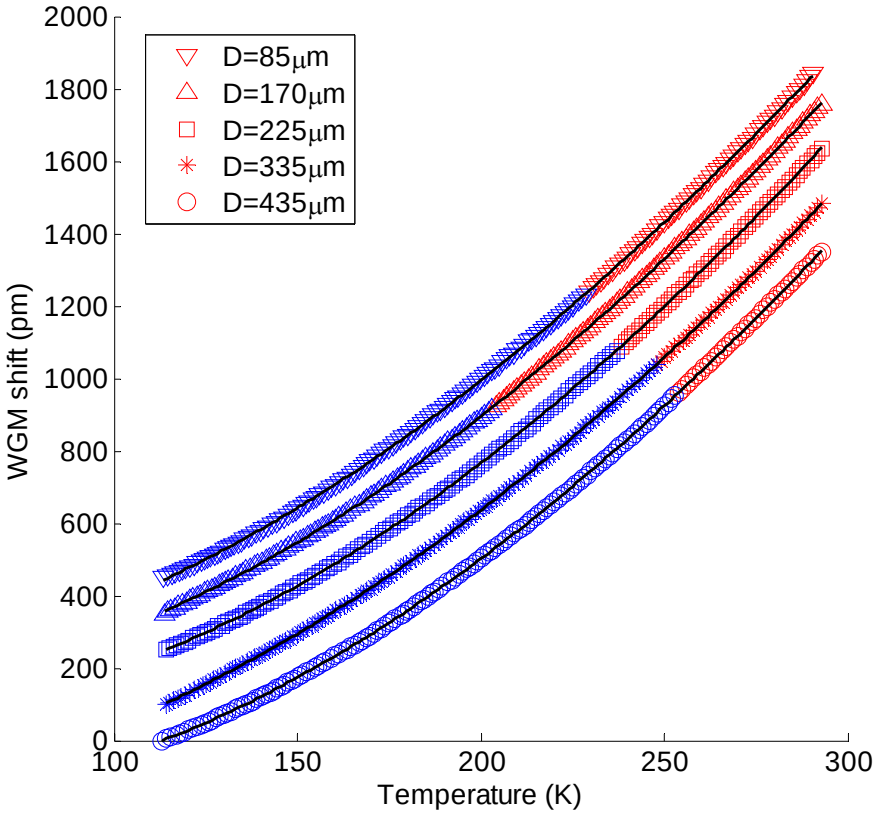

Figure 5.15 The measured data and least-square cubic fitting curves of WGM resonance wavelength shift against temperature variation for five different microspheres. The shifts are raised by 100pm, 250pm, 350pm, and 450pm for microspheres of 335µm, 225µm, 170µm and 85µm in diameter, respectively, for easier visualization.

WGM resonances in the wide temperature range could reach 1.4 nm, beyond this tuning range. It is worth mentioning that although two different WGMs are sampled, the shifts obtained from them overlap smoothly as shown in Figure 5.15. The data can be well fitted by third-order polynomials. The coefficients of correlation for the five fitted curves are all above 0.999, and the 95% confidence intervals in the fittings are very small, usually within ±0.20 pm, corresponding to a temperature uncertainty of 0.02 K, which takes account of the random error of measurement. The random error may be caused by fluctuations of the data acquisition instrument system as well as fluctuations of WGM shift and thermocouple temperature measurements. Potential bias/systematic errors are hard to estimate accurately, which may majorly result from the calibration of the thermocouple and the fact that the microsphere is apart from the thermocouple. The thermocouple is only about 0.1mm from the microsphere and the temperature gradient inside the cell is small, which indicates that bias error from separation of microsphere and thermocouple is negligible. The K type thermocouple calibration error is about 2K, i.e., all the curves in Figure 5.15 may be consistently shifted ±2K from their true positions.

Figure 5.16 plots the measured temperature sensitivities which are the slopes of the fitted curves in Figure 5.15 for the tested microspheres. Error bars are added to the beginning and end of the curves. The related uncertainties are estimated from combing the random errors from curve fittings and the major bias errors (±0.06pm/K) resulted from thermocouple calibration. Although slight differences exist among the various size microspheres, no significant size effect is noted. The temperature sensitivity increases from 4.5 pm K^{-1} to 11 pm K^{-1} with increasing temperature in the test temperature range. It

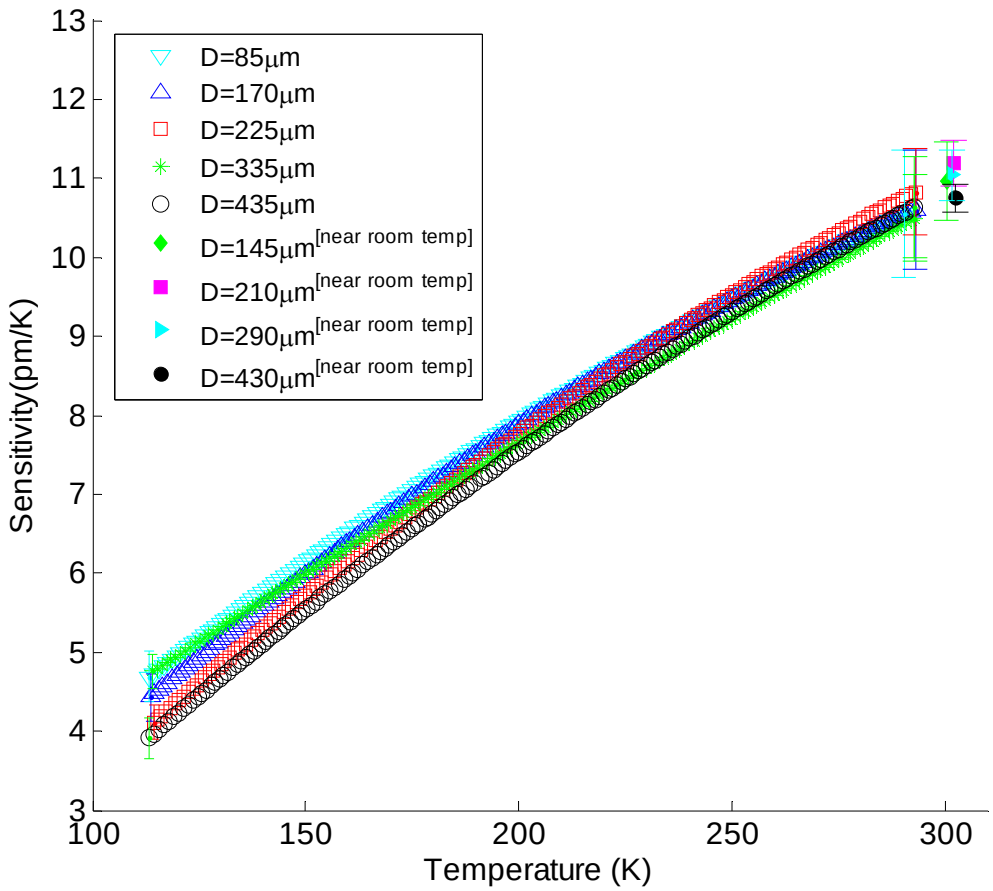

Figure 5.16 The measured temperature sensitivities of the five different microspheres and the sensitivities for the cases in the near room temperature measurements.

was noted that a linear laser tuning curve was assumed in the determination of the WGM shifts in near room temperature measurements. From Figure 5.13, such a linear assumption was appropriate for the much smaller laser tuning range (~0.15nm) in the near room temperature measurements. The values in Table 5.1 are marked in Figure 5.16, and they match with the tendency of the cryogenic measurement curves.

The thermal expansion and thermo-optic coefficients for fused silica from Corning SMF-28 fibers at wavelength 1531 nm are unknown. However, they are available in the

literature for bulk Corning 7980 silica at wavelengths 1500 and 1600 nm [54, 60] as summarized in Figure 5.17. Generally, the thermal optic coefficient of Corning 7980 silica is much larger than the thermal expansion coefficient. Figure 5.18 compares the measured sensitivity averaged from the five test microspheres with the analytical sensitivity calculated from equation (5.4) based on the material properties of bulk Corning 7980 silica. The measured sensitivity can be expressed by a quadratic equation

$$d\lambda / dT = -(4.48 \pm 0.30) \times 10^{-5} T^2 + (5.31 \pm 0.12) \times 10^{-2} T - (1.08 \pm 0.12) \qquad (5.9)$$

The coefficients are obtained from averaging the corresponding coefficients of the five tested cases. The uncertainties in the three coefficients of the equation give 95% confidence intervals, which are estimated by a commercial statistical software SAS using the generalized linear model. The analytical sensitivity curve can also be fitted by a quadratic relationship. Thus, the cubic fittings in Figure 5.15 are reasonable. From Figure 5.18, it is observed that the varying pattern of the experimental sensitivity curve is similar to the analytical one. Error bars are added to the beginning and end of the experimental curve and ratio curve. The related uncertainties are estimated from combing the random errors that indicated in equation (5.9) and the major bias errors resulted from thermocouple calibration (±0.06pm/K). The profile of the ratio of the experimental sensitivity to the analytical sensitivity against the temperature is also plotted in Figure 5.18. It is seen that this ratio profile is nearly linear, varying in a narrow range between 0.79 and 0.80. It may indicate that the effective sum of ($\alpha + \beta$) for the fused silica microspheres made of the Corning SMF-28 fiber is approximately 79–80% of the value for bulk Corning 7980 silica.

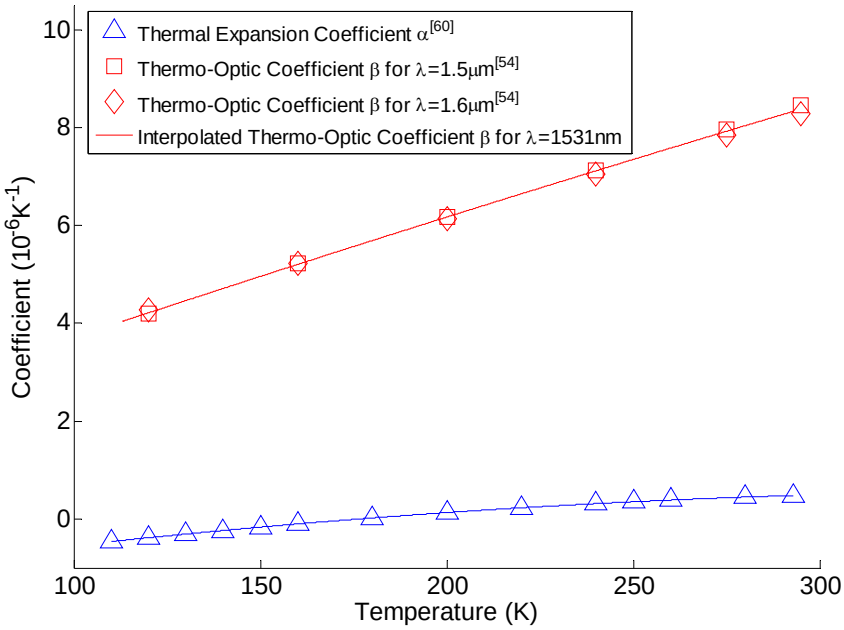

Figure 5.17 The thermo-optic and thermal expansion coefficients for bulk Corning 7980 silica in the tested temperature range [54, 60].

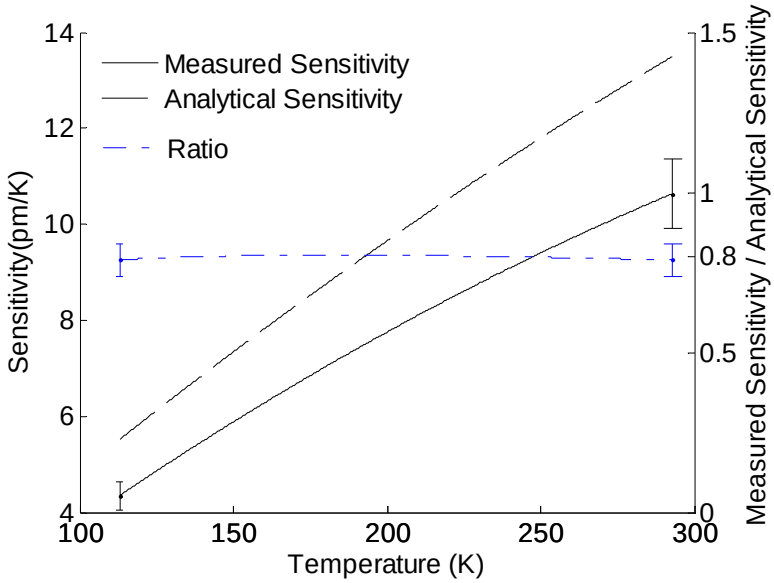

Figure 5.18 Comparison of the measured sensitivity with the analytical sensitivity based on the properties of bulk Corning 7980 silica, and the ratio profile of the measured sensitivity to the analytical value in the test temperature range.

5.5 Merits of the WGM temperature sensor

WGM-based temperature sensors are basically frequency modulated (FM) sensors because the resonance frequency is modulated. A FM sensor is normally more sensitive, or in other words, has much finer measurement resolution than an intensity modulated (IM) sensor such as a thermocouple. Pico Technology did a press announcement in 2000 that TC-08 thermocouple converters boast of 2.5×10^{-2} resolution. Recently, Jha *et al*. [61] achieved a high resolution of approximately 8×10^{-3} K using a complementary metal oxide semiconductor (CMOS) digital temperature sensor. Conventional CMOS devices work over a range of 218K to 398K. Thermocouples are most suitable for measuring over a large temperature range from 0K up to 2073K. The temperature range of a WGM-based sensor depends on the material of the micro-resonator. Silica material still functions below 40K and its softening point is as high as 1665 ^{o}C. The temperature resolution of a WGM sensor is formulated as

$$\Delta T_{\min} = \Delta\lambda_{\min} /(d\lambda / dT) \tag{5.10}$$

in which $\Delta\lambda_{\min}$ is the wavelength resolution of the instrument and $d\lambda / dT$ is the temperature sensitivity of the microsphere. The wavelength resolution is restricted by the linewidth of the scanning laser, the sampling rate in data acquisition, and the loaded WGM resonance *Q*-factor. Suppose the wavelength tuning range of a scanning laser is $\Delta\lambda$ (~0.01–1 nm), the tuning frequency of the laser is f_s (~1–10Hz), and the DAQ card has a sampling rate S, then the minimum tuning wavelength is $\Delta\lambda f_s / S$. Since the sampling rate can go up to dozens of GHz, data sampling is usually not a limiting factor for the wavelength resolution. As for the *Q*-factor, the minimum resolvable resonance shift is about one-hundredth of the resonance linewidth ($\lambda/(100Q)$) [29]. Since the intrinsic

Q-factor of a microsphere resonator is extremely high, the loaded Q can always push to the limit of the laser linewidth. Therefore, Q-factor may not be a limiting factor. In the current instrument, $\Delta\lambda_{\min}$ is limited by the laser linewidth. The current DFB laser has a linewidth of 2 MHz, equivalent to 0.0156 pm. From sensitivity equation (5.4), $d\lambda / dT$ is obtained as 10.82 and 5.877pmK^{-1} for temperature at 300Kand 150 K, respectively. Thus, the minimum resolvable temperature of the current instrument is 1.4 mK and 2.7 mK for temperature at 300 K and 150 K, respectively. No existing cryogenic temperature measurement devices exhibit such a high resolution. The optical fiber temperature sensor usually has a resolution of 0.3 K in the temperature range of 20–120 K [57]. Ciotti *et al.* [56] claimed a temperature measurement resolution of 0.02K. However, its sensor response time is slow, on the order of 1s. The WGM sensor has a quick response. For instance, the time constant of a silica microsphere 80μm in diameter is only 0.03s. As an optical fiber sensor, the WGM sensor can be certainly applied to a cryogenic temperature range on the order of 10 K, although the current infrastructure cannot realize such a low temperature. At 50 K, the sensor sensitivity analytically evaluated from the values of thermal expansion and optical coefficients [54, 60] is 1.301 pm K^{-1}, giving a temperature resolution of 0.012K. The state-of-the-art laser technology has pushed the laser linewidth to a few kHz, i.e., almost three orders of magnitude reduction as compared with the DFB laser used in the current instrument. In such a case, it is possible to reduce the WGM sensor temperature resolution by three orders of magnitude, i.e. to the level of 10^{-6} K. This amazing high resolution is also claimed by Jet Propulsion Lab (JPL) at National Aeronautics and Space Administration (NASA) by studying the WGM temperature sensor [62], however, after our first publication [63] on this subject.

In addition to ultra-high resolution, WGM micro-sensors have other promising application potentials. For example, on-chip temperature monitoring is currently a challenging task [64] because a chip may be easily overheated to function incorrectly or sustain fatal damage without proper temperature monitoring and thermal solution. Nevertheless, integrating common types of sensors (such as thermodiodes, thermistors or thermocouples) into a chip is technically difficult. However, WGM sensors can be easily fabricated and integrated into other electro-optical systems using existing microelectronics techniques [65]; furthermore, the thermo-optic effect can be dominant as in the silica resonators ($\beta >> \alpha$) and this will minimize the mechanical stress induced to the chip by thermal expansion. Recent developments in micro-fluidics and lab-on-a-chip devices have also raised the challenge of whole-chip (liquid and substrate) temperature measurement [66]. Traditional embedded thermocouples have been used for micro-fluidics applications. However, measurements are limited to single locations unless complex fabrication and data acquisition are implemented for multiple thermocouples [67, 68]. It is possible that arrays of WGM sensors can be fabricated on a chip and coupled with just one waveguide to monitor temperature at different locations.

CHAPTER 6

INSTABILITY CHARACTERIZATION OF WHISPERGING GALLERY MODE IN VACUUM

6.1 Introduction

The extreme high resolution of WGM sensor is always claimed according to sensitivity and resonance linewidth (or *Q*-factor) in literature. Few prior studies have been done to characterize the WGM spectral shift noise level for a specific system (laser quality, WGM coupling, etc.). In this chapter, some attempts are carried out to calibrate the resonance spectral shift noise level of the fiber taper-micropshere based WGM coupling system using our DFB1531nm laser. A vacuum chamber is designed and fabricated to enclose the whole coupling system. A fiber ring resonator (FRR) [69] is implemented in the system as a Fabry-Prot interferometer to reconstruct the WGM spectra for eliminating the non-linear tuning and wavelength drifting effects of the laser. Simultaneous and continuous time trace of the WGM spectra under vacuum and interferences spectra of FRR are recorded. Continuous variations in WGM resonance characteristics, i.e., resonance wavelength shift, *Q*-factor and coupling coefficient are extracted out using MATLAB programming. Resonator self-heating effect is also observed by varying the laser power in vacuum.

6.2 Design and fabrication of the vacuum chamber

To study the instability of WGM resulting from the coupling system itself, eliminating the external disturbance such as convection heat transfer and air current flowing around the

coupling system is necessary. A vacuum chamber for this purpose is designed and fabricated.

6.2.1 Design of the vacuum chamber

The design and dimensions of the vacuum chamber for enclosing the WGM coupling system are shown in Figure 6.1. The chamber has a transparent top for viewing the inside coupling. On two side walls of the chamber, there are different types of national pipe thread tapered thread (NPT) feedthroughs including electrical feedthrough for controlling the 3D differential translation stage inside the chamber, fiber input and output feethroughs, gas-in and gas-out feedthroughs (for gas detection study later on), pressure gage feedthrough, vacuum pumping feedthrough, thermocouple feedthrough, and an optional feedthrough (for gas detection study later on). The chamber sits on a base and is fixed by 16 screws. A square O-ring slot with rounded angles is made in the base so that a matched O-ring can be placed between the chamber and the base.

6.2.2 Fabrication of the vacuum chamber

The chamber is fabricated from raw materials. The body and base of the chamber are made of gray chemical-resistant PVC (McMaster) sheets. They are accurately machined and polished for required dimensions using milling machine. The four side walls are accurately aligned and glued together by PVC welding (E-Z WELD). The top is made of heat-resistant borosilicate glass (McMaster) and is attached to the four chamber walls using clear RTV adhesive sealant (#732 multipurpose, DOW CORNING). The 16 holes on

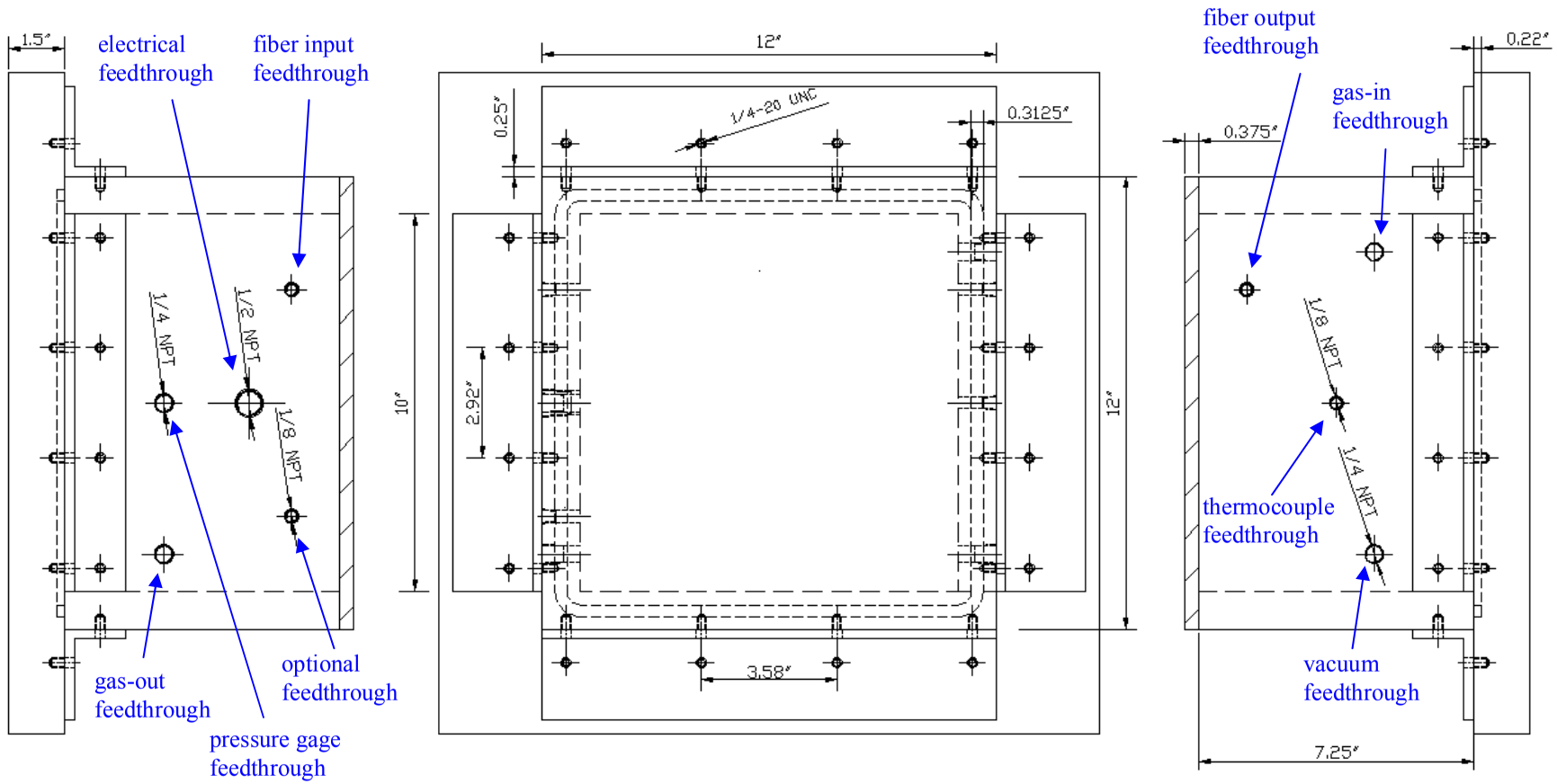

Figure 6.1 Design and dimensions of the vacuum chamber.

the chamber and 16 threaded holes (1/4”-20 UNC) on the base for tightening are well aligned with transfer screws. The O-ring slot in the base is done by milling machine with a rotary holder for its rounded angles. Two ends of a 5/16” silicone O-ring (McMaster) is joined by super glue. The O-ring is then tightly placed into the O-ring slot. High vacuum synthetic grease (DOW CORNING) is applied on the O-ring for further sealing. Stainless steel NPT tubing swageloks (RS Crum) and valves are fed into the through-NPT thread machined on the walls. A high accuracy pressure transducer (Omega Engineering) is fed into the chamber and the signal is monitored by a multimeter. For the vacuum fiber feedthrough, the technique developed by Abraham et al. [70] is adopted to ensure a high vacuum seal around the optical fiber as it traverses though the vacuum chamber wall. Basically, a 1/8” NPT Swagelok is modified by replacing the steel spacer with a Teflon spacer machined by a lathe. A 0.0135” hole is drilled to allow the fiber to go through. The fiber is squeezed and very well sealed when the Swagelok connector is tightened. The electrical feedthrough is also homemade. A cap with six 2mm holes is designed using ProE as shown in Figure 6.2 and the design is then input into a fused deposition modeling machine (FDM3000, Stratasys Inc.) for fabrication. The cap is then inserted into a through drilled 1/2” NPT plug. Six copper wires (for controlling XYZ of the 3D translation stage) with insulation coating are held through the holes of the cap and a type of epoxy (ES1001, Hysol) is filled in the plug for sealing. The photo of the finished chamber is shown in Figure 6.3. The vacuum level can reach <0.03torr using a compact electric extreme-vacuum pump (DV-85N, JB Industries).

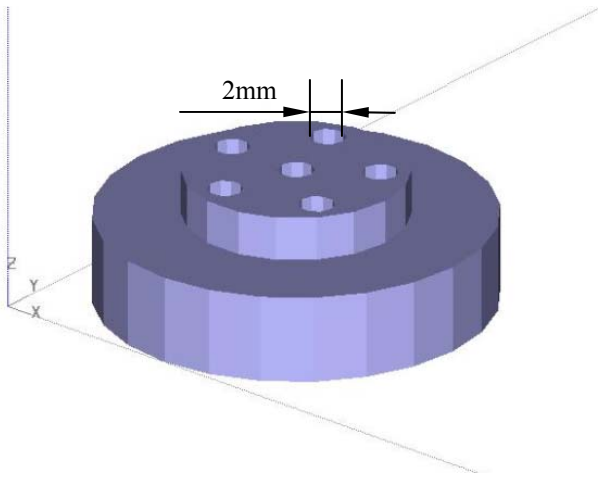

Figure 6.2 The ProE design of the electrical feedthrough cap.

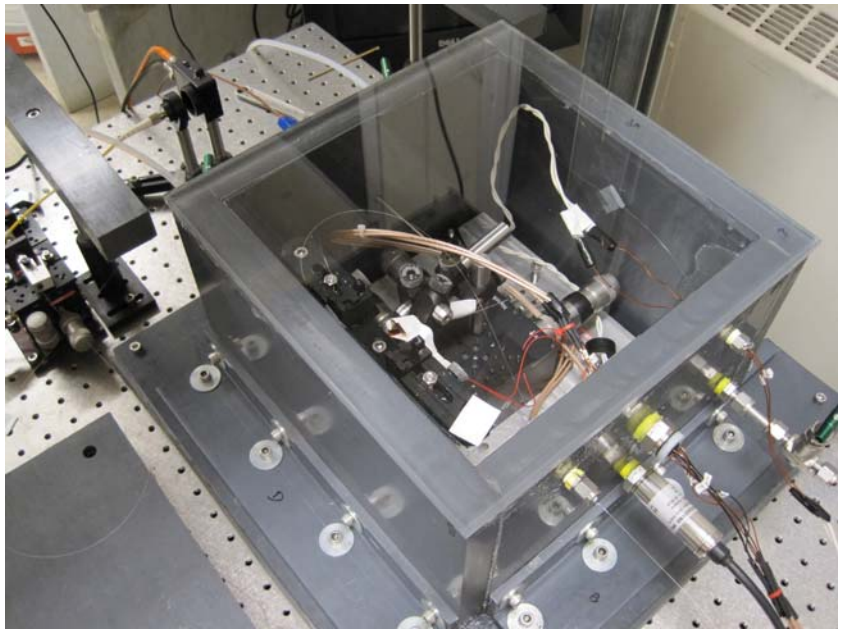

Figure 6.3 Photo of the vacuum chamber.

Since the WGM coupling is made inside the chamber, a special fiber taper fixture is made so that the fiber taper can be removed from the fabrication stage. As shown in Figure 6.4, the two fiber clamps are fixed on two rail carriers. After the fiber taper fabrication, a rail can be put through these two carriers and fixed onto them so that the two clamps holding the fiber can be detached from the pulling device. Another issue is that the base is

deformed a little bit due to the pressure difference between inside and outside of the chamber during vacuum pumping which spoils the coupling. This problem is solved by using an extra alumina breadboard on the base inside the chamber for optical alignments.

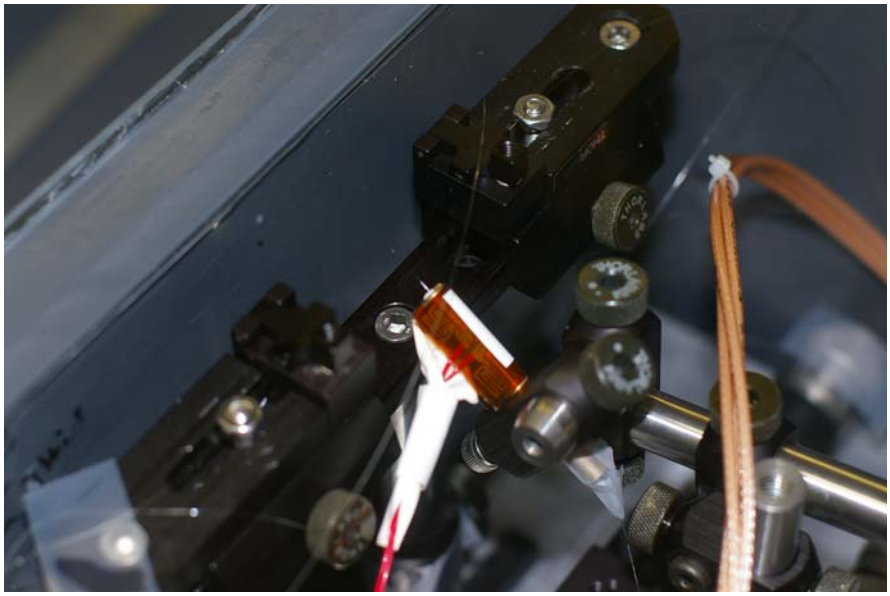

Figure 6.4 Coupling inside the chamber showing the removable fixture of fiber taper.

6.3 Setup for WGM instability characterization

In addition to a vacuum environment, the tiny laser drifting & tuning variation properties have to be tracked simultaneously with a WGM resonance. A fiber ring resonator (FRR), essentially a Fabry-Perot interferometer, is applied for this purpose. The FRR is made simply by connecting two fiber ends of a 2×2, 50/50 broadband fiber coupler (Newport). As shown in Figure 6.5, the WGM coupling is made in vacuum and can be adjusted by a 3D-translation stage (20nm step resolution) controlled by a stage controller (MDT 693A, Thorlabs) outside the chamber through the electrical feedthrough. A fiber based electro-optic modulator (EOM, X5 JDSU) is inserted right after the laser source

(DFB 1531nm) to adjust the light intensity by its DC modulation. The light is then split half by half into two paths using a fiber splitter (Newport). For the path to the WGM coupling, the laser goes through a fiber isolator to minimize the etalon noise and then goes through a polarization controller which adjusts the coupling non-intrusively from outside. The fiber is then fed through the vacuum chamber for the coupling inside the chamber. The other path of the laser goes through the FRR. The interference spectrum of the FRR and WGM spectrum are detected and acquired simultaneously. Therefore, every recorded WGM spectrum can be corrected and reconstructed using the corresponding Fabry-Perot interferences from FRR.

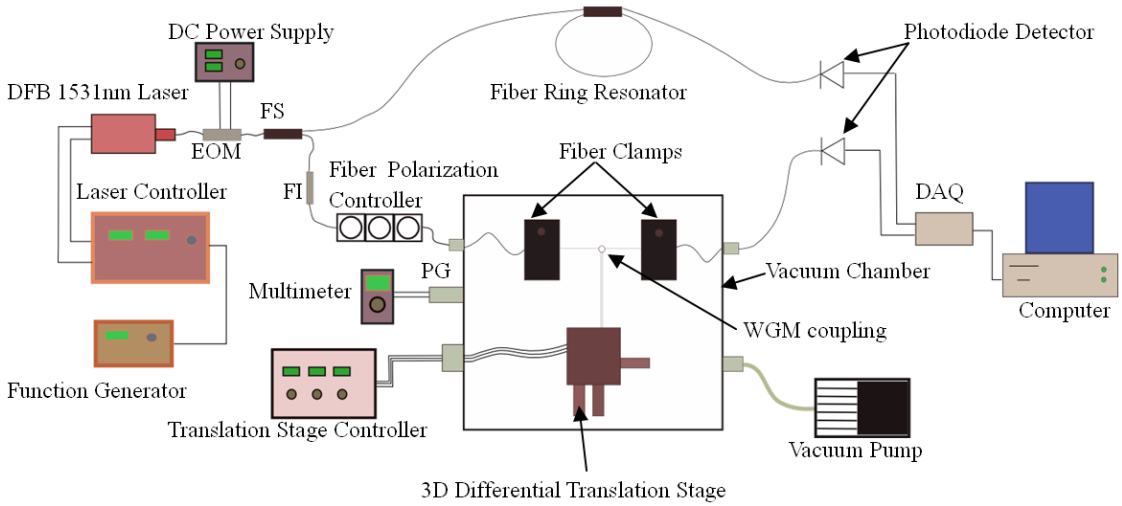

Figure 6.5 Schematic of the WGM instability characterization setup. EOM, electro-optic modulator; FS, fiber splitter; PG, pressure gage; FI, fiber isolator.

6.4 Laser tuning property test

The interferences of FRR serve as wavelength references. All the interference peaks are assumed to be equally spaced in wavelength in the short laser tuning range (15pm). The

fiber ring of the FRR should be appropriate wired and positioned so that only the clear fundamental interference modes appear. Figure 6.6 shows a typical spectrum of optimized interferences. Sixteen peaks appear in the scan and the finesse is approximately 7. The laser wavelength is first assumed to be perfectly linear and stable with injection current and then the shifts of the interference peaks are used to give an idea of the laser tuning linearity and stability. The sixteen interferences are traced continuously at a frequency of 50Hz in 40s (2000 tuning periods), then spectral shift is extracted out for every interference peak using MATLAB programming. As shown in Figure 6.7, the interference peaks shift within 1pm based on the perfect laser tuning assumption. However, as the interference peaks are treated as wavelength-fixed references, the observation proves that the laser tuning is not perfect but with small drifting and random non-linearity. To better illustrate the non-linearity of the laser tuning, assuming the spectral positions of interferences are equally spaced and constants, the tuned wavelength variations referred by the interferences resulting from injection current tunings of the laser at different times (t=8s, 16s, 24s, 32s and 40s, respectively) are shown in Figure 6.8. The five curves intersect with each other and have small deviations from perfect linearity. This test illustrates the need for tracking the laser tuning property using FRR simultaneously with WGM spectra to extract out the tiny spectral shift noise of WGM in vacuum.

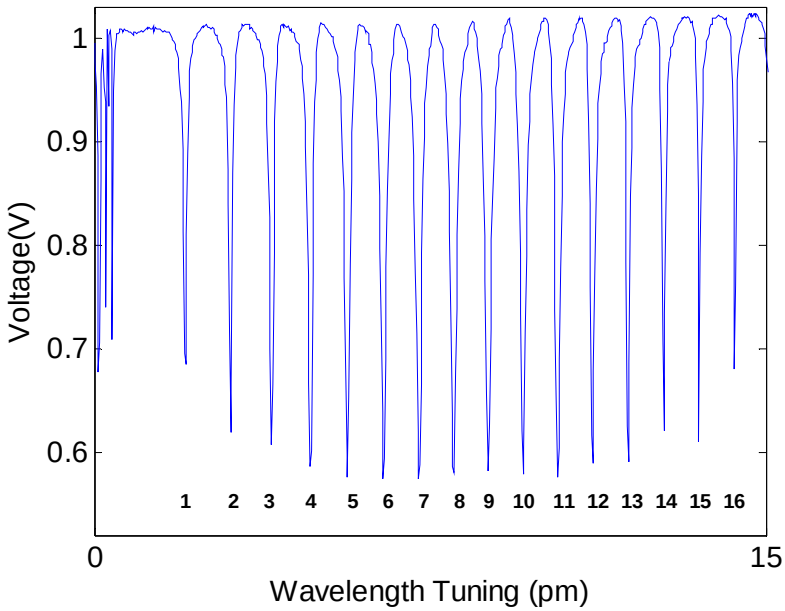

Figure 6.6 A typical optimized spectrum of the interference peaks of the fiber ring resonator in a wavelength tuning of 15pm.

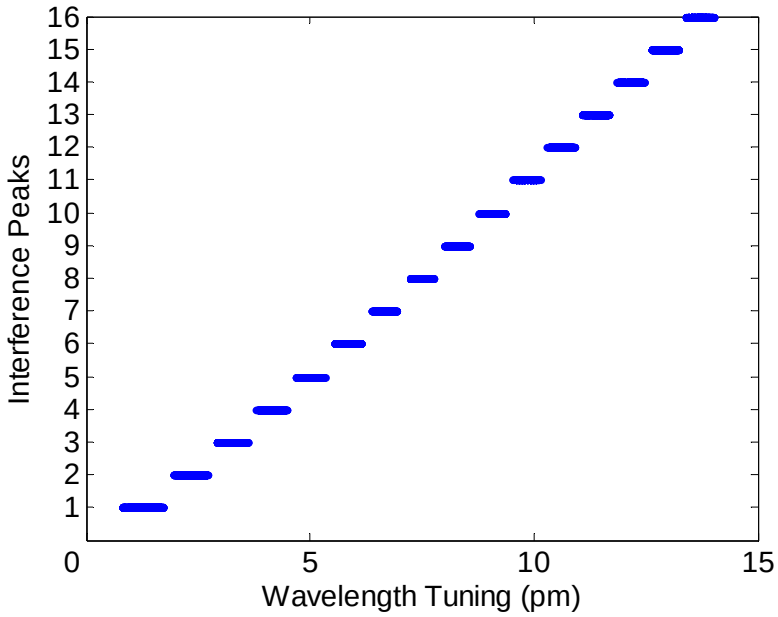

Figure 6.7 Positions of the interference peaks in 2000 tuning periods in 40s.

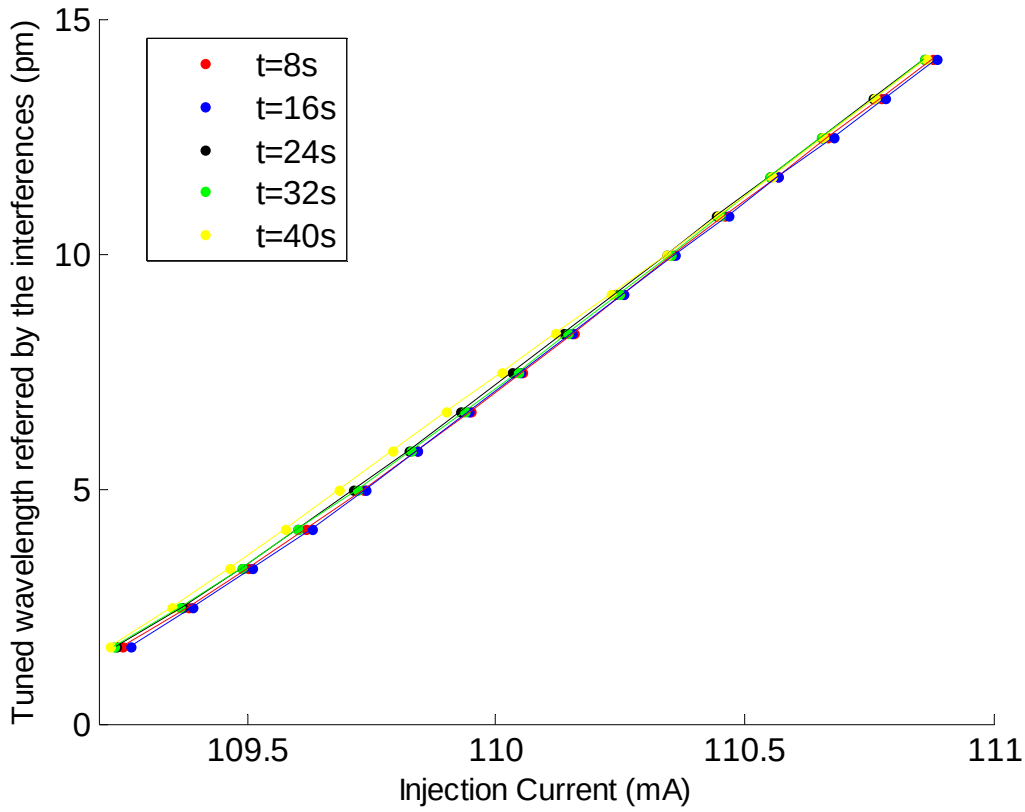

Figure 6.8 The tuned wavelength referred by the interferences resulting from injection current tunings of the laser at different times (t=8s, 16s, 24s, 32s and 40s, respectively).

6.5 Observation of WGM spectral shift by laser heating

The vacuum environment provides the chance of demonstrating the effect of laser heating the microsphere by varying the laser intensity. The Mach-Zehnder electro-optic modulator is applied for continuously attenuating the laser intensity. The wavelength is tuned at a frequency of 100Hz and a microsphere with a diameter of 410μm is used. As shown in Figure 6.9, with a loaded *Q*-factor of approximately 10^7, a blue shift of 2.3pm results from attenuating the initial laser intensity (5mW) by 20dB. The attenuated signal is

amplified in the figure for the ease of comparison. This shift corresponds to a temperature change approximately 0.2K according to the temperature measurement study.

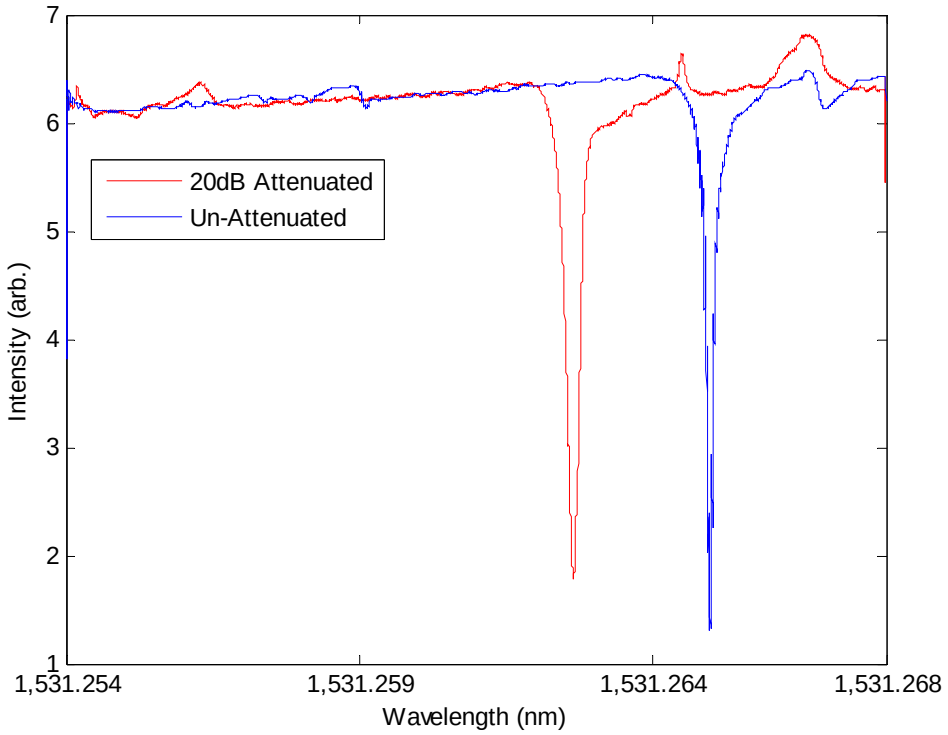

Figure 6.9 WGM spectral shift induced by attenuating the laser intensity.

6.6 Results and discussion of WGM instability characterization in vacuum

A WGM coupling is made in vacuum (<0.03torr) as shown in Figure 6.5. The diameter of the microsphere is 335μm. No voltage is applied on the electro-optic modulator which means that the laser is not attenuated and the input power for the WGM coupling is approximately 5mW. The spectra of WGM and FRR interferences are acquired simultaneously in a tuning range of 15pm so that a single WGM dip appears as shown in Figure 6.10. It is still assumed that the wavelength tuning is perfectly linear with injection current to plot Figure 6.10. The hardwares of our computer (Dell Dimension 3000,

2.80GHz CPU, 2GB memory) and DAQ card (PCI-6132, National Instrument) allow us to record both WGM and FRR spectra up to 40s at a data acquisition rate of 31250Hz. The laser is tuned at a frequency of 50Hz, so that there is 625 data points describing each scan. This gives enough resolution for WGM instability characterization according to our tests.

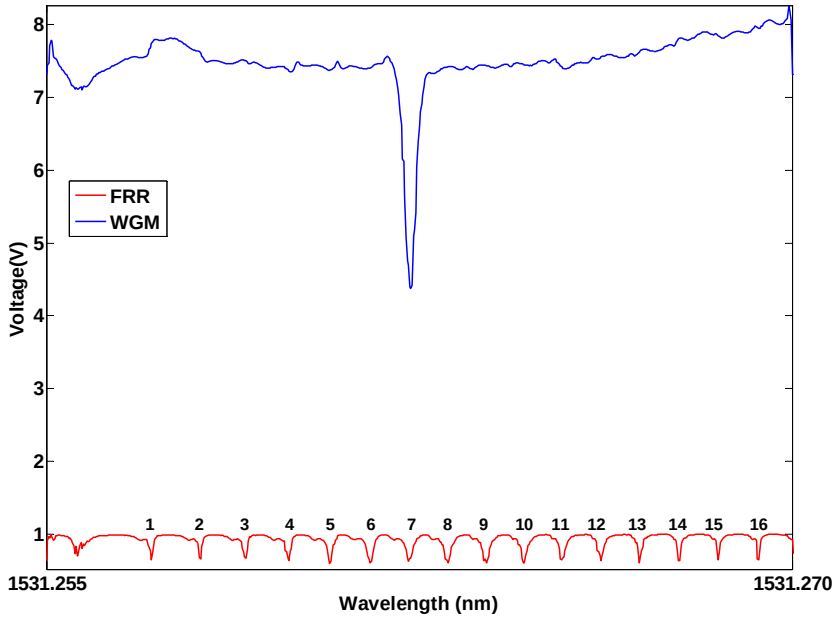

Figure 6.10 Spectra of a 15pm scan of WGM resonance and FRR interferences.

Based on the perfect laser tuning assumption, the WGM spectral shift is extracted out as shown in Figure 6.11. As can be seen, except the digitization noise which results from limited DAQ rate, there are two types of fluctuations: relatively high frequency fluctuation (~1Hz) and a major fluctuation of lower frequency and larger amplitude (~0.1pm). To better interpret these fluctuations, we extract out the spectral shifts of the simultaneously traced of FRR interferences and present a selection of them with the WGM spectral shift as shown in Figure 6.12. For the ease of comparison, a 5th-order Butterworth lowpass filter is applied to remove the digitization noise. It is clearly seen that the same relatively high

frequency fluctuations also exist in the spectral shifts of FRR as that in the WGM spectral shift, which proves that these fluctuations result from the laser drifting, i.e., the starting wavelength of every tuning is not exactly the same. Another significant fact in Figure 6.12 is that the shifts of FRR interferences do not overlap with each other. It reveals the tiny randomness and nonlinearity of the small range tuning (15pm) of the laser. Therefore, we can use FRR interferences as wavelength references to remove all these defects for reconstruction of WGM spectra.

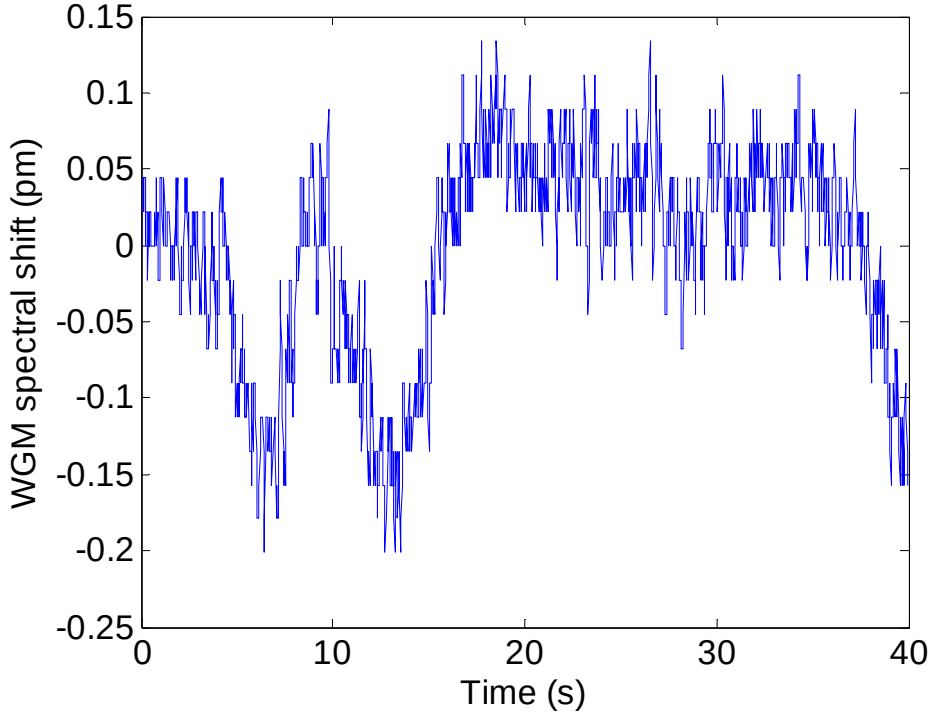

Figure 6.11 WGM spectral shift in vacuum based on perfect laser tuning assumption.

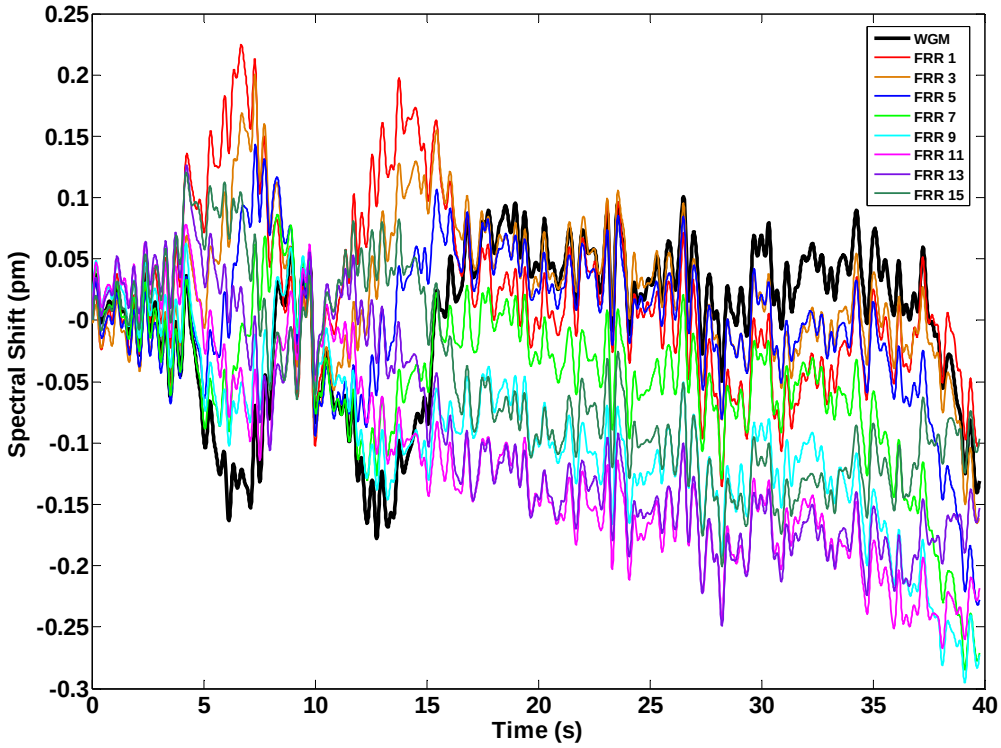

Figure 6.12 Simultaneous trace of WGM spectral shift and FRR interferences shifts in vacuum. Shifts for only half of the interferences (numbers labeled refers to the ones in Figure 6.9) are presented and digitization noise is removed using a 5th-order Butterworth lowpass filter for the ease of comparison.

To better illustrate the similarity or match of the local relatively high frequency variations among the spectral shifts in Figure 6.12, the power spectrums of the spectral shifts for both WGM and interferences are calculated using discrete fast fourier transform (FFT) as shown in Figure 6.13. It can be clearly seen that the relatively high frequency components of the spectral shifts in 1Hz~3.5Hz match well with each other.

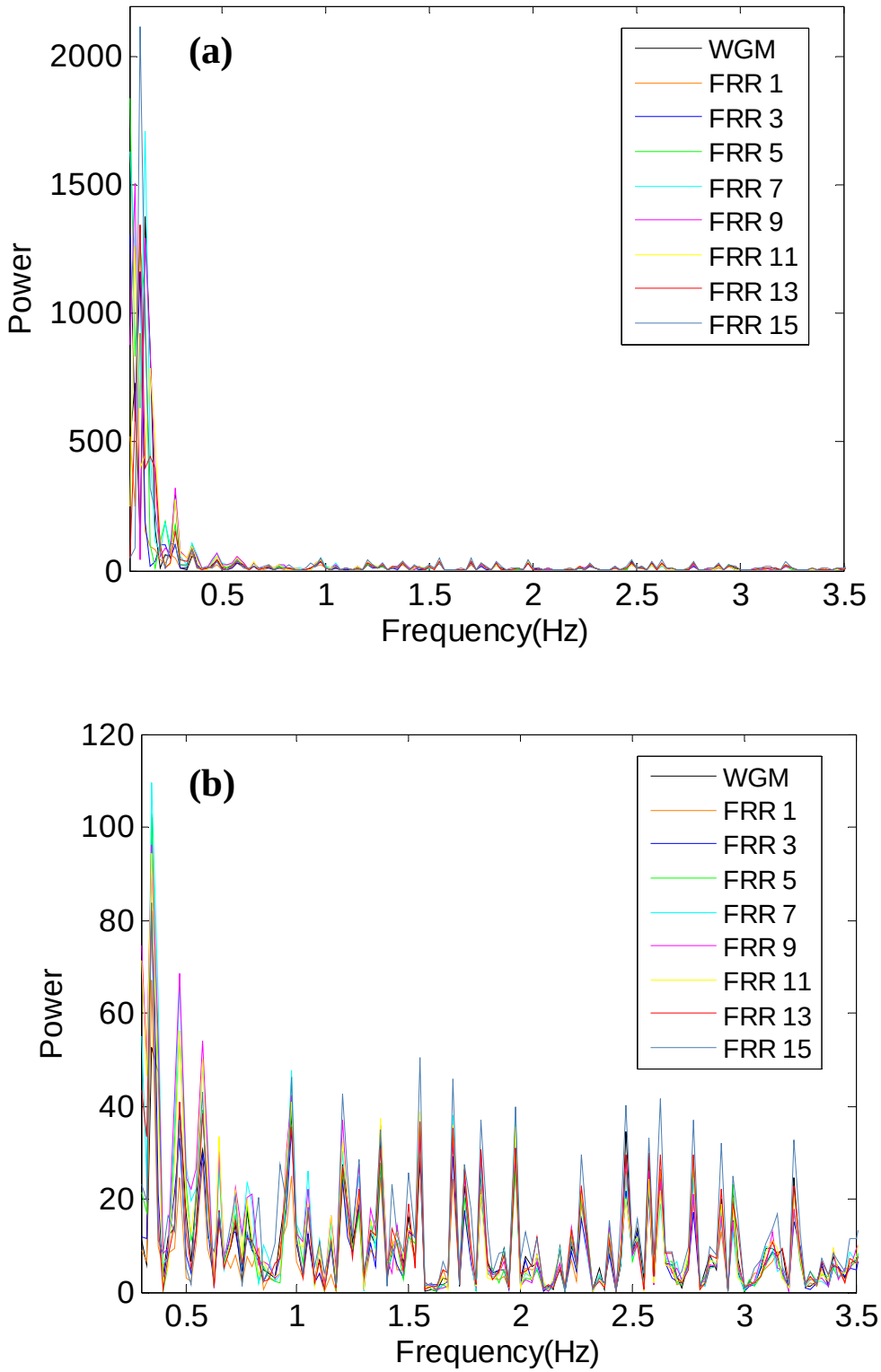

Figure 6.13 Power spectrums for the spectral shifts of both the WGM and interferences shown in Figure 6.12. (a) for a frequency range of 0~3.5Hz, (b) a zoom in for 0.3~3.5Hz.

Using the sixteen interferences as wavelength references and MATLAB programming, every scan of WGM spectrum is reconstructed and the spectral shift is extracted out as shown in Figure 6.14. It is clearly seen that all the relatively high frequency fluctuations result from laser drifting are removed. We have only the digitization noise and larger time scale fluctuation left. In one period of laser tuning, 625 points are acquired, which results in a spectral spacing of 0.024pm between two adjacent data points. The amplitude of the digitization noise indicated in Figure 6.14 is also approximately 0.024pm, which illustrates that the digitization noise comes from the limited DAQ rate. And the larger time scale fluctuation profile is significantly different from the one shown in Figure 6.11, although the amplitude and frequency is similar. Now, we may consider the spectral shift in Figure 6.14 as a result of instability of the WGM coupling system itself. Furthermore, as shown in Figure 6.15, we also extracted out the loaded *Q*-factor based on resonance linewidth measurement (as described in chapter 2) and coupling coefficient using the reconstructed WGM spectra. The digitization noise in coupling coefficient and *Q*-factor are more significant when *Q*-factor is higher, which again confirms that it results from less acquired data points across thinner WGM resonance profile. It can be observed that the coupling coefficient and *Q*-factor fluctuate inversely with each other. From equation (3.11), we can obtain the relation between coupling coefficient and *Q*-factors as

$$M = 1 - T = \frac{4Q_{in} / Q_{coup}}{(Q_{in} / Q_{coup} + 1)^2} \tag{6.1}$$

where M is the coupling coefficient. In the case that the system is in the under-coupling regime i.e. $Q_{in} / Q_{coup} < 1$, M increases as Q_{coup} decreases which indicates the total loaded *Q*-factor should change inversely with coupling coefficient. Thus, the fluctuations of

Q-factor and coupling coefficient presented in Figure 6.15 most likely result from coupling instability. By plotting *Q*-factor together with the WGM spectral shift as shown in Figure 6.16, we also observe that the shift profile follows the *Q*-factor profile (and thus to the

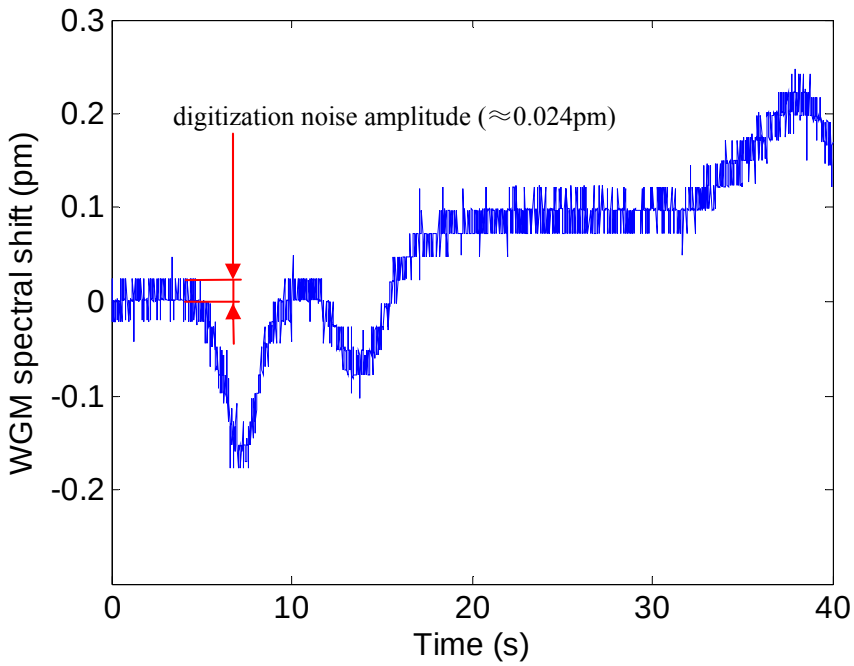

Figure 6.14 WGM spectral shift in 40s for WGM in vacuum based on reconstructed spectrum using FRR interferences with a laser input power of 5mW.

coupling coefficient profile) in the 40s trace to some extent, although there is a time gap approximately 2s. This confirms that the WGM spectral noise is due to the coupling instability instead of any periodical laser heating effect. In addition, since the laser is tuned at a frequency of 50Hz, the much lower frequency and the randomness of the shift noise also illustrates that the shift is a not a result of laser heating. To further confirm this, we attenuate the power of the laser by approximately 20dB (to 0.05mW). Following the same

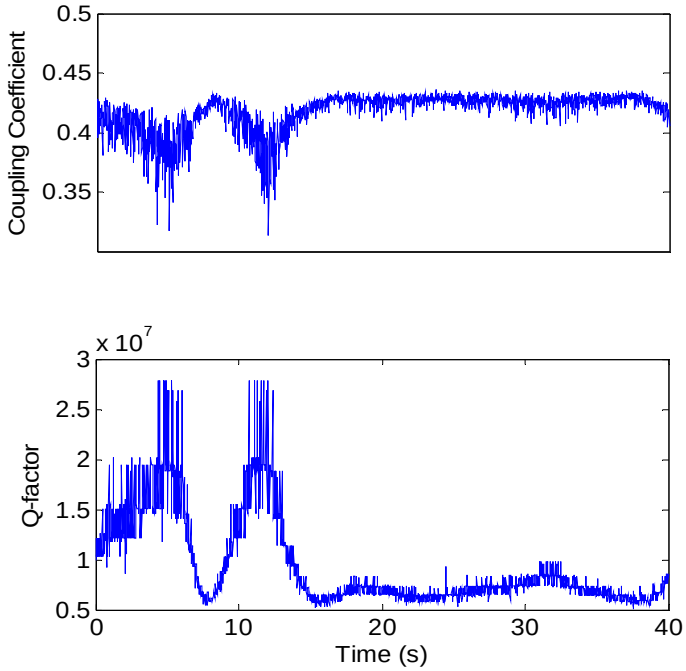

Figure 6.15 Coupling coefficient and *Q*-factor of the 40s trace of WGM in vacuum with a laser input power of 5mW.

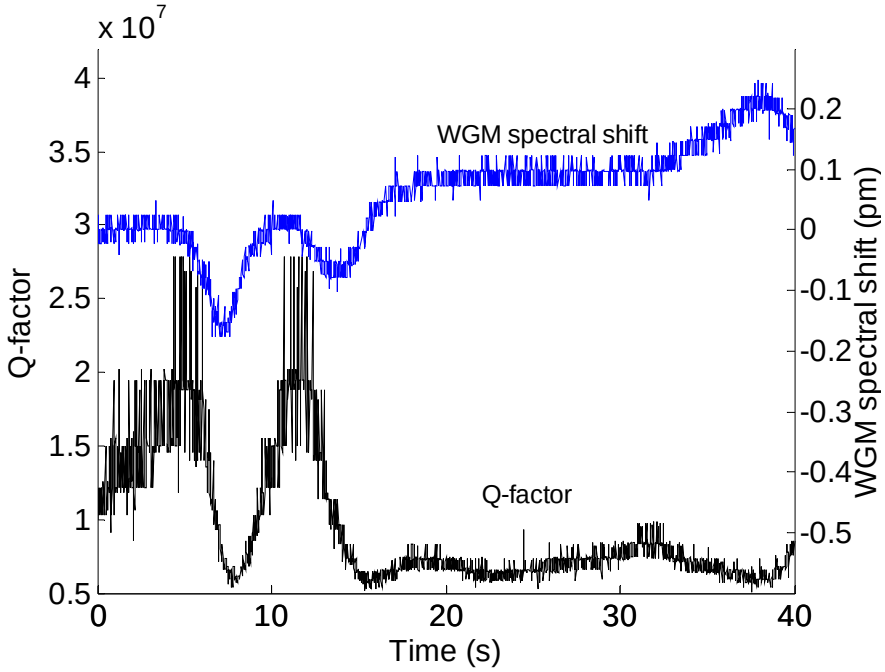

Figure 6.16 Comparison between of the fluctuations of Q-factor and WGM spectral shift noise of the 40s trace of WGM in vacuum with a laser input power of 5mW.

signal processing procedure, we have the WGM spectral shift noise shown in Figure 6.17. The amplitude and frequency component are similar as the case with un-attenuated laser

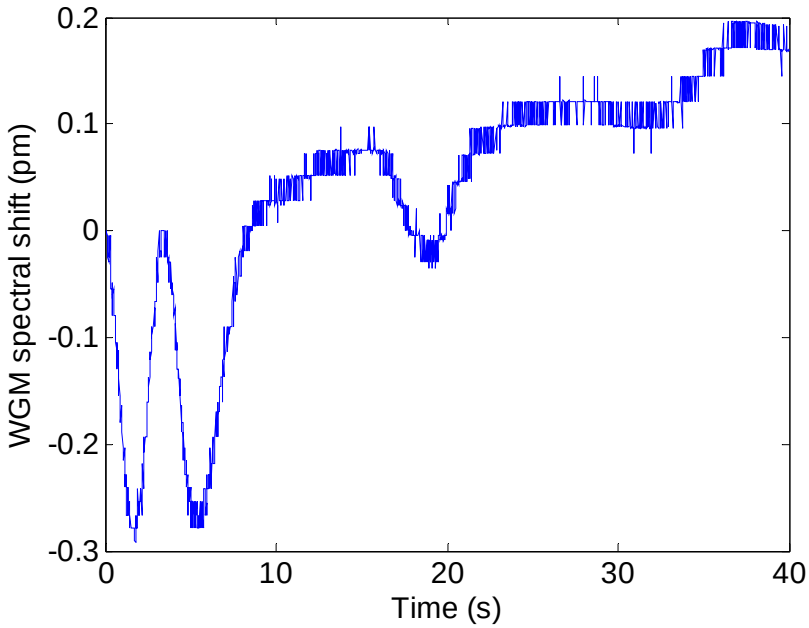

Figure 6.17 WGM spectral shift in 40s for WGM in vacuum based on reconstructed spectrum using FRR interferences with a laser input power of 0.05mW.

power. The *Q*-factor and coupling coefficient is shown in Figure 6.18, which still shows that they fluctuate inversely to each other. Figure 6.19 shows that shift profile still follows the *Q*-factor profile. Therefore, there is nothing new for the measurement with 20dB attenuated laser input power, which again proves that the noise has nothing to do with the laser scanning and heating. The laser heating effect should already reach steady state when the laser power is set to a level and stabilized during the tunings.

The bandwidth of the laser (DFB 1531nm) is 2MHz corresponding to a *Q*-factor of approximately 10^8, which is only one order magnitude higher than the *Q*-factors of the

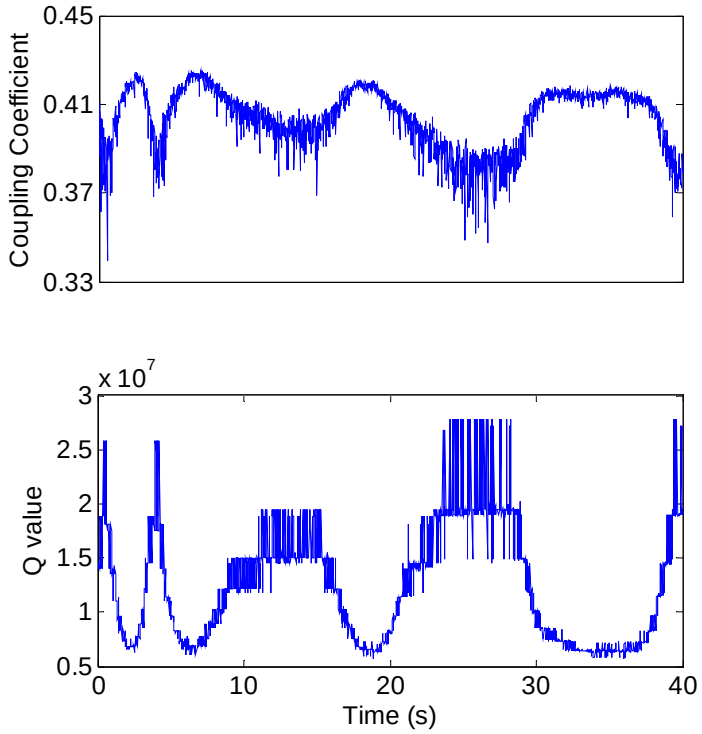

Figure 6.18 Coupling coefficient and *Q*-factor of the 40s trace of WGM in vacuum with a laser input power of 0.05mW.

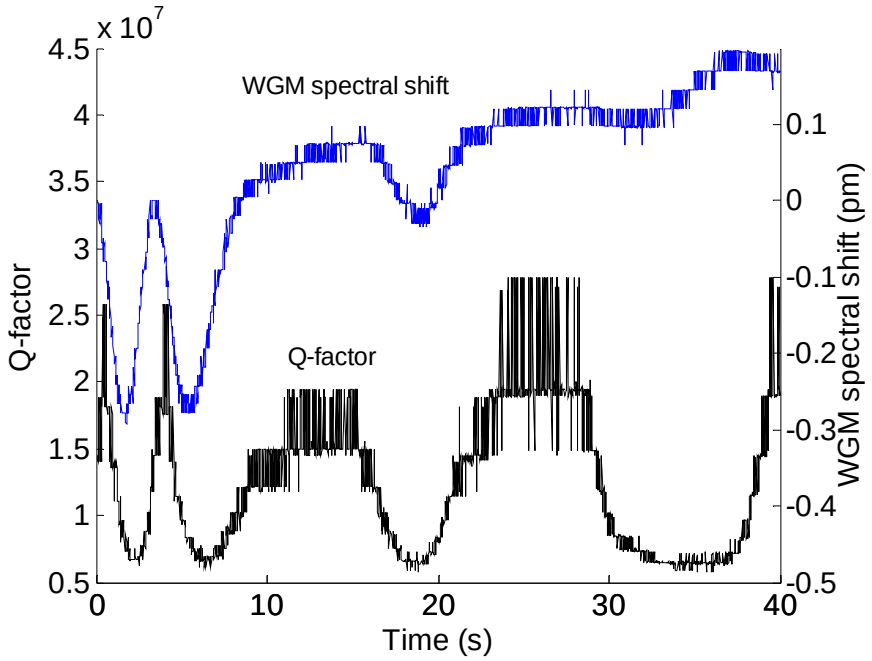

Figure 6.19 Comparison between of the fluctuations of Q-factor and WGM spectral shift noise of the 40s trace of WGM in vacuum with a laser input power of 0.05mW.

WGM observed in the last two tests. Thus, to see whether the WGM spectral shift noise result from the interference of the laser lineshape with the WGM, we study a WGM with *Q*-factor at a much lower level of ~10^5 in a poorly made microsphere (200μm in diameter). As shown in Figure 6.20, the spectral shift noise still looks similar as the ones of Q~10^7. As discussed in chapter 5, broader linewidth of the WGM degrade its resonance shift resolving power which contributes more significant noise on the major fluctuation. In addition, broader peak allows the higher chance of amplitude noise existence which is mainly caused by the detector's shot noise and laser's intensity noise. The peak spectral position is determined by the extremum data point of the peak profile. With added amplitude noise, the actual extremum is not likely to be at the exact center frequency of the Lorentzian shape as it should be. This may result in more noise overlapped with the simple digitization noise as seen in the case of higher *Q*-factor. At some location of major fluctuation, the total digitization noise amplitude can be around 0.05pm as seen in Figure 6.20. The coupling coefficient and *Q*-factor still fluctuate inversely to each other as shown in Figure 6.21. The noise amplitude on the *Q*-factor decreases significantly due to more data points describing the linewidth of the resonance. Figure 6.22 shows that the resonance shift profile still follows the *Q*-value variation in the 40s trace.

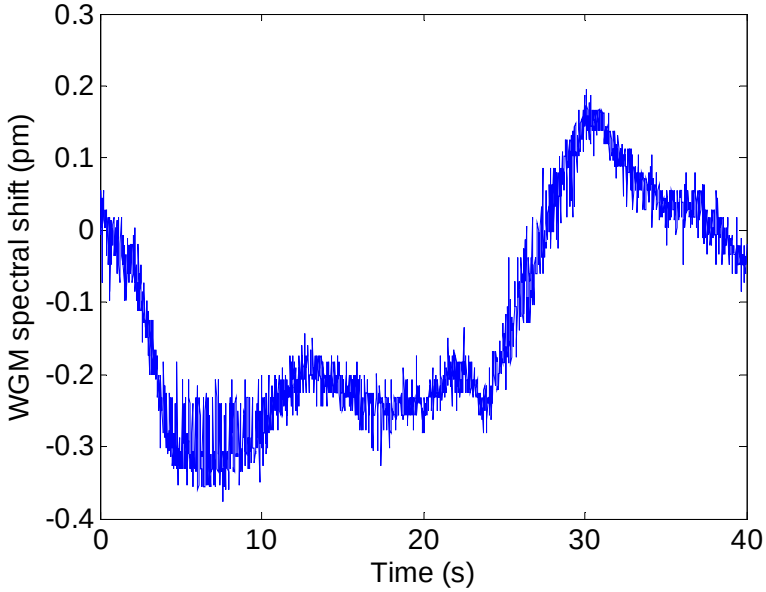

Figure 6.20 WGM spectral shift in 40s for WGM in vacuum based on reconstructed spectrum using FRR interferences with much lower *Q*-factors of ~10^5.

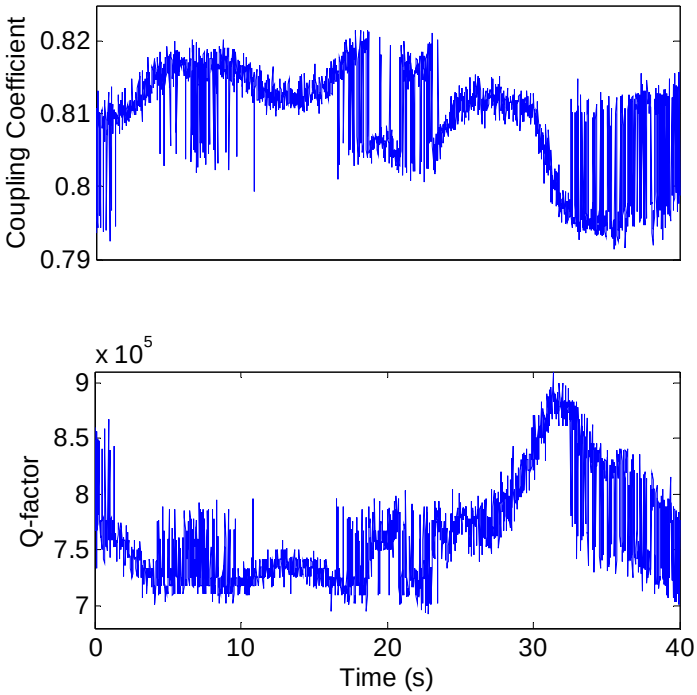

Figure 6.21 Coupling coefficient and *Q*-factor of the 40s trace of WGM in vacuum with much lower *Q*-factors of ~10^5.

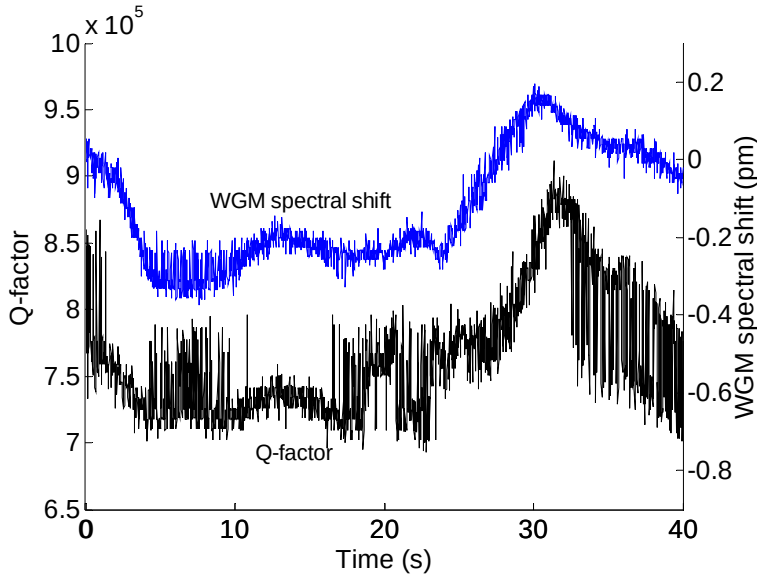

Figure 6.22 Comparison between of the fluctuations of Q-factor and WGM spectral shift noise of the 40s trace of WGM in vacuum with much lower *Q*-factors of ~10^5.

In summary, the WGM instability at different levels of laser power and different levels of *Q*-factors are measured. The resonance shift fluctuation is always within 0.4pm and has similar frequencies (approximately 0.1Hz~0.2Hz) and randomness. As analyzed above, the noise may result from the unstable coupling which is most likely caused by the mechanical instability of the very thin and suspended fiber taper contacting with the microsphere. Any tiny environmental vibrations and fluctuations of Van del Waals force in the coupling system may disturb the fiber taper a tiny bit. A proposed approach of solving this is to fabricate an on-chip waveguide for coupling light into the microsphere. A rigid waveguide is stable and the coupling is immune to external vibrations and any tiny forces fluctuations as long as the microsphere is also held firmly. However, the fiber taper is still the best time and cost economic choice for sensor studies. All the statements on the WGM sensor quality including the response time and ultrahigh-resolution are still valid as long as

coupling waveguide stability is improved. The methodology for WGM resonance instability characterization developed in this chapter applies to any kind of WGM coupling.

CHAPTER 7

SPECTRAL SHIFT RESPONSE OF OPTICAL WHISPERING GALLERY MODES DUE TO WATER VAPOR ADSORPTION AND DESORPTION

7.1 Introduction

Optical whispering-gallery mode effects in dielectric micro-resonators such as microspheres [18, 71, 63], microdisks [19, 72], or microrings [73] have been intensively investigated for the development of new biological and/or chemical sensors. The evanescent field of the WGM with a characteristic length of tens to hundreds of nanometers is sensitive to the refractive index change of the surrounding medium or to the binding of biological/chemical molecules to the resonator surface. A resonance frequency shift of the WGMs is induced when such events happen. The light-matter interaction is enhanced due to the long interaction length of the optical resonances associated with high quality factor WGMs. The high Q-factor is also correlated with narrow linewidths, which provide WGM-based sensors with high sensitivity when relying on a resonance frequency shift method of detection. Arnold *et al*. [18, 71] has demonstrated detection of protein molecules within an aqueous solution utilizing the refractive index change of the solution as measured by the shift of WGMs in silica microspheres. Armani *et al*. [74] also proved label-free single molecule detection with a micro-toroid resonator in aqueous solution, extending the technique to a dynamic range of 10^{12} in concentration. Krioukov *et al*. [72] demonstrated a sensor based on integrated optical microcavities which can measure a change of as little as 10^{-4} in refractive index of the surrounding medium.

Few prior studies have explored WGM resonances for gas-phase molecular detection. Rosenberger *et al.* [47] have proposed and studied an approach of cavity-enhanced laser

absorption spectroscopy using WGM for gas detection. However, only centimeter pathlengths were achieved which resulted in 10^4ppm detection levels for very strong infrared molecular absorption transitions. Locking and tuning of the WGM resonances through the spectral width of the gas absorption line proved challenging and limited the temporal response and accuracy of the technique.

For any potential evanescent-wave absorption spectroscopy based WGM gas sensor, a relatively large evanescent tail of the WGM is needed for high sensitivity concentration measurements. As the size of the evanescent tail is inversely proportional to resonator diameter, this favors smaller resonators. However, the potential loaded Q-factor that is proportional to the pathlength the light travels decreases drastically as the resonator's size decreases. Thus, making a small, tunable micro-resonator with ultra high Q is desired; however, producing such a spherical resonator with capabilities sufficient for ppm level detection of species is challenging.

In this chapter, we explore a potential WGM gas sensing method that uses a coated silica microsphere. The coating is designed to specifically adsorb only the probed gas molecules and be transparent to the laser wavelength used. The concept of coated microsphere gas sensing is illustrated in Figure 7.1. The refractive index of coating changes as it adsorbs gas molecules at different concentration levels which induces a resonance frequency shift of the WGM. The complexity of resonant absorption spectroscopy is avoided in this kind of method as the WGM resonances can be read using any laser frequency, as it is not required to be resonant with an optical transition associated with the molecule of interest. Furthermore, the measurement sensitivity is determined both by the size of the wavelength shift that can be resolved by the WGM peak and the sensitivity of the coating to the analyte species.

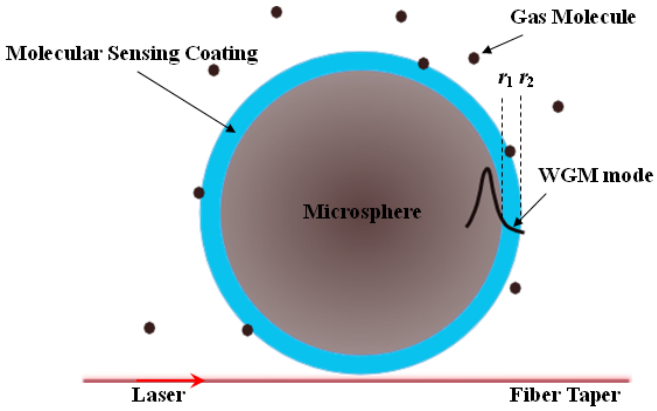

Figure 7.1 Illustration of the WGM gas sensing with coated microsphere.

We have designed and fabricated an optical resonator that is coated with a nanostructured layer of SiO_2 nanoparticles to study the response of the WGM spectral shift to water vapor concentration. The most prominent merit of SiO_2 as a humidity sensing material is its compatibility with the current microelectronics industry. The response and recovery times of the SiO_2 films are as short as in milliseconds, making them well suited to performing time resolved measurements [75]. However, most prior works have demonstrated reliable detection of water vapor concentration in excess of 20% [76] relative humidity (RH) at atmospheric pressure and room temperature. For example, Viegas *et al.* [77] recently demonstrated a humidity sensor based on a long-period fiber grating coated with a thin film of SiO_2 nanoparticles which can measure a RH range of 20% to 80%. For a long period fiber grating device described in that work, the minimum humidity detectivity was determined to be on the order of 1% RH [77]. In our study, utilizing a similar hydrophilic coating applied to a microsphere resonator, the WGM spectral shift response to water vapor concentration from 0% to 10% RH was measured to far exceed the previous minimum detectivity reported for a nanostructured SiO_2 coating.

It should be acknowledged that Lei Huang in Prof.Guo's group first get the idea of using SiO_2 coating for humidity sensing during a discussion with the author.

Understanding of the experimental coating process was jointly undertaken and the development of a useful coating was accomplished collaboratively between Lei and the author. In addition, WGM experiments using the coated device were done by the author with some assistance from Lei Huang. It should also be recognized that the atomic force microscopy of the coating is done by Ji Li in Prof.Huang's group with some assistance from the author and Lei Huang. Prof.Guo first got the insight in correctly analyzing the complex hysteresis effect of the coating with assistance from Lei Huang. The author would like to share the research credits on the recognized cooperation with Lei Huang and Ji Li.

7.2 WGM resonance in coated microsphere and coating refractive index sensitivity

For coated microspheres, knowledge of the evanescent wave penetration depth and its relation to radial mode number as well as to the sensitivity of the coated WGM sensor is crucial to understanding the experimental results. The radial distribution of the transverse electronic (TE) WGMs in a coated microsphere can be described by Mie theory [78]:

$$E_{l,n} = \begin{cases} A\psi_l(n_1 k_0^{(n)} r) & (r \le r_1) \\ C\psi_l(n_2 k_0^{(n)} r) + D\chi_l(n_2 k_0^{(n)} r) & (r_1 \le r \le r_2) \\ B\chi_l(n_3 k_0^{(n)} r) & (r_2 \le r) \end{cases} \tag{7.1}$$

where a Ricatti-Bessel function $\psi_l(z) = zj_l(z)$ and a Ricatti-Neumann function $\chi_l(z) = zy_l(z)$ are defined by use of lth spherical Bessel and Neumann functions $j_l(z)$ and $y_l(z)$, respectively. The refractive indices of the microsphere, coating and surrounding gas are described by n_1, n_2 and n_3. The terms r_1 and r_2 represent the radius of the original microsphere and the coated microsphere, respectively. $k_0^{(n)}$ is the amplitude of the wave vector in vacuum for nth-order radial WGM. Based on the fact that $E_{l,n}$ and $E'_{l,n}$ are

continuous at the boundaries of $r = r_1$ and $r = r_2$, the constants A, B, C and D can be determined as

$$
\begin{aligned}
A &= 1 \\
B &= \frac{\alpha - \gamma}{\alpha_1 - \gamma_1} \frac{\alpha_1 \sigma_1 - \beta_1 \gamma_1}{\alpha\sigma - \beta\gamma} \\
C &= \frac{\beta - \sigma}{\beta\gamma - \alpha\sigma} \\
D &= \frac{\alpha - \gamma}{\alpha\sigma - \beta\gamma}
\end{aligned}
\tag{7.2}
$$

where

$$
\begin{aligned}
\alpha &= \frac{\psi_l(n_2 k_0^{(n)} r_1)}{\psi_l(n_1 k_0^{(n)} r_1)} \\
\beta &= \frac{\chi_l(n_2 k_0^{(n)} r_1)}{\psi_l(n_1 k_0^{(n)} r_1)} \\
\sigma &= \frac{n_2}{n_1} \frac{n_2 k_0^{(n)} y_{l-1}(n_2 k_0^{(n)} r_1) - \frac{l}{r_1} y_l(n_2 k_0^{(n)} r_1)}{n_1 k_0^{(n)} j_{l-1}(n_1 k_0^{(n)} r_1) - \frac{l}{r_1} j_l(n_1 k_0^{(n)} r_1)} \\
\gamma &= \frac{n_2}{n_1} \frac{n_2 k_0^{(n)} j_{l-1}(n_2 k_0^{(n)} r_1) - \frac{l}{r_1} j_l(n_2 k_0^{(n)} r_1)}{n_1 k_0^{(n)} j_{l-1}(n_1 k_0^{(n)} r_1) - \frac{l}{r_1} j_l(n_1 k_0^{(n)} r_1)} \\
\sigma_1 &= \frac{n_2}{n_3} \frac{n_2 k_0^{(n)} y_{l-1}(n_2 k_0^{(n)} r_2) - \frac{l}{r_2} y_l(n_2 k_0^{(n)} r_2)}{n_3 k_0^{(n)} y_{l-1}(n_3 k_0^{(n)} r_2) - \frac{l}{r_2} y_l(n_3 k_0^{(n)} r_2)} \\
\gamma_1 &= \frac{n_2}{n_3} \frac{n_2 k_0^{(n)} j_{l-1}(n_2 k_0^{(n)} r_2) - \frac{l}{r_2} j_l(n_2 k_0^{(n)} r_2)}{n_3 k_0^{(n)} y_{l-1}(n_3 k_0^{(n)} r_2) - \frac{l}{r_2} y_l(n_3 k_0^{(n)} r_2)}
\end{aligned}
\tag{7.3}
$$

Therefore, a resonance wavelength for a specific polar mode number l and radial mode number n can be searched and established using a MATLAB code based on matching the boundary conditions.

(I) The case of $n_2 > n_1 > n_3$

Let us first study the case that the refractive index of coating is higher than that of the microsphere. Since the coating process usually spoils the Q-factor by one to two orders of magnitude, we use relatively big microsphere to maintain a decent resonance quality after coating. We study a microsphere with original diameter of 460μm which is the case in the experiment. A tunable 1653nm DFB laser (NLK1U5FAAA, NEL) is applied in the experiments. The refractive indices of the silica microsphere and surrounding gas are n_1=1.4682 and n_3=1, respectively. Assume the initial refractive index of the coating is n_2=1.6 and the coating thickness is 1μm, a first- and a fifth- radial order resonances are solved at wavelengths of 1653.13051nm (n=1, l=1263) and 1654.05424nm (n=5, l=1215), respectively, and plotted in Figure 7.2. Here the radial mode number refers to the number of radial mode intensity maxima propagating inside the original microsphere. However, a radial mode intensity maxima propagating in the coating is seen, which is unique for $n_2 > n_1 > n_3$ and when coating thickness is comparable to the resonance wavelength. The fractions of energy outside the original microsphere are 2.358% and 2.021% for first-and

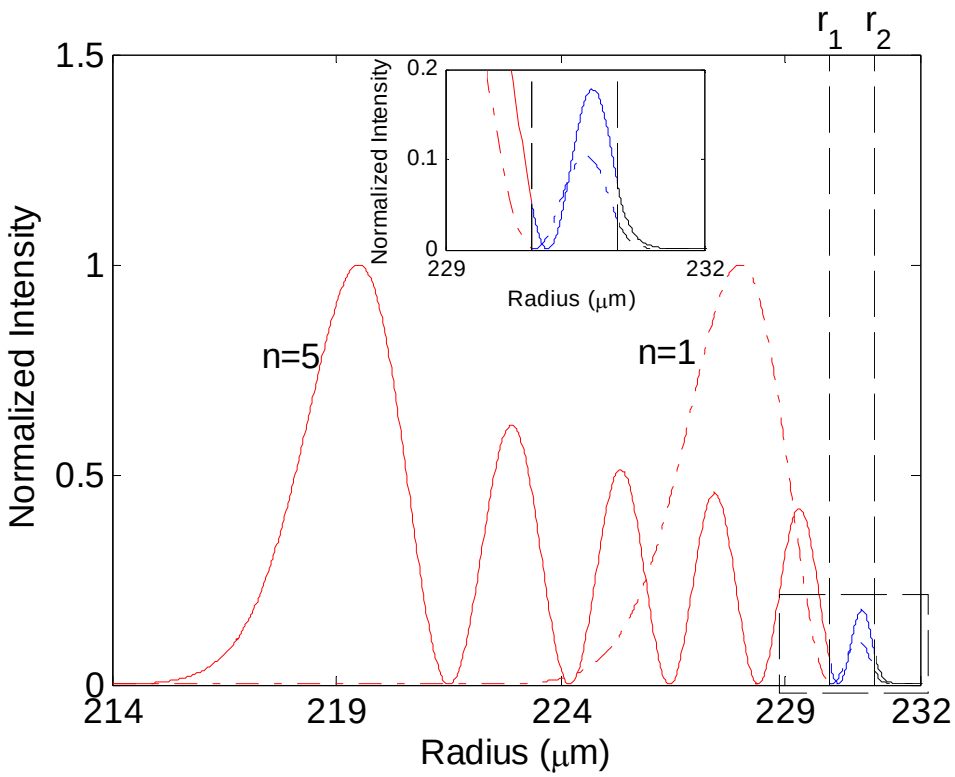

Figure 7.2 Intensity distribution of two TE WGMs (*n*=1, *l*=1263, dashed and *n*=5, *l*=1215, solid) with r_1=230μm and r_2=231μm. Dashed lines show the boundaries of the 1μm thick coating. Refractive indices: n_1=1.4862, n_2=1.6, n_3=1.0. The inset shows the evanescent tails and intensity in the coatings of the two radial modes in more detail.

fifth- order radial modes, respectively. Additionally, the fractions of energy in the coating are 2.204% and 1.817% for first- and fifth- order radial modes, respectively. Figure 7.3 shows that the first-order mode has a better refractive index sensitivity (26.9nm/RIU) in the coating than the fifth-order (22.3nm/RIU). It turns out that the ratio of the sensitivities (1.207) is approximately the same as the ratio (1.213) of the fractions of energy in the coatings, demonstrating that refractive index sensitivity of a mode in the coating is proportional to the mode's energy fraction in the coating.

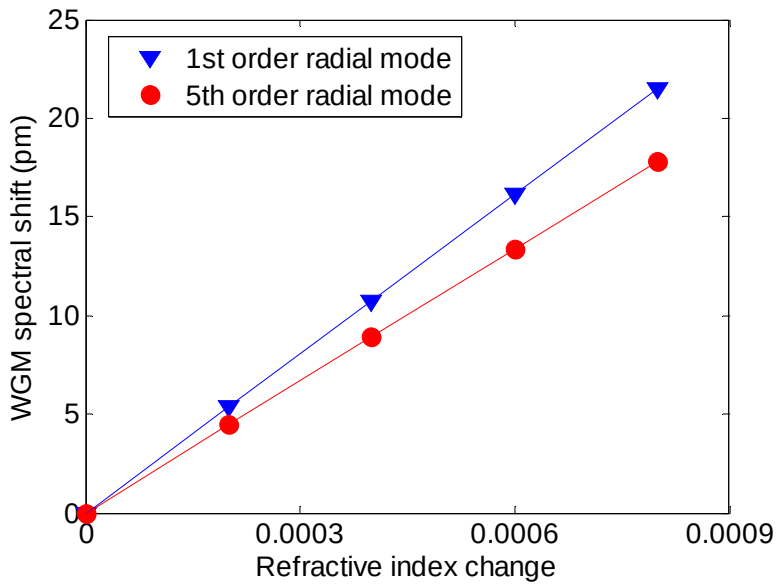

Figure7.3 Simulation of WGM spectral shift versus refractive index change of the coating for the case of n_2=1.6, coating thickness=1μm.

Thicker the coating degrades more severely the *Q*-factor. Thus, in experiment, we usually use a coating much less than 1μm. And specifically in our case, it is 330nm. Still assuming an initial coating refractive index of n_2=1.6, a first- and fifth- order radial mode can be solved at resonance wavelength of 1653.29204 (n=1, l=1270) nm and 1653.83131nm (n=5, l=1210), respectively as plotted in Figure 7.4. Almost no mode intensity maxima exist in the coating any more due to the much thinner thickness. However, surprisingly, the energy fractions of the modes increase comparing to the case of 1μm coating. They are 8.313% and 2.438% for first-and fifth- order radial modes, respectively, outside the original microsphere. Additionally, coating holds 7.149% and 2.009% of the fifth-and first- order radial modes energy, respectively. Figure 7.5 show that the first-order mode has significantly better refractive index sensitivity (87.6nm/RIU) in the coating than

the fifth-order (24.6nm/RIU). And the ratio of the sensitivities (3.56) is equal to the ratio of the fractions of energy in the coatings for the two modes.

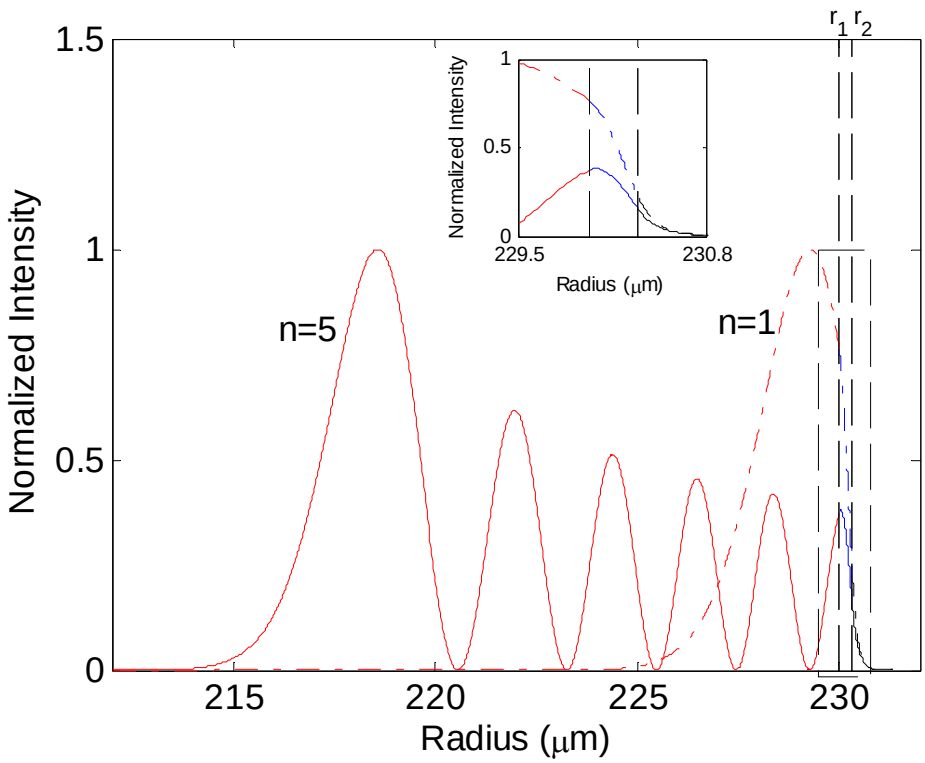

Figure 7.4 Intensity distribution of two TE WGMs (*n*=1, *l*=1270, dashed and *n*=5, *l*=1210, solid) with r_1=230μm and r_2=230.33μm. Dashed lines show the boundaries of the 1μm thick coating. Refractive indices: n_1=1.4862, n_2=1.6, n_3=1.0. The inset shows the evanescent tails and intensity in the coatings of the two radial modes in more detail.

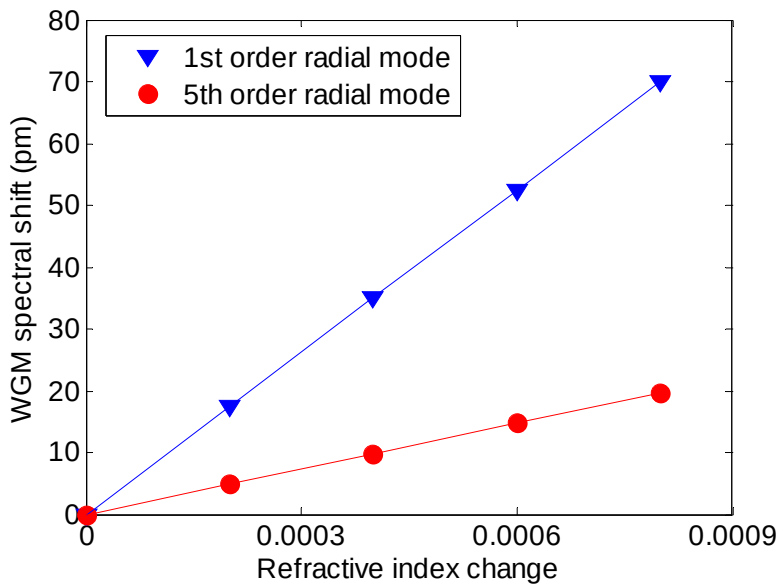

Figure7.5 Simulation of WGM spectral shift versus refractive index change of the coating for the case of n_2=1.6, coating thickness=0.33μm.

(II) The case of $n_1 > n_2 > n_3$

In our experiment, the initial refractive index of the SiO_2 nanostructured coating is lower than that of the microsphere, which is approximately 1.22 and increases as it absorbs water vapor. The coating thickness is 330nm. By matching the boundary conditions, a first- and fifth-order radial mode can be established at wavelengths of 1653.85848nm (n=1, l=1264) and 1653.59575nm (n=5, l=1216), respectively, as shown in Figure 7.6. Only part of the evanescent tail can exist in the coating due to low coating refractive. As a result, the energy fraction in the coating becomes much smaller. The evanescent fractions of energy outside the original microsphere are 0.426% and 0.393% for fifth-and first- order radial modes, respectively. The coating holds 0.379% and 0.358% for fifth-and first- order radial modes energy, respectively. Figure 7.7 show that the fifth-order mode has a slightly better (~6% larger) refractive index sensitivity (3.6nm/RIU) in the coating than the first-order

(3.4nm/RIU), both of which are one order magnitude smaller than the case with high coating refractive index (n_2=1.6). However, the ratio of the sensitivities (1.06) is still equal to the ratio of the fractions of energy in the coatings for the two modes.

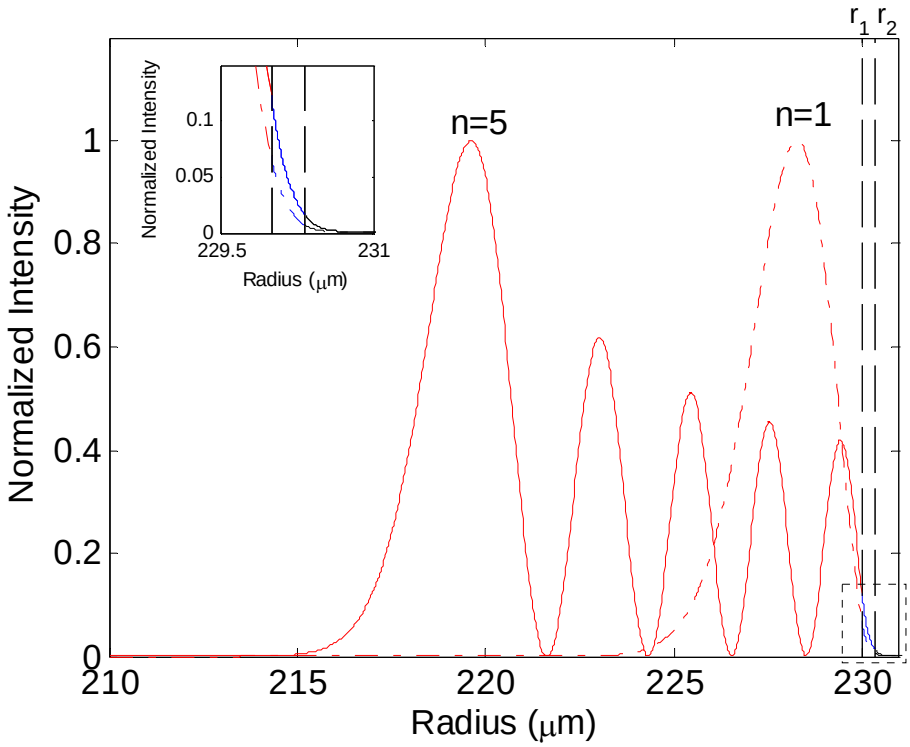

Figure7.6 Intensity distribution of two TE WGMs (*n*=1, *l*=1264, dashed and *n*=5, *l*=1216, solid) with r_1=230μm and r_2=230.33μm. Dashed lines show the boundaries of the 330nm thick coating. Refractive indices: n_1=1.4862, n_2=1.22, n_3=1.0. The inset shows the evanescent tail of the two radial modes in more detail.

The key results of refractive index sensitivities based on Mie theory analysis for different coating thicknesses and refractive indices in case (I) and (II) are summarized in Table 7.1. For a specific initial coating refractive index, it clearly shows that the refractive

index sensitivity is proportional to the energy fraction in the coating. The case of $n_2 > n_1$ allows significantly more energy fraction in the coating and therefore has sensitivities

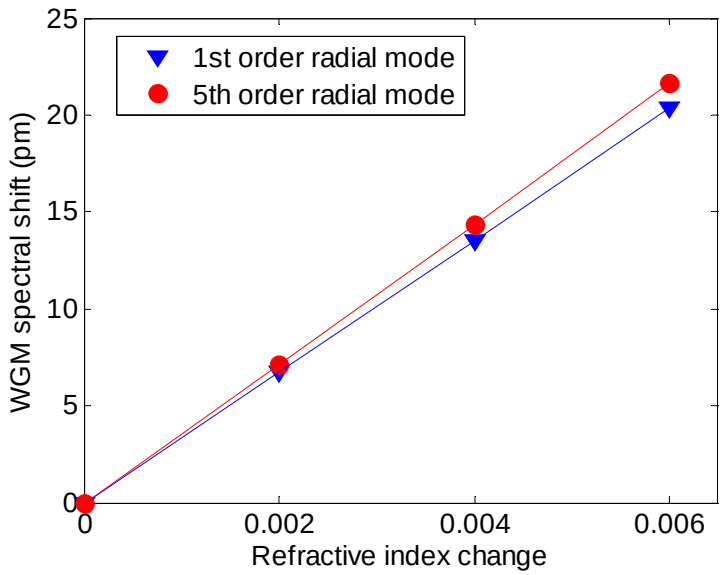

Figure7.7 Simulation of WGM spectral shift versus refractive index change of the coating for the case of n_2=1.22, coating thickness=0.33μm.

approximately one order of magnitude higher than the case of $n_1 > n_2$. According to the ratio of refractive index sensitivity against energy fraction in the coating, the case of $n_2 > n_1$ also has better refractive index sensing efficiency (1221~1227nm/RIU) than the case $n_1 > n_2$ (950nm/RIU). In the case of $n_2 > n_1$, the lower radial mode has significantly better sensitivity. However, in the case of $n_1 > n_2$, the higher radial mode has slightly better sensitivity. The design rule for achieving high refractive index sensitivity in the coating is that a lower radial mode excitation in a submicron coating with refractive index higher than the microsphere is most desirable, which is the case bolded in the table.

Table 7.1 Comparison of the refractive index sensitivities based on Mie theory analysis for different coating thicknesses and refractive indices.

Coating Thickness (μm)	Initial Coating Refractive Index	Radial Mode Order	Energy Fraction in the Coating	Refractive Index Sensitivity (nm/RIU)	Refractive Index Sensitivity / Energy Fraction in the coating (nm/RIU)
1	1.6	1st	2.204%	26.9	1221
1	1.6	5th	1.817%	22.3	1227
0.33	**1.6**	**1st**	**7.149%**	**87.6**	**1225**
0.33	1.6	5th	2.009%	24.6	1224
0.33	1.22	1st	0.358%	3.4	950
0.33	1.22	5th	0.379%	3.6	950

Another important factor that should be taken into account in determining the final achievable detectivity of a resonance spectral shift based sensor is *Q*-factor. The dominating loss mechanisms for a coated microsphere with diameter larger than 400μm are material absorption and Rayleigh scattering. Assume the energy fraction in the coating is f_c, equation (2.48) for calculating original microsphere Q_{absorb} can be modified as

$$Q'_{absorb} = \frac{2\pi\left[(1-f_c)n_1 + f_c n_2\right]}{\lambda\left[(1-f_c)\alpha_s + f_c\alpha_c\right]} \tag{7.4}$$

where α_s and α_c are the absorption coefficient of microsphere material (SiO_2) and coating material, respectively, at the resonance wavelength λ. Let $p = n_2 / n_1$ and $q = \alpha_c / \alpha_s$, we have

$$Q'_{absorb} = \frac{\left(1+\frac{f_c}{1-f_c}p\right)}{\left(1+\frac{f_c}{1-f_c}q\right)}\frac{2\pi n_s}{\lambda\alpha_s} = \frac{\left(1+\frac{f_c}{1-f_c}p\right)}{\left(1+\frac{f_c}{1-f_c}q\right)}Q_{absorb} \tag{7.5}$$

Due to the fact that $f_c << 1$, we have $f_c/(1-f_c) << 1$ which attenuate the effect of p and q. As shown in Table 7.1, relatively larger f_c happens when $n_2 > n_1$ (p>1) which indicates that it actually allows $\alpha_c > \alpha_s$ (q>1) without degradation of Q_{absorb} as long as p>q. With the attenuation factor $f_c/(1-f_c)$, the degradation of Q_{absorb} only happens when q is significantly higher than p. Thus, in the case of larger f_c which result in higher refractive index sensitivity, the quality factor related to material absorption is not necessarily degraded or not degraded significantly by the coating as long as the coating material does not have significant higher absorption coefficient. However, as indicated by equation (2.47), the loss due to Rayleigh scattering should be largely increased due to the much more significant coating surface roughness and possible porous structures in the coating, which may significantly decrease Q_{scat}. Thicker coating has more chance of inducing Rayleigh scatterings. However, fortunately, relatively large f_c exist in thinner coating with $n_2 > n_1$. As a conclusion, to obtain a high detectivity of a resonance spectral shift, a thin (submicron), uniform and smooth coating with refractive index higher than the original microsphere and low absorption coefficient is preferable if constant adsorption capability of gas molecules is assumed for the coating.

7.3 Experimental setup and methods

We adopted the technique of electrostatic self-assembly (ESA) for fabricating the SiO_2 nanoparticle-based film [75], which has the advantages of both self-assembly and molecular control of the structure of the coating, molecular layer by molecular layer. A microsphere, 230μm in radius formed on tip of a fiber, is introduced to a piranha acid solution (70% H_2SO_4, 30%H_2O_2) for 10 min to create a charged surface. Then, it is suspended in a magnetic stirrer and thoroughly washed in agitated deionized (DI) water for 5 minutes. After that, the microsphere is dipped into a colloidal suspension (LUDOX TM-40, diluted to 25mg/ml) of dissolved silica particles with an average diameter of 22nm at pH 2.0 for 15 min to form a monolayer of SiO_2 on the microsphere surface. After a similar DI water bath to remove excess adsorbed material, the microsphere is immersed for 15 min into a similar SiO_2 nanoparticles solution but with pH 10.0 so that another monolayer of SiO_2 is formed. The microsphere is again cleaned with DI water. This process is repeated until 20 monolayers of the nanoparticles are coated on the microsphere to form a thin film. The thickness of the film is approximately 330nm according to a similar study of ESA based fabrication of a similar multi-monolayer structure conducted by Corres *et al.* [75], who used a nano-Fabry-Perot measurement to determine layer thickness. The refractive index of the film is approximately 1.22 according to a simulation by Villar *et al.* [79] and increases as it absorbs water vapor.

Figure 7.8 shows an atomic force microscopy (AFM) image of the surface morphology of the nanostructured coating on the microsphere. The high surface porosity and roughness enhance the behavior of the film to the super-hydrophilic regime. The contact angle of this film as fabricated onto a glass slide is measured to be less than 5

degrees which indicates the super-hydrophilic property of the coated surface. Prior works have investigated water adsorption and desorption process into this type of nanoporous network associated with the SiO_2 nanostructured coating. It is widely accepted that the adsorption of water can be divided into two important steps. The first step at very low humidity levels occurs when specific adsorption happens onto hydroxyl groups through hydrogen bond (-H) interactions followed by formation of sub-monolayer coverage. In the second step of water vapor adsorption, capillary condensation leads to multilayer deposition of water [80]. Owing to differences in the nucleation and evaporation mechanisms inside the nanoporous network, the adsorption isotherm can show a significant hysteresis phenomenon that is mainly attributable to the capillary condensation phenomena.

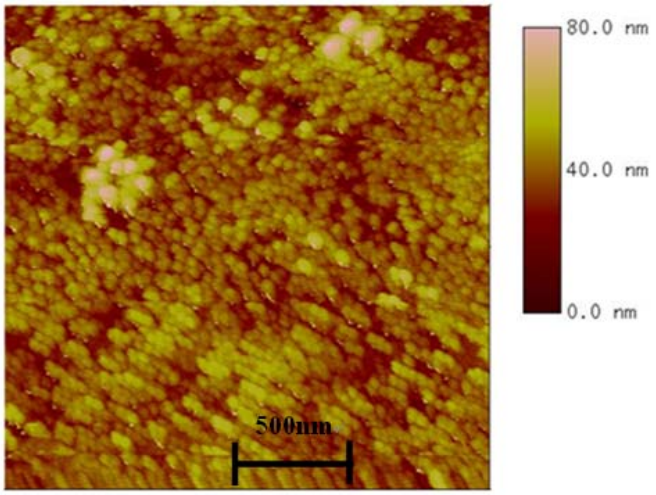

Figure 7.8 AFM image of the film composed by 20 monolayers of 20nm nanoparticles.

Following fabrication, the coated microsphere is positioned in contact with a fiber taper inside the vacuum chamber introduced in Chapter 6 as shown in Figure 7.9. A commercial

relative humidity (RH) sensor (Omega OM-DVTH) with a 10s time constant and a resolution of 0.01%RH is placed near the microsphere to measure and record humidity changes inside the chamber. Nitrogen purging for several hours is used to decrease the humidity in the vacuum chamber to near 0% (within the accuracy ±2%RH of the commercial RH sensor). A water vapor source (wet cotton stick) is then inserted into the chamber through another port to increase the humidity in the chamber in a controlled manner through evaporation. Laser light from a tunable DFB laser diode (1653nm) is coupled into the coated microsphere for WGM by evanescent coupling from the adiabatic fiber taper. The tunable laser repeatedly scans across a wavelength range of approximately

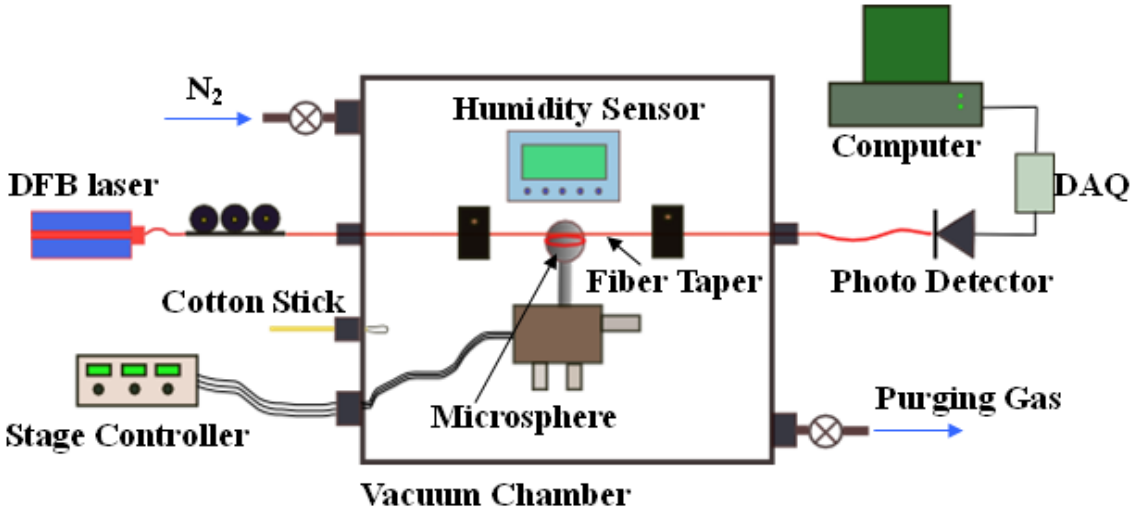

Figure 7.9 Experimental setup for the very low humidity (0%~10%) sensing.

170pm using sawtooth current modulation to resolve the spectral location of the WGM as a function of the changing environmental parameters. The WGM spectral positions are recorded at the output end of the fiber taper by detection of the transmitted light intensity as

a function of time, which is then temporally correlated with the wavelength modulation of the laser.

7.4 Results and discussions

After examining the role of radial order in sensitivity in case (II) of section 7.2, experimental measurements of water vapor sensitivity of the WGM associated with the coated microsphere were performed in the vacuum chamber under controlled humidity variation. As shown by the inset of Fig7.10, the RH in the chamber decreases slowly from 10% to 0% at temperature T=298.2K in 9140s by slow nitrogen purging, and then increased back to 10% slowly in 4120s by the insertion of a humidity source. This process is slow enough to ensure that the temporal response of the commercial humidity sensor is sufficient to fully resolve the humidity changes. In addition, the relatively long time for humidity changes allows for a spatially uniform humidity environment to be maintained in the chamber through diffusion.

As the humidity of the chamber decreases, the water desorbs from the pre-hydrated nano-structured silica film, causing the effective refractive index of the coated layers to decrease, hence blue-shifting the WGM resonance wavelength. Once the chamber humidity reaches the minimum value, the water vapor source increases the humidity and the water begins to be adsorbed by the nano-structured silica film, starting from sub-monolayer coverage and progressing to physisorption of bulk water into the film. As the water occupies the nanoporous network, the effective refractive index is increased,

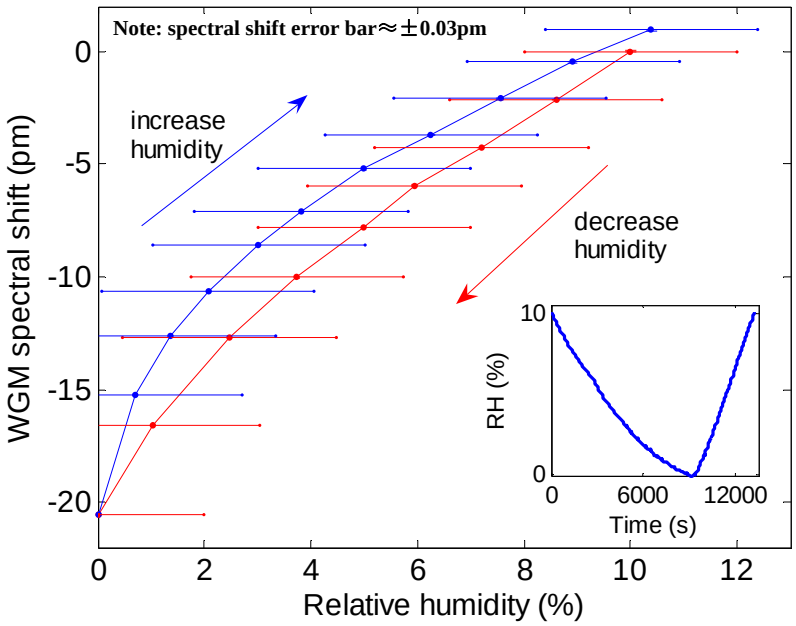

Figure 7.10 WGM spectral shift versus relative humidity change at 298.2K, inset: humidity change versus time.

while the resonance of the WGM shifts to larger wavelengths. The temperature inside the chamber is maintained at 298.2±0.1K during the test, as measured by the commercial sensor (0.01K resolution).

To obtain the WGM temperature sensitivity of this coated microsphere in the humidity test, the RH is kept at a constant of 5% and the spectral shift is measured against a temperature change of 297.7K to 298.7K in the chamber. The sensitivity to temperature changes is 13.2±0.01pm/K, showing that the thin coating does not significantly affect the overall temperature sensitivity of the micro-resonator. The spectral shift of a randomly selected, strongly-coupled WGM versus RH is shown in Figure 7.10, corrected for any temperature variations during the test. Horizontal error bars illustrate the uncertainties estimated by the accuracy (±2%RH) of the commercial RH sensor. Vertical error bars (i.e.

error bar of spectral shift) are obtained as the 95% confidence interval (±0.03pm) calculated from the five spectral shifts (from the five scans in 0.1s) recorded at each humidity value. However, in the subsequent similar tests during several days, the range of WGM spectral shift for humidity change between 0%~10% gradually drops to about 15pm~16pm. The repeatability of the curve in Figure 7.10 is not good in this sense. As shown in Figure 7.7, the sensitivity of the fifth order mode is only 6% higher than that of the first order radial mode in a shift of 20pm (relative humidity change of 10%). Since the selected WGM has an order less than 5th order confirmed by wider range laser tuning observation, this small difference can be neglected when comparing with the experiment result. In this experiment, the WGM spectral shift is approximately 16pm during the humidity loading phase and 18pm during the humidity unloading phase of the experiment which corresponds to refractive index changes of 0.0046 and 0.0052 RIU, respectively, using Figure 7.7. Therefore, the method has a sensitivity of 2.9×10^{-4} RIU/pm of spectral shift.

The minimum detectivity of this technique depends upon the ability to determine small spectral shifts relative to the initial position, which is dependant on the *Q*-factor of the coated microspheres. The *Q*-factor of the WGM used in this study is 0.8×10^{6}. From prior experience, a shift of 1/100 of the related linewidth can be easily resolved by the detection scheme employed, which correlates to a spectral shift sensitivity in the range of ~0.02pm. Using the sensor responsivity at very low humidity (0.02 pm/ppm H_2O) to estimate the minimum detectivity, a change of 1 ppm H_2O (0.003 %RH) should be resolvable using coated WGM microspheres. Finer resolution could be achieved if such a coated microsphere is fabricated with a higher *Q*-factor, however, limitations in our

fabrication process typically limit the maximum achievable intrinsic Q value to less than 10^9. The coated microsphere geometry represents a significant enhancement of low humidity detection when compared to long period fiber grating methods that employ similar coatings. In addition, we can see that the coating behaves similarly in the spherical geometry for the microsphere and the cylindrical geometry for the fiber optic sensors as the humidity sensitivity of the coating is measured to be 5.8 x 10^{-6} RIU/ppm H_2O in this study as compared to the range of $3\times10^{-6} \sim 8 \times10^{-6}$ RIU/ppm H_2O as demonstrated by Viegas *et al*. [77].

Separation between the sensitivity of the coated WGM microsphere during the humidity loading and unloading process is seen, suggesting a significant hysteresis effect, as shown in Figure 7.10. This likely results from the fact that mechanisms for the adsorption and desorption of water molecules for the superhydrophilic coating are considerably different and not exactly inverse of each other. To study the dynamic transport of water molecules between the thin nano-coating and surrounding environment, a calibration test with continuous step changes of humidity is performed. The humidity source is repeatedly inserted for a short time and then removed from the chamber to create the step humidity step increases, while an equivalent step humidity decrease is achieved by short duration nitrogen purging. Temperature variation is maintained within 0.08K and effect of temperature variation is corrected for in all test results. As shown in Figure 7.11, the WGM spectral shift appears to exhibit two distinct dynamic phenomena in response to the step variation in environmental humidity. The WGM shift closely follows the initial step change of the humidity suggesting prompt adsorption and desorption of water molecules to and from the nano-coating. This fast response time constant (< 1sec) of the

nano-coating was one of the primary reasons it was selected for humidity measurement by our and other research groups. However, there also appears to be a long time constant process (~ 700 sec) which seems to counteract the refractive index change of the nano-coating.

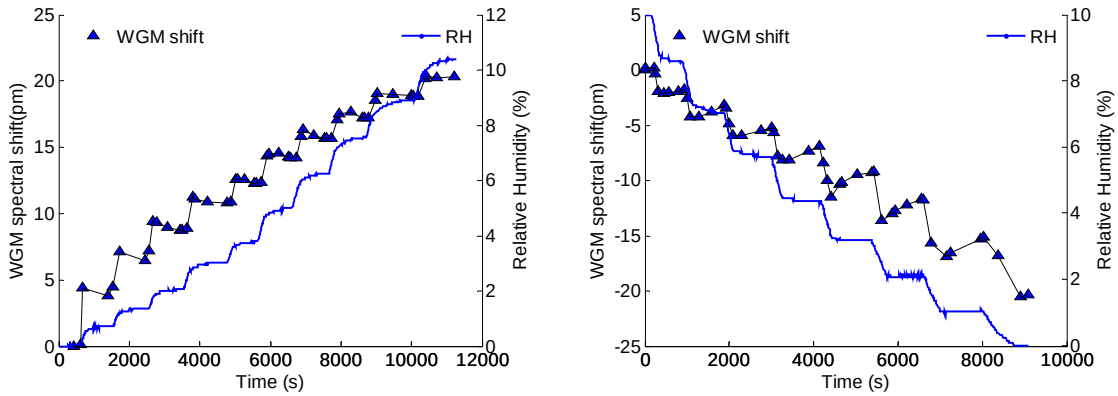

(a) (b)

Figure 7.11 WGM spectral shift with continuous step change of humidity at 300K, (a) humidity step increase (b) humidity step decrease.

Figure 7.11 shows that after an initial step change in the WGM spectral position, the resonant wavelength slowly relaxes to an intermediate value. This phenomenon indicates that the dynamic adsorption and desorption processes tends to return to the initial water concentration level in the coating when the source for sustaining the humidity gradient is removed even though the humidity in the vacuum chamber remains constant. In addition, this shift retraction phenomenon is more significant at lower humidity levels.

For further investigation, we examined the stability of the WGM shift as a dynamic process when the humidity source is absent for a long period of time. As shown in Figure 7.12, the spectral shift decreases and tends to a constant value within 1000s after a single humidity increase step change, where the final spectral shift level is still significantly

higher than the initial level. However, the spectral shift almost completely retracts and returns to its initial level for the single humidity decrease step change. We can conclude that the spectral shift for the nano-coated WGM microsphere depends on its prior humidity history in addition to the response related to the relatively long time constant associated

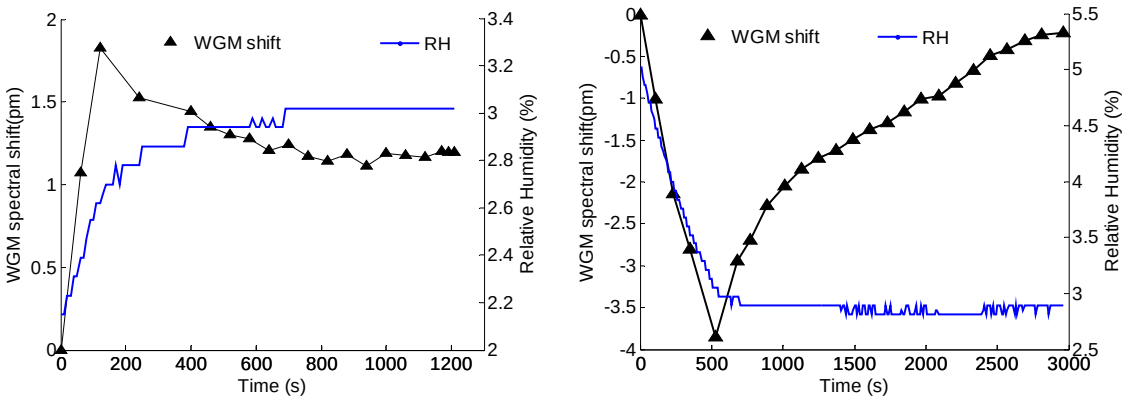

(a) (b)

Figure 7.12 WGM spectral shift with single step change of humidity at 300K, (a) humidity step increase (b) humidity step decrease.

with the slower dynamic process. Clearly, desorption and adsorption are complex processes for this kind of coating at lower humidity levels and their effects on the sensitivity, stability, and temporal accuracy of nano-coated WGM microspheres preclude further development of this concept into a steady humidity sensor for the low RH range. The sensing methodology appears to be better suited to dynamic humidity measurements where the measurement time scale involved is less than 100 sec.

The physical phenomenon which gives rise to the multiple time constants seen in Figure 7.12 is also responsible for the hysteresis behavior shown in Figure7.10. Due to behavior of the complex water vapor desorption process from the coating during periods of

humidity decrease and its extremely long time constant, the sensitivity of the coated WGM microsphere during decreasing humidity conditions is much lower than that of the increasing humidity environment. If the humidity changes occurred over much faster time scales (with changes on the order of 10 seconds or less), the two curves in Figure 7.10 would display similar sensitivities and exhibit a much better overlap.

7.5 Conclusion

In summary, we have analyzed the WGM spectral shift induced by the refractive index change in the coating by Mie theory and presented experimental results of the spectral shift response of optical WGMs for a SiO_2 nano-particle coated microsphere in response to environmental humidity changes. Significant response using the nano-SiO_2 particle coating is achieved at very low humidity level (<10%), which far exceeds the sensitivities reported by prior efforts. However, the coating appears to be exhibit poor stability due to its demonstrated significant hysteresis effect and long effective time constant. The dynamic adsorption and desorption processes of water molecules interacting with this coating are revealed by the WGM spectral shift during the step changes in humidity. The water concentration in the coating tends to return to its initial value when the source for the humidity gradient is removed even though the chamber humidity remains constant. However, this study clearly shows the merit of optical resonance methods as a useful measurement technique for determining surface interactions and transport dynamics within thin film coatings. In addition, if the coating refractive index can be controlled or modified by doping to be higher than the refractive index of the microsphere, the detectivity may be improved one order of magnitude better as shown in the Mie theory analysis.

CHAPTER 8

GAS MOLECULAR ABSORBTION SPECTROSCOPY BASED ON OPTICAL WHISPERING GALLERY MODE

8.1 Introduction

For ultra-sensitive detection of trace gas species, cavity ringdown spectroscopy (CRDS) has been previously shown to be a compact method for enhancing molecular absorption techniques. Through the use of a resonant cavity, absorption path lengths can be increased from the physical size of the resonator (usually the order of 1m for meso-scale CRDS) to several kilometers. Through the selection of appropriate absorption transitions, this method can allow sub-ppm detection of trace species with a wide dynamic range (~ 10^4). CRDS offers great enhancement of the absorption optical path length with minimal coupling to the cavity mode resonances. However, due to the small fraction of energy storage in the cavity (and thus leaking out per cavity pass), high power lasers are required to detect the ring down signal. As long as the pulse duration of injected light is shorter than the round-trip time within the cavity, and the laser linewidth is smaller than the absorption features of interest, pulsed CRDS is a straightforward and very sensitive technique for obtaining the absorption spectrum of dilute or weakly absorbing gas-phase species [81], particulate matter [82], and acetylene using femtosecond lasers [83]. Pulsed CRD offers high sensitivity over a potentially wide spectral range by use of a broadly tunable pulsed laser and a relatively simple setup [84].

However, the use of pulsed lasers also imposes some limitations on the meso-scale CRDS technique. The intensity of the light coupled into and out of the cavity is small, as a

consequence of reduced spectral overlap between cavity modes and laser linewidth as well as a lack of significant light buildup within the cavity. Moreover, for most practical pulsed laser systems, interference effects within the ring-down cavity preclude the use of simple models to describe the decay of light within the cavity as has been extensively demonstrated. In addition, the spectral resolution of pulsed CRDS is limited by the bandwidth of the pulsed laser (~typically 0.2 cm-1), which is often too large for direct recording of high-resolution spectra [85]. Finally, the relatively high cost of typical pulsed tunable laser systems in the infrared spectrum often prohibits the use of pulsed CRD for many industrial applications.

With the development of narrow bandwidth diode laser in the near infrared (NIR) spectrum due to advancements in optical communication, trace gas species with infrared active transitions is now common using continuous wave (CW) laser sources [86]. For typical CW cavity ringdown spectroscopy, two mirrors (usually R > 99.9%) are used to form a stable optical resonator (linear or ring resonators are common) with a discrete set of resonance frequencies. To couple a narrow linewidth laser effectively into the cavity, the laser wavelength must overlap with a cavity resonance frequency. For meso-scale CRDS measurements of trace species, the cavity length is typically modified by mounting one mirror on a piezoelectric transducer which allows for periodic tuning of the resonance frequencies over a small range [87]. Then, every time the laser frequency and cavity resonance overlap, laser power is strongly coupled into the cavity and accumulated through a build-up process. Typically, a threshold circuit coupled with the optical detector is used to detect sufficiently strong build-up events and trigger an acousto-optical modulator (AOM), which serves to deflect the laser beam and decouple it from the resonant cavity.

After the beam is deflected, the light intensity in the cavity decays exponentially (known as the cavity ringdown) owing to fixed roundtrip losses due to mirror reflectivity, Rayleigh and Mie scattering in the measurement volume, and optical absorption from the test gas.

While advanced in CRDS systems have increased rapidly, the systems are still bulky laboratory-scale devices which are neither portable nor field deployable, in general. Additionally, specialized high reflectivity mirrors are required for the resonant cavity, usually with limited spectral range (~ 50nm). With the development of nanofabrication technologies and microscale optical system, entirely new areas of CRDS exploration, or more generally, the cavity-enhanced absorption spectroscopy are possible using microresonant cavities based on whispering galley mode (WGM) resonators. WGM resonators utilize total internal reflection of evanescently coupled light to create extremely high *Q*–factor cavities with reduced round trip losses. This resonator geometry and energy storage capability make WGMs the ideal microscale building block for a novel cavity-enhanced spectrometer with high sensitivity and ultra wide tunability (as total internal reflection is a broadband phenomenon which does not rely on a specialized reflective coating).

In this chapter, theory of molecular absorption spectroscopy is introduced for simulation of trace gas absorption spectral profile based on HITRAN data base [88]. Cavity-enhanced gas absorption spectroscopy based on WGM are theoretically examined and reviewed for three types of techniques i.e. cavity ring down spectroscopy (CRDS), Q-spoiling, dip-depth variation based on an envisioned gas, methane (CH_4). An experimental setup is designed and built for characterizing the WGM system in the

absorption based gas detection. The experimental result is provides insights for clear directions for future endeavors.

8.2 Theory of molecular absorption spectroscopy

The well known Beer-Lambert relation for a uniformly absorbing medium of length L (cm) can be expressed as:

$$T_v = \left(\frac{I}{I_0}\right)_v = \exp(-k_v L) \tag{8.1}$$

where T_v is the transmitted intensity fraction. I and I_0 are the transmitted and incident spectral intensities, respectively at a particular transition frequency v. The spectral absorption coefficient k_v (cm^{-1}) can be expressed as [89]

$$k_v = S_i \phi_v P x_j \tag{8.2}$$

where S_i [cm^{-2}atm^{-1}] is the absorption transition's linestrength, ϕ_v [cm^{-1}] is the lineshape function, P is the total pressure of the medium and x_j is the mole fraction of the absorbing species. The linestrength of an absorption transition depends on the population in the lower quantum state, which is a function of the Boltzmann fraction, and the probability of the transition, which depends on specific spectroscopic constants associated with that molecule's particular transition. The molecular spectroscopic database, known under the acronym HITRAN, has been established to provide fundamental parameters to represent molecular properties in atmospheric absorption transition analysis. HITRAN uses a number-density dependent version of linestrength, S^*[cm^{-1}/(mol·cm^{-2})] which needs to be converted to the pressure-dependent version of linestrength, S [cm^{-2}atm^{-1}] in equation (8.2) as

$$S[cm^{-2}atm^{-1}] = \frac{S^*[cm^{-1}/(mol \cdot cm^{-2})] \times n_i[mol \cdot cm^{-3}]}{P_i[atm]} \tag{8.3}$$

where n_i is the number density of species i, and according to the ideal gas law, we have

$$n_i = \frac{P_i}{kT} \tag{8.4}$$

Plugging equation (8.4) in (8.3) gives further simplification as

$$S[cm^{-2}atm^{-1}] = 7.34 \times 10^{21} \frac{1}{T} \times S^*[cm^{-1}/(mol \cdot cm^{-2})] \tag{8.5}$$

where T is the temperature in unit of Kelvin.

The lineshape function, ϕ_ν, describes the relative variation in the spectral absorption coefficient with frequency. It is defined such that the spectral integral over frequency is unity:

$$\int_{-\infty}^{+\infty} \phi_\nu d\nu = 1 \tag{8.6}$$

The width of the lineshape function results from various broadening mechanisms that perturb the transition's energy levels. The dominant broadening mechanisms are Doppler broadening which is inhomogeneous resulting from molecular thermal motion and collisional broadening which is homogeneous resulting from molecular collisional effects.

Doppler broadening produces a Doppler shift of each velocity class of the molecular velocity distribution. Assuming the velocity distribution is Maxwellian, the resulting lineshape is a Gaussian profile [89]:

$$\phi_D(\nu) = \frac{2}{\Delta\nu_D}\left(\frac{\ln 2}{\pi}\right)^{1/2} \exp\left\{-4\ln 2\left(\frac{\nu - \nu_0}{\Delta\nu_D}\right)^2\right\} \tag{8.7}$$

The Doppler halfwidth (FWHM) $\Delta\nu_D$ is given as [89]

$$\Delta v_D = 7.1623\times10^{-7} v_0 \left(\frac{T}{M}\right)^{1/2} \tag{8.8}$$

where v_0 [cm^{-1}] is the linecenter of a transition, T [K]is the temperature and M is the molecular weight in grams/mole.

The lineshape for collisional broadening takes the form of a Lorentzian function [89]:

$$\phi_C(v) = \frac{1}{2\pi}\frac{\Delta v_C}{(v-v_0)^2 + (\Delta v_C/2)^2} \tag{8.9}$$

The Collisional halfwidths (FWHM), Δv_C for species A is modeled as the product of the total pressure and sum of the mole fraction for each perturber species B multiplied with its process-dependent collisional halfwidth [90]:

$$\Delta v_C = P\sum_B x_B 2\gamma_{A-B} \tag{8.10}$$

where 2γ varies with temperature according to the following expression [89]

$$2\gamma(T) = 2\gamma(T_0)\left(\frac{T_0}{T}\right)^m \tag{8.11}$$

where T_0 is the reference temperature, and m is the temperature exponent which varies with transition and collision partner. m=0.5 can be derived using simple kinetic theory based on the 'hard-sphere' collisions.

The resulting lineshape profile is calculated as the convolution of the Doppler and collision broadening profiles:

$$\phi_v(v) = \int_{-\infty}^{+\infty} \phi_D(u)\phi_C(v-u)du \tag{8.12}$$

This convolution can be modeled as a Voigt profile $V(a,w)$ if the Doppler and collision broadening are of similar magnitude. The Voigt a parameter indicates the relative significance of Doppler and collisional broadening [89]:

$$a = \frac{\sqrt{\ln 2}\Delta v_C}{\Delta v_D} \tag{8.13}$$

And the non-dimensional line position w parameter is [89]

$$w = \frac{2\sqrt{\ln 2}(v - v_0)}{\Delta v_D} \tag{8.14}$$

Equation (8.12) can be modified to [89]

$$\phi_v(v) = \frac{2}{\Delta v_D}\left(\frac{\ln 2}{\pi}\right)^{1/2} V(a, w) \tag{8.15}$$

as a good approximation of the lineshape function.

8.3 An estimate of CRDS based on WGM

As introduced in Chapter 2, the incident laser can be suddenly blocked off when the WGM is fully excited. In the case that the sum of blocking time and detector response time constant are much smaller than the CRD time constant, an exponential decay signal could be observed at the transmission end due to the energy stored in the WGM coupling back into the fiber. The decay time can be expressed as [90]:

$$\frac{1}{\tau} = \frac{[T + R + f_{eva} k_v(v) Lc]}{L} \tag{8.16}$$

where τ is the decay time constant, L is the cavity length, T is the propagation loss, R is the mirror reflection loss, k_v is the spectral absorption coefficient as introduced in equation (8.2), f_{eva} is the energy fraction of evanescent field and c is the speed of light. The ring-down decay time without the presence of the absorbing sample is measured independently (τ_0) and thus the sample absorption coefficient can be calculated from difference between the two measured ring down times [90]:

$$f_{eva}k_{\nu}(\nu)=\frac{1}{c}\left(\frac{1}{\tau}-\frac{1}{\tau_0}\right) \tag{8.17}$$

The measurement sensitivity depends on the rms shot-to-shot noise (σ_τ/τ) of ring-down decay time constant τ and on the equivalent path length ($c\tau_0$) in the WGM resonator.

Suppose we detect methane (CH_4) using WGM, a strong absorption line selected is at 1653.7222nm (6046.9657cm^{-1}). At room temperature 298K, from HITRAN, the linestrength is 1.309×10^{-21} $[cm^{-1}/(mol\cdot cm^{-2})]$, air-broadening halfwidth is $\gamma_{air}=0.0657$ [cm^{-1}atm^{-1}], self-broadening halfwidth is $\gamma_{self}=0.082$ [cm^{-1}atm^{-1}] and 1% (10000ppm) CH_4 is used. Using the theory of molecular absorption spectroscopy, the simulated absorption spectral linestrength profile is shown in Figure 8.1. The *FWHM* of the profile is 0.0368nm (4GHz), which is much larger than the *FWHM* (18MHz) of a WGM with Q=10^7. Thus, a WGM with Q>10^7 can be used to scan the absorption profile with negligible convolution effect. At the three dashed-line indicated spectral positions, i.e., 6046.8118[cm^{-1}], 6046.8882[cm^{-1}] and 6046.9647[cm^{-1}] shown in Figure 8.1, the absorption coefficients are 2.4371×10^{-4}[cm^{-1}], 6.6303×10^{-4}[cm^{-1}] and 1.5369×10^{-3}[cm^{-1}], respectively. A Q-factor of 10^8 results in a decay time of τ_0 =87.73ns according to equation (2.56) with absence of absorbing medium. If we can tune the WGM and locate it at the three indicated spectral positions and assume f_{eva}=0.4% (for first order radial mode excitation in a sphere with D=210μm), the decay time becomes 87.51ns, 87.12ns and 86.33ns, respectively, according to equation (8.17). The maximum decay time difference is only 1.4ns. Therefore, the total response time constant of an extremely fast laser blocking device combined with an extremely fast detector should be in the scale of ~0.1ns. A less concentrated gas will require even better devices or higher loaded Q-factor. Thus, CRDS

based on WGM is extremely challenging. If the micro-fabrication technology can push the loaded Q up to 10^{10} (τ_0 ~μs), this technique may be better used for practical sensor development.

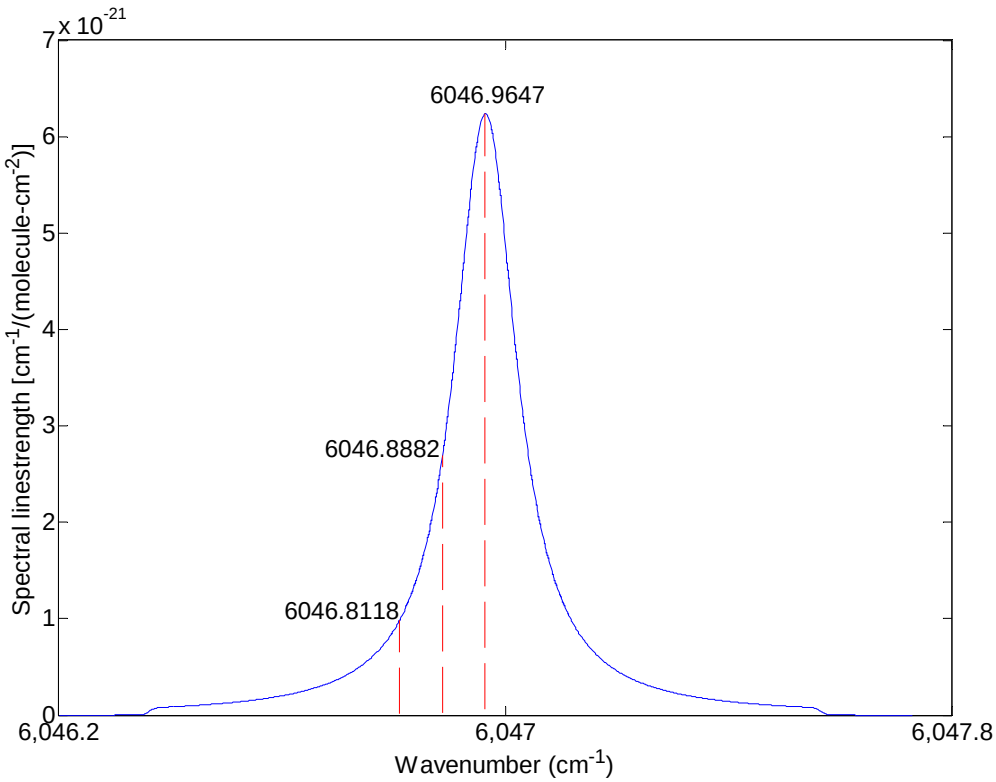

Figure 8.1 Simulated absorption spectral linestrength profile of CH_4 at center wavelength of 1653.7222nm (6046.9657cm^{-1}).

8.4 An estimate of absorption spectroscopy based on *Q*-spoiling of WGM

Due to the high instrumentation requirement of CRDS, *Q*-spoiling technique may be considered as another cavity-enhanced absorption spectroscopy. The loaded *Q*-factor can be easily obtained by the linewidth measurement described in chapter 2. The linewidth of a WGM increases and thus *Q*-factor drops when absorbing species medium is introduced. Using the case in section 8.3 as an example, the initial *Q*-factor is 10^8 and related linewidth

is 1.814MHz. As the ring-down time constants drops to 87.51ns, 87.12ns and 86.33ns, the corresponding Q-factor becomes 9.975×10^7, 9.930×10^7 and 9.840×10^7, respectively, according to equation (2.56). The related linewidths are 1.819MHz, 1.827MHz and 1.844MHz, respectively, obtained from equation (2.42). The maximum linewidth increment is 0.03MHz. More generally, plugging equation (2.42) in equation (2.56) gives

$$\tau = \frac{1}{2\pi\Delta f} \tag{8.18}$$

Using equation (8.17), we have

$$\Delta f - \Delta f_0 = \frac{c f_{eva} k_v(v)}{2\pi} \tag{8.19}$$

where Δf and Δf_0 are the linewidths of the WGM with and without the presence of the absorbing species, respectively. This indicates that the linewidth increment due to Q spoiling does not depend on the original Q-factor. Only the absorption coefficient, $k_v(v)$, determines the amount of linewidth increment. As indicated by equation (2.55), the laser linewidth must be much smaller than the minimum of Δf, Δf_0 and $(\Delta f - \Delta f_0)$ to remove the convolution effect for accurate measurement. Therefore, the laser linewidth determines the minimal detectivity. As for the case studied, the laser linewidth should at most be in the scale of 0.001MHz for the detection of 10000ppm of methane. Weaker absorber would require even smaller laser linewidth. Thus a laser with extremely narrow linewidth is required for this technique.

8.5 Cavity-enhanced absorption spectroscopy based on WGM dip-depth measurement

The depth of a resonant dip, i.e., the coupling coefficient *M* is given by equation (6.1). Define $x = Q_{in} / Q_{coup}$, we have

$$M = \frac{4x}{(1+x)^2} \tag{8.20}$$

As discussed in chapter 3, if *x* equals unity, critical coupling is obtained and the dip depth attains its maximum value of 100%; the micro resonator is said to be under-coupled if the value *x* is less than unity and over-coupled if the value of *x* is greater than unity. Let *f* denote the evanescent energy fraction of the WGM. The effective loss coefficient can be written as $\alpha = \alpha_i + f\alpha_a$, where α_i is the intrinsic loss coefficient and α_a is the absorption coefficient of the absorbing species. As studied by Rosenberger *et al.* [47], the absorption by the absorbing species causes a change in dip depth that, when small (weak analyte absorption), is proportional to the change in absorbing species absorption coefficient. In analogy with Beer's Law, a theoretical effective absorption path length L_{eff}^t can be obtained as

$$L_{eff}^t = \left(\frac{1-x}{1+x}\right)\frac{f}{\alpha_i} \tag{8.21}$$

which holds in the low-absorption limit, i.e. $\alpha_a L_{eff}^t << 1$. Using the same analogy, the experimental effective absorption path length L_{eff}^e can be obtained as

$$L_{eff}^e = \frac{1}{\alpha_a}\ln\frac{M}{M+\Delta M} \tag{8.22}$$

which can be found by measuring the dip depth in the absence of the absorbing species (M) and in the presence of the absorbing species ($M + \Delta M$). By tuning a WGM across the absorption profile of 1% methane at 1653.7222nm, they obtained a dip depth change (50× amplified) as shown in Figure 8.2. The original $|\Delta M / M|$ is actually less than 1%. The loaded Q-factor is 7×10^6. The theoretical and experimental effective path lengths are 15mm and 17mm, respectively.

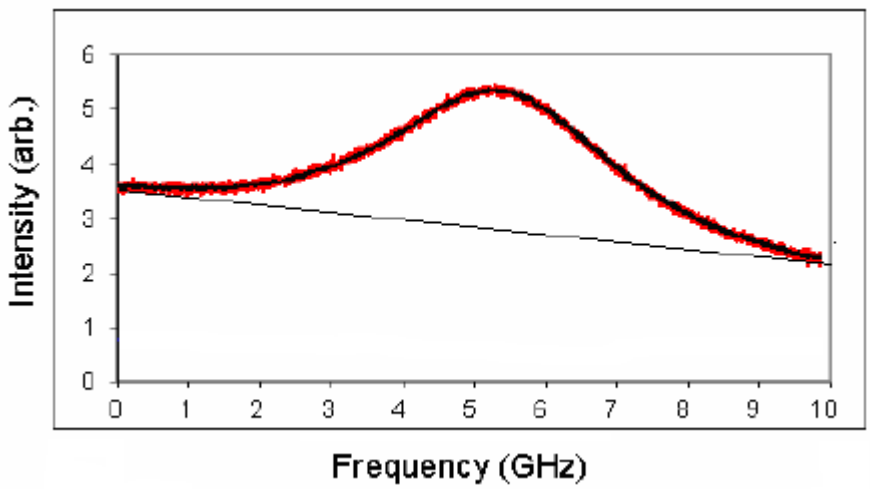

Figure 8.2 The measured absorption profile at 1653.7222nm using depth change for 1% methane obtained by tuning the WGM. The dip depth trace is 50× amplified. Straight line is added to make the variation clear [47].

This is a good demonstration of absorption spectroscopy based on WGM dip depth measurement. However, it is based on a stripped SMF28 fiber rod (125μm in diameter) which inherently has lower Q-factor than a fused microsphere. They stretch the fiber rod using piezo-electric for tuning of the WGM. The effective path length just achieves the order of centimeter.

8.6 Experimental setup for fiber taper-microsphere based WGM absorption spectroscopy

In order to study the fiber taper-microsphere based WGM absorption spectroscopy, an experimental setup is designed and built as schematically shown in Figure 8.3. The WGM coupling system is put in the vacuum chamber as introduced in chapter 6. A gas test cell (63.5cm long) is used for direct absorption spectroscopy test which serves as a spectrum reference. The DFB 1653nm laser is tuned and coupled to a fiber splitter (50/50). One path of the laser is collimated using a fiber collimator (50-1550-FC, Thorlabs) to free space beam and aligned through the gas test cell. The photo of the gas test cell alignments in the setup is shown in Figure 8.4. The other path is used for the WGM coupling. Both the direction absorption and WGM spectra are detected simultaneously with two photodiode detectors. As the chamber and gas test cell are connected with 1/4 inch Teflon tubings, they can be vacuumed in the same time by a vacuum pump. After pumping to vacuum, the chamber and gas test cell can be filled with targeted gas in the same time. The gas concentration can be diluted to a certain value by controlling the valve of vent to air for both the test cell and chamber. The pressure change during vacuum pumping, gas filling and vent are measured by the pressure transducer connected on the chamber.

We use temperature change for tuning of the WGM resonance wavelength. As shown in Figure 8.5, microsphere's supporting fiber stem is held by a copper fiber holder. Silicone paste is applied on the fiber stem and fiber holder to create good heat conduction between them. The microsphere extended out approximately 1cm from the fiber holder. A small 1inch×1inch flexible resistance heater (28V, 5W, KHLV101, Omega) is wrapped and attached on the fiber holder with its own pressure sensitive adhesive. The heater is power

supplied by two wires electrical feedthrough which is produced by the same method as introduced in chapter 6. The heater's power can be controlled by varying the voltage on the DC power supply outside the chamber so that appropriate amount of energy can be transferred to the microsphere for temperature tuning of resonance wavelength.

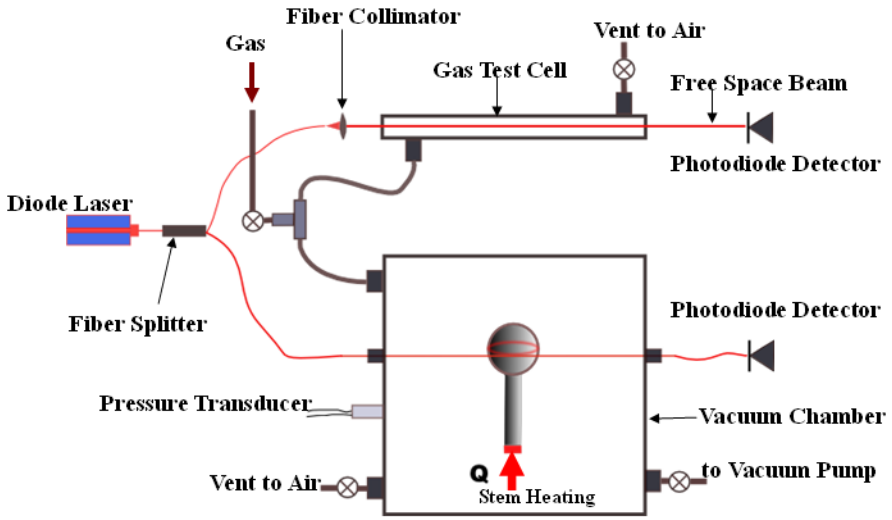

Figure 8.3 Schematic of the experimental setup for fiber taper-microsphere based WGM spectroscopy.

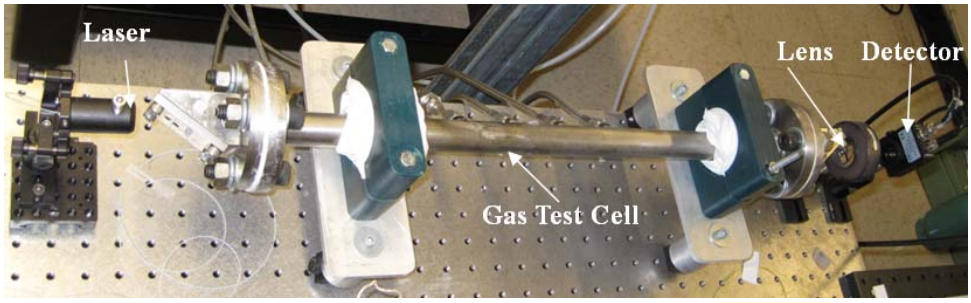

Figure 8.4 Photo of the gas test cell and related optical alignments.

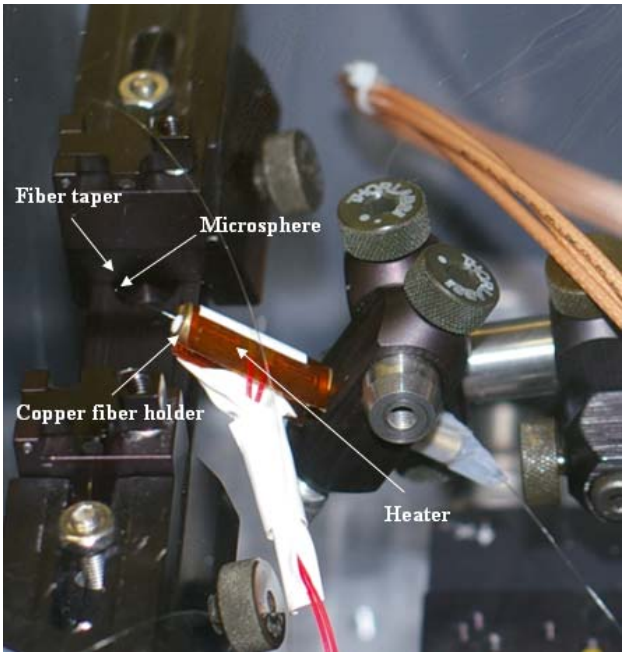

Figure 8.5 Photo of WGM coupling in the vacuum chamber. A 1inch×1inch small flexible heater (10W) is wrapped and attached on the copper fiber holder for temperature tuning of the WGM resonance wavelength.

8.7 Initial experimental results and discussion

To first observe the absorption profile from the dip depth variation, both gas test cell and vacuum chamber are pumped to vacuum and then 100%CH_4 with a pressure of 0.21atm at 293K is filled in the system. The laser is tuned in a range of 183pm around 1653.7222nm (0.667cm^{-1} around 6046.9647cm^{-1}). Figure 8.6 (a) is a simulation of the spectral linestrength in the laser tuning range. To validate the simulation result, the spectral linestrength is converted to transmission absorption spectrum using equations (8.1) and (8.2) for a path length of 63.5cm (length of gas test cell) and compared with experimental test result of the transmission spectrum detected at the end of the gas test cell. The simulation and experiment match with each other very well. This also validates using

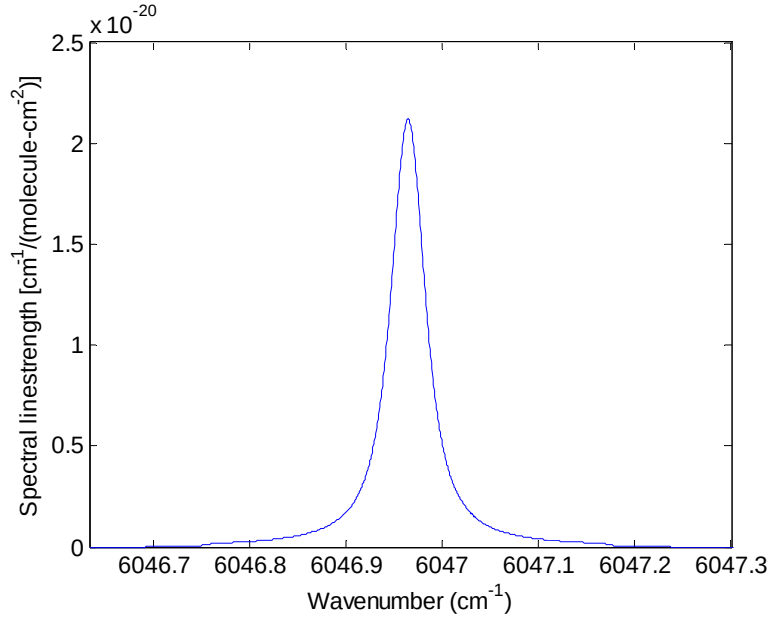

(a)

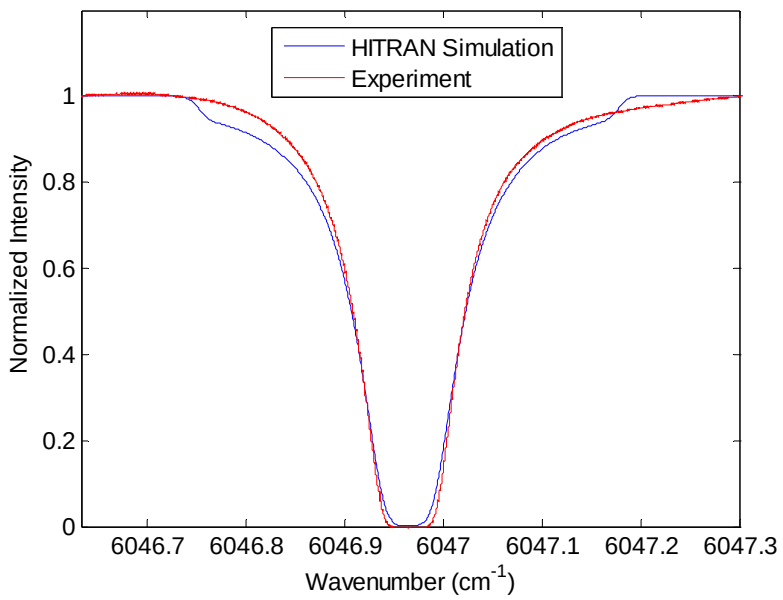

(b)

Figure 8.6 (a) Simulation of CH_4 spectral linestrength profile at 1653.7222nm for 100%CH_4 with a pressure of 0.21atm at 293K (b) Simulation and experimental results of direct transmission absorption spectrum from the 63.5cm gas test cell.

absorption spectroscopy theory and HITRAN database to estimate WGM absorption spectroscopy (CRDS and *Q*-spoiling).

The sphere diameter used in the test is kept relatively small (210μm in diameter) for relatively larger evanescent field fraction. The coupling is repeatedly made for many times until a WGM is located at left part of the spectrum in the small laser tuning range (183pm) indicated in Figure 8.6. A loaded *Q*-factor approximately 2×10^7 is achieved which is almost the highest that can be observed for this microsphere size using our current fabrication and measurement devices. The sphere is slowly heated for 120s and then it cools off for 150s, which produces a total shift about 41pm for each process. This amount of shift indicates a temperature change of approximately 3.6K of the microsphere. The coupling coefficient variation during the heating and cooling processes is shown in Figure 8.7. Error bars illustrate uncertainties of coupling coefficient in the recording time 0.1s at different spectral locations, which clearly show that heating generates more uncertainties. Although the WGM tuning range clearly covers approximately half of the absorption spectrum, unfortunately the variation does not correlate with the absorption profile at all and it appears random.

To identify the cause, our test is compared with Rosenberger's and a scaling method is used to estimate what we should observe. According to equation (8.21), we have

$$L_{eff}^{t} = \left(\frac{1-x}{1+x}\right)\frac{f}{\alpha_i} \propto \left(\frac{1-x}{1+x}\right) fQ_{in} = (1-x)fQ \tag{8.23}$$

From Figure 8.7, it is known that $M \approx 0.6$ which results in $x \approx 0.23$. The evanescent energy fraction f of a fundamental mode of this size of microsphere is very small as shown in Figure 8.8. It is approximately 0.4% at a resonance wavelength around 1653.7222nm. Thus, the scaling is performed as:

$$\frac{L_{eff}^{t}}{L_{eff\_R}^{t}} = \frac{(1-x)fQ}{(1-x_R)f_R Q_R} = \frac{1-0.23}{1-0.28}\frac{0.4\%}{1.6\%}\frac{2\times10^7}{7\times10^6} = 0.76 \tag{8.24}$$

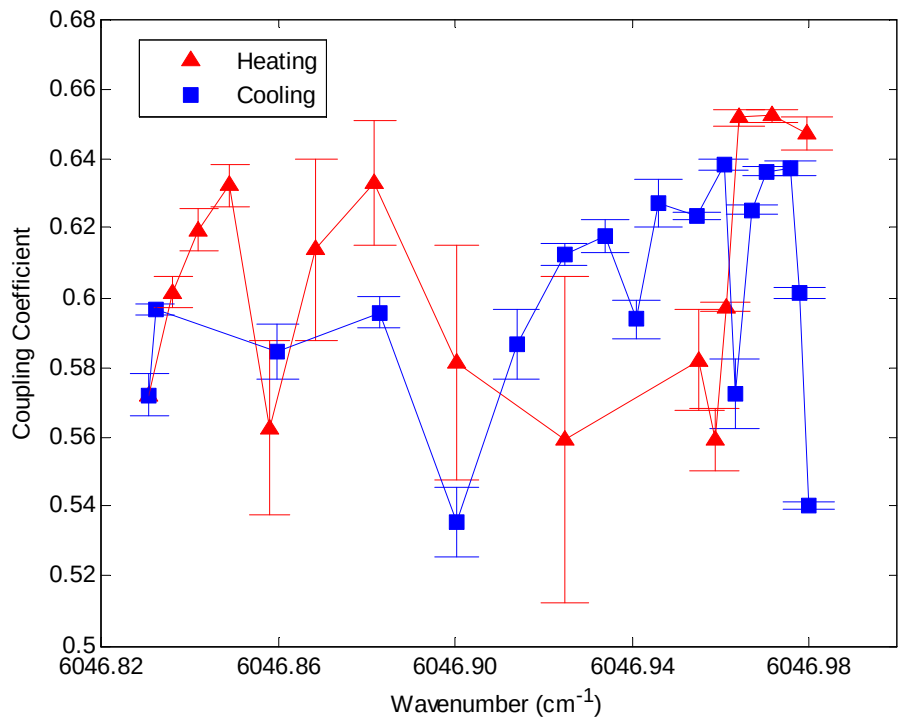

Figure 8.7 Variation of coupling coefficient during temperature tuning of the WGM. The heating process takes 120s and cooling process takes 150s. The total shift of WGM is approximately 41pm for each process.

where the subscript R indicates the values from Rosenberger's study introduced in section 8.5. Surprisingly, although the Q-value in this test is much higher, the effective path length is shorter due to the fact that the evanescent fraction is much smaller. And from equation (8.22), the scaling for dip depth variation is

$$\frac{\Delta M}{M} \propto \alpha_a L_{eff} \tag{8.25}$$

Thus

$$\frac{\Delta M / M}{(\Delta M / M)_R} = 0.76 \frac{\alpha_a}{\alpha_{a\_R}} = 0.76 \frac{0.1099}{0.0053} = 15.76 \tag{8.26}$$

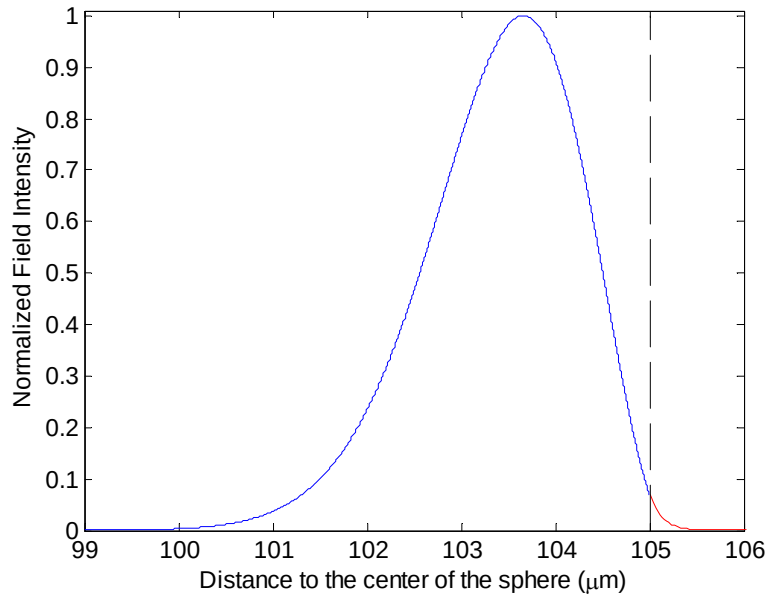

Figure 8.8 A fundamental radial mode around 1653.7222nm for the microsphere with diameter 210μm.

Since $|(\Delta M / M)_R| \le 0.7\%$, we should have $|\Delta M / M| \le 11\%$ in our test. However, the dip depth random variation shown in Figure 8.7 is approximately at a magnitude of 20%. This prevents us from seeing any correlation with the absorption profile. The random variation may be caused by heating and cooling induced instability from the convection boundary conditions. And also the coupling system instability discussed chapter 6 also contributes to the variations.

In conclusion, heating the microsphere for tuning of WGM is not ideal. A more stable tuning method should be used such as applying stress on the microsphere. Obtaining higher *Q*-factor always contradicts with obtaining larger evanescent field energy fraction which is inversely proportional to the size of the microsphere. Better fabrication technique is needed

for fabricating smaller micro resonator which maintains un-compromised Q-factor. Again, as discussed in chapter 6, a properly designed waveguide is needed to replace the fiber taper for more stable coupling for detecting tiny resonance shift and variation of dip depth.

CHAPTER 9

CONCLUSIONS AND FUTURE WORK

9.1 Conclusions

This dissertation has well addressed a few analytical and experimental studies of optical whispering gallery mode resonance in silica micropsheres including temperature sensitivity and measurement resolution of WGM, WGM resonance instability characterization and detection of gas phase molecules using WGM. We first presented a complete theoretical review and study of optical WGM resonance in micro spherical dielectric resonators. The resonance mode distributions including radial, polar and azimuthal are described and solved using both simple geometrical optics and electromagnetic theory. Free spectral range solutions from these two approaches are compared which match with each other well. Concept of WGM Q-factor is introduced. Different loss mechanisms and their contributions to Q-factor calculation are reviewed. A linewidth measurement of WGM for obtaining Q-factor is reviewed and developed for removing the effect of laser linewidth. An experimental system including an ultra fast-electro-optic modulator and a TTL trigger is successfully designed and built for photon life time/cavity ring down measurement, however, our current pulse generator and detection speed limit us for capturing the actual decay signal. For the WGM coupling, different optical couplers are reviewed and compared. A complete theoretical description of optical WGM coupling based on fiber taper-micrpshere system is introduced. The relations of Q-factor to three different coupling regimes are provided. An estimate of

size-matching for efficient coupling between fiber taper and microsphere is given to guide our experimental WGM coupling.

In order to carry out the experimental studies of WGM, after testing different methods of fiber taper and microsphere fabrications, we developed our own fabrication systems and procedures to produce high quality WGM resonance. The fabricated microspheres with size about 50~500μm and fiber taper with submicron waist size are examined using both digital optical microscope and scanning electron microscopy. Setup for micro scale optical WGM coupling is made and different size matched and efficient couplings were obtained for different sizes of microspheres and fiber tapers. Free spectral range of WGM, switching of TE-to-TM mode, and different coupling regimes are experimentally realized and observed. To measure the temperature sensitivity of WGM in a range from approximately 110K to about 310K, we have built temperature well controlled optical test cell and humidity nitrogen-purging system for enclosing WGM coupling system. The measured sensitivity curve matches with the theoretical prediction well. Ultra-high resolution of temperature measurement is discovered and discussed by comparing the resonance linewidth and temperature sensitivity of WGM resonance frequency shift. A potential of 10^{-6} K measurement resolution is predicted for improved WGM coupling system. Potentials of on-chip temperature measurement and cryogenic study applications of the sensor are also addressed.

A specialized vacuum chamber which can achieve 0.03torr vacuum level is designed and fabricated for enclosing the WGM coupling system. A fixture holding the delicate fiber taper is made for transporting it from the fabrication stage into the chamber. Special electrical feedthroughs are designed and made for controlling the coupling in vacuum. For

WGM resonance instability characterizations, in vacuum condition, the WGM spectra and the spectra of fiber ring resonator are simultaneously acquired in parallel laser paths. The massive continuous scanned WGM spectra is corrected and reconstructed using the Fabry-Perot interferences from the fiber ring resonator. Tiny laser wavelength drifting and non-linear tuning effects are observed and eliminated in the signal using this method. WGM resonance wavelength shifts, *Q*-factor and coupling coefficient are then extracted out. A random resonance shift noise within 0.4pm is observed for different levels of laser input powers and with different levels of *Q*-factor, which is analyzed to result from coupling instability of the system. A microsphere coated with SiO_2 nanoparticles using electrostatic self-assembly approach is used for WGM spectral response study of water vapor adsorption-desorption of the coating. The humidity is well controlled in a low level (0~10%) for the tests. The result matches well a theoretical analysis based on Mie theory for coated microsphere. A change of 1ppm water molecule is found to be resolvable from the spectral shift. The Mie theory study also indicates that a lower radial mode excitation in a submicron coating with refractive index higher than the microsphere is most desirable for coated microsphere gas sensing. Finally, we theoretically examined the different gas sensing schemes based on WGM enhanced absorption spectroscopy, including cavity ring down, *Q*-spoiling and dip depth variation. An experiment is carried out to test WGM absorption spectroscopy in comparing with a parallel direct absorption spectroscopy, which provides us insights in directions of improving the absorption based WGM sensor.

9.2 Future work

(I). Faster pulse generator and detector can be used to finally achieve the cavity ring down measurement for recording photon life time of a WGM, which is better for ultra high *Q*-factor measurement and can be applied in cavity ring down spectroscopy.

(II). Electric-arc and CO_2 laser can be explored for fabricating silica microsphere with higher quality factors. Higher *Q*-factor in smaller microsphere is very useful for WGM cavity-enhanced absorption spectroscopy.

(III). A waveguide can be designed and fabricated to do efficient WGM coupling with the microsphere. Ease of coupling light into and out of the waveguide should be considered. The rigidity of the waveguide should make the coupling more stable comparing with the fiber taper.

(IV). An external cavity diode laser could be used to replace the DFB laser to offer broader scanning range and much narrower laser linewidth for better resolving higher *Q* WGM.

(V). A better packaging of the WGM coupling system could be designed to allow measuring much lower cryogenic temperatures.

(VI). Microsphere could be coated with SiN_X to absorb infrared radiations which may give a way of producing ultra sensitive thermal imager. It can be tested in vacuum using the vacuum chamber fabricated in this dissertation.

(VI).The coated microsphere can be explored more to measure other gas in an ultra-sensitive way. For example, cryptophanes can be used as a coating to absorb methane.

REFERENCES

[1] Akahane, Y., Asano, T., Song, B.S. and Noda, S., 2003, "High-*Q* photonic nanocavity in a two-dimensional photonic crystal," *Nature*, vol. 425, pp. 944-947.

[2] Savchenkov, A.A., Matsko, A.B., IIchenko, V.S. and Maleki, L., 2007, "Optical resonators with ten million finesse," Optics Express, vol. 15, pp. 6768-6773.

[3] Rayleigh, J.W.S., 1945, "*The theory of sound*", vol. II, New York: Dover.

[4] Rayleigh, J.W.S., 1914, "Further applications of Bessel's functions of high order to the whispering gallery and applied problems," *Phil. Mag.*, vol.27, pp.100-109, 1914.

[5] Rayleigh, J.W.S., 1910, "The problem of the whispering gallery," *Phil. Mag.*, vol.20, pp. 1001-1004, 1910.

[6] Debye, P., 1909, "Der lichtdruck auf kugeln von beliebigem material," *Ann. Phys.*, vol.30, pp. 57 – 136.

[7] Mie, G., 1908, "Beitrage zur optik truber medien," *Ann. Phys.*, vol. 25, pp. 377 – 445.

[8] Gastine, M., Courtois, L., and Dormann, J.L., 1967, "Electromagnetic resonances in free dielectric spheres," *IEEE Tran. Microwave Theor. Techn.*, vol. MTT-15, pp. 694-700.

[9] Affolter, P. and Eliasson, B., 1973, "Electromagnetic resonances and *Q*-factors of lossy dielectric spheres," *IEEE Tran. Microwave Theor. Techn.*, vol. MTT-21, pp. 573-578.

[10] Balistreri, M. L. M., Klunder, D. J. W., Blom, F. C., Driessen, A. and Hoekstra, H. W. J. M., Korterik, J. P., Kuipers, L., and Hulst, N. F., 1999, "Visualizing the whispering gallery modes in a cylindrical optical microcavity," *Optics Letters*, vol. 24, pp.1829-1831.

[11] Braginsky,V. B., Gorodetsky, M. L., and Ilchenko, V. S., 1989, "Quality-factor and nonlinear properties of optical whispering-gallery modes," *Phys. Lett. A*, vol. 137, pp. 393-396.

[12] Armani, D. K., Kippenberg, T. J., Spillane, S. M., and Vahala, K. J., 2003, "Ultra-high-Q toroid microcavity on a chip," *Nature*, vol. 421, pp. 925-928.

[13] Little, B. E., Foresi, J. S., Steinmeyer, G., Thoen, E. R., Chu, S. T., Haus, H. A., Ippen, E. P., Kimerling, L. C. and Greene, W.,1998, "Ultra-compact Si–SiO_2 microring resonator optical channel dropping filters," *IEEE Photonics Technology Letters*, vol. 10, pp.549-551.

[14] Vernooy, D. W., Furusawa, A., Georgiades, N. Ph., Ilchenko, V. S., and Kimble, H. J., 1998, "Cavity QED with high-Q whispering gallery modes," *Physical Review A*, vol. 57, pp. R2292-R2296.

[15] Sandoghdar, V., Treussart, F., Hare, J., Lefevre-Seguin, V., Raimond, J.-M., and Haroche, S., 1996, "Very low threshold whispering-gallery-mode microsphere laser," *Physical Review A*, vol. 54, pp.R1777-R1780.

[16] Cai, M., Painter, O., Vahala, K. J. and Sercel, P. C., 2000, "Fiber-coupled microsphere laser," *Optics Letters*, vol. 25, pp.1430-1432.

[17] Rabiei, P., Steier, W. H., Zhang, C., and Dalton, L. R., 2002, "Polymer micro-ring filters and modulators," *Journal of Lightwave Technology*, Vol. 20, pp. 1968-1975.

[18] Arnold, S., Khoshsima, M., Teraoka, I., Holler, S. and Vollmer, F., 2003, "Shift of whispering-gallery modes in microspheres by protein adsorption," *Optics Letters*, Vol. 28, pp. 272-274.

[19] Quan. H. and Guo, Z., 2007, "Simulation of single transparent molecule interaction with an optical microcavity," *Nanotechnology*, vol. 18, 375702 (5pp).

[20] Garrett, C. G. B., Kaiser, W., and Bond, W. L., 1961, "Stimulated emission into optical whispering gallery modes of spheres," *Phys. Rev.*, vol. 124, pp. 1807-1809.

[21] Walsh, P. and Kemeny, G., 1963, "Laser Operation without Spikes in a Ruby Ring," *J. Appl. Phys.*, vol. 34, pp. 956-957.

[22] Knight, J. C., Driver, H. S. T., Hutcheon, R. J. and Robertson, G. N.,1992, "Core resonance capillary fiber whispering gallery mode laser," Opt. Lett., vol. 17, pp. 1280-1282.

[23] Sandoghdar, V., Treussart, F., Hare, J., Lefevre-Seguin, V., Raimond, J. M. and Haroche, S., 1996, "Very low threshold whispering-gallery-mode microsphere laser," *Phys. Rev. A*, vol. 54, pp. R1777-R1780.

[24] Ilchenko, V. S., Savchenkov, A. A., Matsko, A. B. and Maleki, L., 2004, "Nonlinear optics and crystalline whispering gallery mode cavities," *Phys. Rev. Lett.*, vol. 92, 043903.

[25] Savchenkov, A. A., Ilchenko, V. S., Matsko, A. B. and Maleki, L., 2004, "KiloHertz optical resonances in dielectric crystal cavities," *Phys. Rev. A*, vol. 70, 051804.

[26] Little, B. E., Chu, S. T., Haus, H. A., Foresi, J. and Laine, J. P., 1997, "Microring resonator channel dropping filters," *J. Lightwave Technol.*, vol. 15, pp. 998-1005.

[27] Chu, S. T., Little, B. E., Pan, W., Kaneko, T. and Kukubun, Y., 1999, "Second-order filter response from parallel coupled glass microring resonators," *IEEE Phot. Tech. Lett.*, vol. 11, pp.1426-1428.

[28] Blair, S. and Chen, Y., 2001, "Resonant-enhanced evanescent-wave fluorescence biosensing with cylindrical optical cavities," *Applied Optics*, vol. 40, pp. 570-582.

[29] Vollmer, F. and Arnold, S., 2008, "Whispering-gallery-mode biosensing: label-free detection down to single molecules," *Nature Methods*, vol. 5, pp. 591-596.

[30] Teraoka, I., Arnold, S. and Vollmer, F., 2003, "Perturbation approach to resonance shifts of whispering-gallery modes in a dielectric microsphere as a probe of a surrounding medium," *J. Opt. Soc. Am. B*, vol. 20, pp. 1937-1946.

[31] Laine, J. P., Tapalian, C., Little, B. and Haus, H., 2001, "Acceleration sensor based on high-*Q* optical microsphere resonator and pedestal antiresonant reflecting waveguide coupler," *Sensors and Actuators A*, vol. 93, pp. 1-7.

[32] Ioppolo, T., Kozhevnikov, M., Stepaniuk, V., Ötügen, M. and Sheverev, V., 2008, "Micro-optical force sensor concept based on whispering gallery mode resonators," *Applied Optics*, vol. 47, pp. 3009-3014.

[33] Huston, A. L. and Eversole, J. D., 1993, "Strain-sensitive elastic scattering from cylinders," *Optics Letters*, vol. 18, pp. 1104-1106.

[34] Matsko, A. B., Savchenkov, A. A., Ilchenko, V. S. and Maleki, L., 2004, "Optical gyroscope with whispering gallery mode optical cavities," *Optics Communications*, vol. 233, pp. 107-112.

[35] Little, B. E., Laine, J. P., and Haus, H. A., 1999, "Analytic theory of coupling from tapered fibers and half-blocks into microsphere resonators," *Journal of Lightwave Technology*, vol. 17, pp. 704-715.

[36] Gorodetsky, M. L., Savchenkov, A. A. and Ilchenko, V. S., 1996, "Ultimate Q of optical microsphere resonators," *Optics Letters*, vol. 21, pp. 453-455.

[37] Gorodetskya, M.L. and Ilchenkoa, V.S., 1994, "High-*Q* optical whispering-gallery microresonators: precession approach for spherical mode analysis and emission patterns with prism couplers," *Optics Communications*, vol. 113, pp. 133-143.

[38] Dubreuil, N., Knight, J. C., Leventhal, D. K., Sandoghdar, V., Hare, J. and Lef ever, V., 1995, "Eroded monomode optical fiber for whispering-gallery mode excitation in fused-silica microspheres," *Optics Letters*, vol. 20, pp. 813-815.

[39] Ilchenko, V. S., Yao, X. S. and Maleki, L., 1999, "Pigtailing the high-Q microsphere cavity: a simple fiber coupler for optical whispering-gallery modes," *Optics Letters*, vol. 24, pp.723-725.

[40] Knight, J. C., Cheung, G., Jacques, F. and Birks, T. A., 1997, "Phase-matched excitation of whispering-gallery-mode resonances by a fiber taper," *Optics Letters*, vol. 22, pp. 1129-1131.

[41] Yang, L., 2005, "Fabrication and characterization of microlasers by the sol-gel method", *PhD dissertation*, California Institute of Technology.

[42] Schiller, S., 1993, "Asymptotic expansion of morphological resonance frequencies in Mie scattering," *Applied Optics*, vol. 32, pp. 2181-2185.

[43] Quan, H. and Guo, Z., 2005, "Simulation of whisperinggallery- mode resonance shifts for optical miniature biosensors," *J. Quant. Spectrosc. Radiat. Transfer*, vol. 93, pp. 231–243.

[44] Nguyen, N. Q. and Gupta, N., 2009, "Analysis of an encapsulated whispering gallery mode micro-optical sensor," *Appl. Phys. B*, vol. 96, pp.793-801.

[45] White, I. M., Oveys, H. and Fan, X. D., 2006, "Liquid-core optical ring-resonator sensors," *Opt. Lett.*, vol.31, pp.1319–1321.

[46] Armani, A. and Vahala, K., 2006, "Heavy water detection using ultra-high-Q microcavities," *Opt. Lett.*, vol. 31, pp.1896–1898.

[47] Farca1, G., Shopova, S. I. and Rosenberger, A. T., 2007, "Cavity-enhanced laser absorption spectroscopy using microresonator whispering-gallery modes," *Optics Express*, vol. 15, pp. 17443-17448.

[48] Guo, Z., Quan, H. and Pau, S., 2006, "Near-field gap effects on small microcavity whispering-gallery mode resonators," *J. Phys. D: Appl. Phys.*, vol. 39, pp. 5133-5136.

[49] Cai, Z., Chardon, A., Xu, H., Feron, P. and Michel Stephan, G., 2002, "Laser characteristics at 1535 nm and thermal effects of an Er:Yb phosphate glass microchip pumped by Ti:sapphire laser," *Optics Communications*, vol. 203, pp. 301-313.

[50] Carmon, T., Yang, L. and Vahala, K. J., 2004, "Dynamical thermal behavior and thermal selfstability of microcavities," *Optics Express*, vol. 12, pp. 4742-4750.

[51] Han, M. and Wang, A., 2007, "Temperature compensation of optical microresonators using a surface layer with negative thermo-optic coefficient," *Optics Letters*, vol. 32, pp. 1800-1802.

[52] Incropera, F. and Dewitt, D., 1996, "*Introduction to Heat Transfer*", New York: Wiley.

[53] http://accuratus.com/fused.html

[54] Leviton, D. and Frey, B., 2006, "Temperature-dependent absolute refractive index measurements of synthetic fused silica," *Proc. SPIE*, vol. 6273, 62732K

[55] Lefevre, P. and Petterson, T., 1995, "The large hadron collider-conceptual design," *CERN Report*, No. CERN/AC/95–05 (LHC).

[56] Lee, Y. and Lee, B., 2002, "High resolution cryogenic optical fiber sensor system using erbium-doped fiber," *Sensors Actuators A*, vol. 96, pp. 25–27.

[57] Bertrand, S., Jalocha, A., Tribillon, G., Bouazaoui, M. and Rouhet, J., 1996, "Optical fibre temperature sensor in the cryogenic range," *Opt. Laser Technol.*, vol. 28, pp. 363–366.

[58] Ciotti, M., Nardelli, V., Caponero, M A., Felli, F., Lupi, C. and Ippoliti, L., 2007, "An optical system for cryogenic temperature measurements," *Smart Mater. Struct.*, vol. 16, pp. 1708–1711.

[59] Humphrey, M., Dale, E., Rosenberger, A. and Bandy, D., 2007, "Calculation of optimal fiber radius and whispering-gallery mode spectra for a fiber-coupled microsphere," *Opt. Commun.*, vol. 271, pp. 124–131.

[60] Barron, T. and White, G., 1999, "*Heat capacity and thermal expansion at low temperatures*", New York: Plenum.

[61] Jha, C. M., Bahl, G., Melamud, R., Chandorkar, S. A., Hopcroft, M. A., Kim, B., Agarwal, M., Salvia, J., Mehta, H. and Kenny, T. W., 2007, "High resolution microresonator-based digital temperature sensor," *Applied Physics Letters*., vol. 91, 074101.

[62] NASA's Jet Propulsion Laboratory, 2008, "Temperature Sensors Based on WGM Optical Resonators," *Technical Briefs: Physical Sciences*.

[63] Ma, Q., Rossmann, T. and Guo, Z., 2008, "Temperature sensitivity of silica micro-resonators," *J. Phys. D: Appl. Phys.*, vol. 41, 245111.

[64] Shih, Y. H.and Hwu, J. G., 2001, "An on-chip temperature sensor by utilizing a MOS tunneling diode," *IEEE Electron Device Lett.*, vol. 22, pp. 299-301.

[65] Guo, Z., Quan, H. and Pau, S., 2006, "Numerical characterization of whispering-gallery mode optical microcavities," *Applied Optics*, vol. 45, pp. 611-618.

[66] Samy, R., Glawdel, T., and Ren, C. L., 2008, "Method for microfluidic whole-chip temperature measurement using thin-film poly(dimethylsiloxane)/rhodamine B," *Anal Chem*, vol. 80, pp. 369-375.

[67] Ross, D. and Locascio, L. E., 2003, "Effect of caged fluorescent dye on the electroosmotic mobility in microchannels," *Anal. Chem.*, vol. 75, pp. 1218–1220.

[68] Erickson, D., Liu, X., Venditti, R., Li, D. and Krull, U. J., 2005, "Electrokinetically based approach for single-nucleotide polymorphism discrimination using a microfluidic device," *Anal Chem.*, vol. 77, pp. 4000-4007.

[69] Stokes, L. F., Chodorow, M. and Shaw, H. J., 1982, "All-single-mode fiber resonator," Optics Letters, vol. 7, pp.288-290.

[70] Abraham, E. and Cornell, E., 1998, "Teflon feedthrough for coupling optical fibers into ultrahigh vacuum systems," *Appl. Opt.* vol. 37, pp. 1762-1763.

[71] Vollmer, F., Arnold, S., Braun, D., Teraoka, I. and Libchaber, A., 2003, "Multiplexed DNA quantification by spectroscopic shift of two microsphere cavities," *Biophys. J.*, vol. 85, pp. 1974-1979.

[72] Krioukov, E., Klunder, D., Driessen, A., Greve, J. and Otto, C., 2002, "Sensor based on an integrated optical microcavity," *Opt. Lett.*, vol. 27, pp. 512-514.

[73] Sumetsky, M., Windeler, R., Dulashko, Y. and Fan, X., 2007, "Optical liquid ring resonator sensor," *Opt. Express*, vol. 15, pp. 14376-14381.

[74] Armani, A., Kulkarni, R., Fraser, S., Flagan, R. and Vahala, K., 2007, "Label-free, single-molecule detection with optical microcavities," *Science*, vol. 317, pp. 783-787.

[75] Corres, J., Matias, I., Hernaez, M., Bravo, J. and Arregui, F., 2008, "Optical fiber humidity sensors using nanostructured coatings of SiO2 nanoparticles," *IEEE Sens. J.*, vol. 8, pp. 281-285.

[76] Chen, Z. and Lu, C., 2005, "Humidity sensors: a review of materials and mechanisms," *Sens. Lett.*, vol. 3, pp. 274-295.

[77] Viegas, D., Goicoechea, J., Corres, J., Santos, J., Ferreira, L., Araujo, F. and Matias, I., 2009, "A fibre optic humidity sensor based on a long-period fibre grating coated with a thin film of SiO_2 nanospheres," *Meas. Sci. Technol.*, vol. 20, 034002.

[78] Teraoka, I. and Arnold, S., 2006, "Enhancing the sensitivity of a whispering-gallery mode microsphere sensor by a high-refractive-index surface layer," *J. Opt. Soc. Am. B*, vol. 23, pp. 1434-1441

[79] Villar, I., Matías, I., Arregui, F. and Claus, R., 2005, "Fiber-optic hydrogen peroxide nanosensor," *IEEE Sens. J.*, vol. 5, pp. 365-371.

[80] Wang, C., Wu, C., Chen, I. and Huang, Y., 2005, "Humidity sensors based on silica nanoparticle aerogel thin films," *Sens. Actu. B*, vol. 107, pp. 402-410.

[81] Martin, J., Paldus, B. A., Zalicki, P., Wahl, E. H., Owano, T. G., Harris, J. S., Kruger, C. H. and Zare, R. N., 1996, "Cavity ringdown spectroscopy with Fourier transform limited light pulses," *Chem. Phys. Lett.*, vol. 258, pp. 63–70.

[82] Sappey, A. D., Hill, E. S., Settersten, T. and Linne, M. A., 1998, "Fixed-frequency cavity ringdown diagnostic for atmospheric particulate matter," *Opt. Lett.*, vol. 23, pp. 954-956.

[83] Gherman, T. and Romanini, D., 2002, "Mode–locked cavity–enhanced absorption spectroscopy," Optics Express., vol. 10, pp. 1033-1042.

[84] Scherer, J. J., Paul, J. B., O'Keefe, A. and Saykally, R. J., 1997, "Cavity ringdown laser absorption spectroscopy: history, development, and application to pulsed molecular beams," *Chem. Rev.* vol. 97, pp. 25–51.

[85] Nakagawa, K., Katsuda, T., Shelkovnikov, A. S., Labachelerie, M. and M. Ohtsu, 1994, "Highly sensitive detection of molecular absorption using a high finesse optical cavity," *Opt. Commun.*, vol. 107, pp. 369-372.

[86] Romanini, D., Kachanov, A.A., Sadeghi, N., Stoeckel, E., 1997, "CW cavity ring down spectroscopy," *Chemical Physics Letters*, vol. 264, pp. 316-322.

[87] Totschnig, G., Baer, D.S., Wang, J., Winter, F., Hofbauer, H. and Hanson, R.K., 2000, "Multiplexed continuous-wave diode-laser cavity ringdown measurements of multiple species," *Appl. Optics*, vol. 39, pp. 2009-2016.

[88] Rothman, L. S., Rinsland, C. P., Goldman, A., Massie, S. T., Edwards, D. P., Flaud, J.-M., Perrin, A., Camy-Peyret, C., Dana, V., Mandin, J.-Y., Schroeder, J., McCann, A., Gamache, R. R., Wattson, R. B., Yoshino, K., Chance, K. V., Jucks, K. W., Brown, L. R., Nemtchinov, V. and Varanasi, P., 1998, "The HITRAN molecular spectroscopic database and HAWKS (HITRAN Atmospheric Workstation): 1996 Edition," *J. Quant. Spectrosc. Radiat. Transfer*, vol. 60, pp. 665-710.

[89] Mihalcea, R. M., 1999, "CO and CO2 measurements in combustion environments using external cavity diode lasers," *Standford University, PhD thesis*.

[90] Busch, K. W. and Busch, M. A., 1999, "*Cavity-ring down spectroscopy: an ultratrace-absorption measurement technique*" Washington, DC: American Chemical Society.

[91] Quan, H., 2006, “Characterization of Optical Whispering Gallery Mode Resonance and Applications,” *PhD dissertation*, Rutgers University.

CURRICULUM VITAE OF THE AUTHOR

EDUCATION

PhD Mechanical & Aerospace Engineering, Rutgers University, New Jersey

GPA 4.0 October 2010

MS Engineering Thermophysics, Tsinghua University, Beijing, China

GPA 3.8 July 2005

BS Thermal Engineering, Tsinghua University, Beijing, China

GPA 3.5 July 2003

ACADEMIC HONORS AND AWARDS

2009 SPIE Optics+Photonics Travel Grant	8/2009
MAE Fellowship, Rutgers University	2005~06
Guanghua First Prize Scholarship, Tsinghua University (Top 5%)	2004~05
Weilun Fundation Scholarship, Tsinghua University (Top 2%)	2003~04
Excellent Student Scholarship, Tsinghua University (Top 10%)	2001~02

PROFESSIONAL AFFILIATIONS

New York Society of Applied Spectroscopy (NYSAS)

International Society of Optical Engineering (SPIE)

American Society of Mechanical Engineering (ASME)

RESEARCH EXPERIENCE

Research Assistant, Rutgers University, New Jersey, USA 9/2005~6/2010

Research Assistant, Tsinghua University, Beijing, China 9/2003-6/2005

PUBLICATIONS

[1] **Ma, Q.**, Rossmann, T., Guo, Z., "Whispering-Gallery Mode Silica Microsensors for Cryogenic to Room Temperature Measurement" Measurement Science and Technology 21 025310 (7pp) 2010

[2] **Ma, Q.**, Huang, L., Guo, Z. and Rossmann, T., "Spectral Shift Response of Optical Whispering Gallery Modes due to Water Vapor Adsorption and Desorption," Accepted by Measurement Science and Technology, 2010

[3] **Ma, Q.**, Rossmann, T., Guo, Z., "Temperature sensitivity of silica micro-resonators" Journal of Physics D: Applied Physics 41 245111 (6pp) 2008

[4] **Ma, Q.**, Rossmann, T., Guo, Z., "Micro-Temperature Sensor based on Optical Whispering Gallery Mode of Fiber Taper-Microsphere Coupling System" SPIE Optics and Photonics, San Diego, CA, Paper No. 7420-25, August 2~6, 2009

[5] **Ma, Q.**, Rossmann, T., Guo, Z., "Fabrication, Characterization and Microsensing of Whispering-Gallery Mode Micro-Coupling System" ASME International Mechanical Engineering Congress & Exposition, Boston, MA, Paper No.IMECE-66946, October 31~November 6, 2008

[6] **Ma, Q.**, Li, S., Guo, Z., and Rossmann, T,, "Trace Gas Detection Utilizing Optical Spectroscopy of Microresonant Cavities" 45th AIAA Aerospace Sciences Meeting and Exhibit, Paper No. 2007-0874, January 8~11, 2007, Reno, Nevada

[7] **Ma, Q.**, Rossmann, T., Knight, D. and Jaluria, Y., "Utilization of Laser-Based Measurements and Numerical Simulation for Analysis of Thermal-Fluid Systems Using

Dynamic Data Driven Application Systems" 45th AIAA Aerospace Sciences Meeting and Exhibit, Paper No.2007-0875, January 8~11, 2007, Reno, Nevada

[8] **Ma, Q.**, Luo, Y., Rossmann, T., Knight, D. and Jaluria, Y., "Diode Laser Measurements for DDDAS: Flowfield Reconstruction Using Dynamic Experimental and Numerical Data" 25th AIAA Aerodynamic Measurement Technology and Ground Testing Conference, Paper No.2006-2974, June 5~8, 2006, San Francisco, California

[9] Knight, D., **Ma, Q.**, Rossman, T. and Jaluria, Y., "Determining Unknown Boundary Conditions in Fluid-Thermal Systems Using the Dynamic Data Driven Application Systems Methodology" Third International Symposium on Integrating CFD and Experiments in Aerodynamics, US Air Force Academy, Colorado Springs, CO, June 21~22, 2007.

[10] Knight, D., **Ma, Q.**, Rossman, T. and Jaluria, Y., "Evaluation of Fluid-Thermal Systems by Dynamic Data Driven Application Systems – Part II" Lecture Notes in Computer Science, Springer Berlin/Heidelberg, ISSN 0302-9743 (Book Chapter).

[11] Knight, D., **Ma, Q.**, Rossman, T. and Jaluria, Y., "Assessment of Fluid-Thermal Systems by Dynamic Data Driven Application Systems" International Conference on Modeling and Optimization of Structures, Processes and Systems, University of Kwazulu-Natal, South Africa, January 22~24, 2007.

[12] **Ma, Q.** and Peng, XF., "Clustering Analysis of Nucleation during Solidification" Chinese Journal of Engineering Thermophysics, vol.25 2004. (in Chinese)